MPHIL

Aeroelastic Topology Optimisation of Aircraft High Aspect Ratio Wings

Seow, Vincent

Award date:
2017

Awarding institution:
University of Bath

Aeroelastic Topology Optimisation of Aircraft High Aspect Ratio Wings

submitted by

Youk Eng Vincent Seow

for the degree of Master of Philosophy

of the

University of Bath

Department of Mechanical Engineering

June 2016

Abstract

Aeroelastic topology optimisation is used to design and optimise the internal configuration of an aircraft high aspect ratio wing box. The approach combines an aeroelastic analysis solver, aeroelastic sensitivity analysis solver, and level set based topology optimisation algorithm. The aeroelastic solver is used to couple the aerodynamic model with structural model and perform a flutter analysis. The aeroelastic sensitivity analysis solver is used to calculate the sensitivities of wing mass, compliance and flutter with respect to structural design variables. Although aeroelastic topology optimisation allows greatest freedom to design the wing box layout, there are a few challenges existing in this subject.

Two of the main issues with the aeroelastic topology optimisation are mode switching and local modes. Both mode switching and local modes problems cause the discontinuity throughout the optimisation hence makes the solution difficult to converge. These issues are addressed in this thesis by implementing the improved eigenvector orthogonality correlation method, imposing the continuous flutter constraint and implementing the effective modal mass method in the topology optimisation problem. The optimisation of various high aspect ratio wings demonstrates the usefulness and importance of resolving these two issues.

Acknowledgements

I would like to express my greatest gratitude to my supervisors Dr. Alicia Kim, Professor Chris Bowen and Professor Richard Butler for their advice and continuous support. I am also very thankful for having the opportunity to work with Dr. Peter Dunning, who kindly shared with me his level set codes and helped me to understand topology optimisation.

During my years at University of Bath I benefited from the friendship of my fellow colleagues and friends. I am very grateful to them for their helpful discussions and suggestions, particularly Dr. Chris Brampton, Dr. Dave Betts, Dr. Sean Jenkins, Peter Harris and Jia Ming.

I also wish to thank my parents for supporting my research in the later years and working really hard to send me abroad to study when I was 19 years old. A special thanks to Glyn and Ruth Greenaway for being my guardian and providing me with guidance and support for the past few years in the UK.

This research was funded by Great Western Research (GWR) and Airbus UK and their support is greatly appreciated.

I would not have finished my final thesis without the love and support from my wife, Michelle. The joy and experience that we have together are invaluable and I am really pleased to have her as my partner and closest friend.

Contents

List of Figures

List of Tables

Nomenclature

Abbreviations

AIC	Aerodynamic Influence Coefficient
CFD	Computational Fluid Dynamics
CSM	Computation Structural Mechanics
DKT	Discrete Kirchoff Triangular
DLM	Doublet Lattice Method
FEA	Finite Element Analysis
FEM	Finite Element Method
FPS	Finite Plate Spline
MAC	Modal Assurance Criterion
SIMP	Simple Isotropic Material with Penalisation
SLP	Sequential Linear Programming
2D	Two dimensional
3D	Three dimensional

Latin Symbols

A_c	Constant factor over the entire structural boundary

$\boldsymbol{A}$	Unsteady aerodynamic matrix
$\boldsymbol{A}_i$	Imaginary part of the unsteady aerodynamic matrix
$\boldsymbol{A}_r$	Real part of the unsteady aerodynamic matrix
$\widetilde{\boldsymbol{A_i}}$	Reduced imaginary part of the unsteady aerodynamic matrix
$\widetilde{\boldsymbol{A_r}}$	Reduced real part of the unsteady aerodynamic matrix
$\boldsymbol{B}_e$	Strain-displacement matrix
c	Semi-chord of the wing
$c_{i,j}$	Reduced stiffness matrix in weak formulation
C	Compliance value
C^*	Target compliance value
$\boldsymbol{D}$	Non-dimensional downwash factor matrix
E	Young's modulus
f	General function
$\boldsymbol{f}_a$	Aerodynamic load vector in structural mesh
$\boldsymbol{f}_c$	Structural load vector due to downwash
$\boldsymbol{f}_\alpha$	Structural load vector due to angle of attack
$\boldsymbol{f}_g$	Gravity load vector due to wing weight
$\boldsymbol{f}_t$	Total load vector applied on wing structure
g	Damping ratio
g_r	Acceleration due to gravity
G	Constraint function
$H(\Omega)$	Heaviside function
$\boldsymbol{I}$	Identity matrix

J	Jacobian equation
k	Reduced frequency
$\boldsymbol{K}$	Global stiffness matrix
$\widetilde{\boldsymbol{K}}$	Reduced stiffness matrix
$\boldsymbol{L}$	Left eigenvector
$\boldsymbol{L}(\boldsymbol{u})$	Total aerodynamic lift vector
L_c	Aerodynamic lift due to downwash
L_α	Aerodynamic lift due to angle of attack
$\bar{\mathbf{L}}$	Coefficient vector
$m_{i,j}$	Reduced mass matrix in weak formulation
$\boldsymbol{M}$	Global mass matrix
$\widetilde{\boldsymbol{M}}$	Reduced mass matrix
M_{eff}	Effective modal mass
M_w	Wing box structural mass
M_∞	Mach number
n	Unit vector normal to the structural boundary
N	Load factor
$\boldsymbol{N}_e$	Shape function of each finite elements
p	Complex eigenvalue
q	Dynamic pressure
q^*	Flutter dynamic pressure
q_{lim}	Limit on the flutter dynamic pressure
$\boldsymbol{Q}$	Aerodynamic stiffness matrix

$\boldsymbol{Q_d}$	Dual aerodynamic stiffness matrix
$\boldsymbol{R}$	Right eigenvector
R_z	Ratio of effective modal mass between shell and solid elements
s_f	Shape sensitivity function for f
$\boldsymbol{S}$	Integration matrix
t	Time
$\boldsymbol{T_l}$	Load transformation matrix
$\boldsymbol{T}_u$	Displacement transformation matrix
$\boldsymbol{T}_v$	Downwash matrix due to the wing motion
$\boldsymbol{u}$	Structural displacement vector
$\boldsymbol{u}_e$	Nodal displacement for each finite element
U_d	Design cruise speed
U_s	Speed of sound
U_∞	Freestream velocity
v	Virtual displacement
V_n	Velocity function
Vol	Volume of the wing box
w	Velocity weights in level set method
$\boldsymbol{w}$	Adjoint vector
$\bar{\boldsymbol{w}}$	Normalwash vector
$\boldsymbol{w_c}$	Slope of the aerofoil centreline
$\boldsymbol{w}(\boldsymbol{u})$	Downwash vector dependent on deformed wing shape
W	Total weight of the aircraft

W_b	Weight of the wing box
W_c	Fixed weight of the aircraft
$\boldsymbol{z}$	Column vector of ones

Greek Symbols

α	Angle of attack
$\boldsymbol{\varepsilon}$	Strain vector
$\boldsymbol{\varepsilon_e}$	Elemental strain vector
ρ	Material density
λ	Lagrangian multiplier
$\mathcal{L}$	Lagrangian equation
ρ_{air}	Air density
$\Delta\overline{\boldsymbol{p}}$	Pressure difference vector
Δt	Discrete time step
$\boldsymbol{\eta}$	Eigenvector
$\boldsymbol{\Phi}$	Modal matrix
θ	Direction of the velocity function
ϕ	Level set function defining a structural boundary
$\boldsymbol{\varphi}$	Modal amplitudes vector
Ω	Domain of a structure
Γ	Boundary of a structure
Γ_D	Boundary of where boundary conditions are applied

Ω_d	Design domain
Ψ	Modal participation factor matrix
τ	Influence vector
ω	Harmonic frequency

Chapter 1

Introduction

1.1 Structural Topology Optimisation

Structural topology optimisation has been used in a variety of engineering fields over the past three decades. It is concerned with seeking the optimum distribution of material in a given design domain that minimises a given cost function, while satisfying all prescribed constraints. For example, in the aerospace engineering field, the best structure might be the one with the lowest mass that meets all stress, flutter, fatigue and manufacturing constraints.

In structural topology optimisation, both the layout and sizing of the structure can be determined. This freedom allows the greatest opportunity to find the best possible design. However, this freedom usually translates into a large number of design variables that can make topology optimisation problems difficult to solve. Since computers have become more powerful to analyse complex structures, intensive research (Bendsøe and Sigmund 2004) has been undertaken for a wide

range of applications into developing computational methods for solving structural topology optimisation problems.

1.2 Aeroelastic Optimisation

Today, aircraft wing design has become one of the most challenging engineering fields as the process involves the application of wide variety of different but interrelated disciplines, such as aerodynamics, structures, stabilities and aeroelasticity. With an increase in flexibility of modern aircraft structures which results in a complex aero-structural interaction, aeroelastic effects must be taken into consideration from the preliminary design phase in order to avoid expensive redesign during subsequent design phases. There will also be greater weight penalties that is required to satisfy aeroelastic requirements, such as flutter and divergence, if they have not been previously accounted for. As a result, the design process at the later phase may be costly to be redesigned. Therefore, in order to obtain realistic wing structural layout and sizes, it is necessary to use aeroelastic optimisation including aero-structural interaction in conjunction with a complete set of real-world constraints.

1.3 Thesis Overview

The work in this thesis is concerned with designing and optimising the internal configuration of high aspect ratio wings. The problem studied is the minimisation of wing mass subject to compliance and flutter constraints.

$$\begin{aligned} &\text{Minimise:} && M_w \\ &\text{Subject to:} && G_f \leq 0 \quad , \quad q_{min} < q < q_{max} \\ & && C^* \leq C_{lim} \end{aligned} \tag{1.1}$$

where M_w is the wing mass, G_f is a continuous function, q_{min} and q_{max} are minimum and maximum dynamic pressure within range of interest, C^* is the target compliance value, C_{lim} is the limit on the compliance.

Flutter is a dynamic aeroelastic phenomenon caused by the interaction between aerodynamic loading, structural forces, and inertial forces (Wright and Cooper 2007). It is an unstable self-excited vibration in which the structure extracts energy from the air stream and often results in catastrophic failure. Flutter can take various forms involving different pairs of interacting modes, such as wing bending or/and torsion modes.

The compliance of a structure is equivalent to its stiffness under loading conditions. It is also equivalent to the internal strain energy or the work done by the surface tractions and body forces. By considering the compliance as constraint, the wing structures produced by solving Eq. (1.1) provide an optimal arrangement of the available material in order to minimise wing mass. This approach produces optimal structures in the sense that all of the available material inside the wing is utilised in a useful manner by supporting the aerodynamic loading conditions. This is a useful concept, especially in the preliminary design stage, when the general layout of the wing box is yet to be determined.

The aeroelastic optimisation problem is studied within the following scope:

(i) Three dimensional linear elastic structures.

(ii) Static aerodynamic loading distribution from a chosen flight condition.

(iii) Level set based structural topology optimisation method.

Within this scope, the key contributions of this thesis are:

(i) Sensitivity analysis of continuous flutter constraint and mode tracking method that are applicable for used with the level set based optimisation method, (Chapter 4).

(ii) Implementation of an improved eigenvector orthogonality correlation method for mode tracking in flutter analysis, (Chapter 5).

(iii) Investigation and development of effective modal mass method that eliminates the localised modes for high aspect ratio wings during the aeroelastic optimisation, (Chapter 6).

(iv) Implementation of a level set optimisation method to solve multiple constraints, such as compliance and flutter for high aspect ratio wings, (Chapter 7).

Chapter 2

Background and Literature Review

2.1 Introduction

The purpose of this chapter is to critically review the relevant literature and to provide deeper background in the methods and ideas throughout this thesis. The review consists of three main parts. The first part provides an overview of the development of aeroelastic optimisation and the various approaches to the problem formulation. The second part describes the level set method for topology optimisation in more detail with current trends and developments. The third part discusses the state-of-the-art of aeroelastic topology optimisation, which includes the challenges and issues that are known in the literature. The chapter concludes with some remarks on the literature that are used to motivate the research presented in this thesis.

2.2 Aeroelastic Tailoring and Optimisation

The application of optimisation to the aircraft design structures with aeroelastic effects considered such as aero-structural interaction, divergence, flutter and limit cycle oscillation (LCO) is called aeroelastic optimisation. Before outlining the optimisation procedure, it is important to review the internal wing box structural configuration have been considered for aeroelastic design and optimisation in the literature.

2.2.1 Aeroelastic Tailoring and Optimisation of Wing Box Structure

The term aeroelastic tailoring is defined by Shirk et al. (1986) as "*the embodiment of directional stiffness into an aircraft structural design to control aeroelastic deformation, static or dynamic, in such a fashion as to affect the aerodynamic and structural performance of that aircraft in a beneficial way,*". Traditionally, aeroelastic tailoring has been achieved with composite plate or shell structures via bend-twist coupling, causing either wash-in effect (wing tip leading edge goes up) or wash-out effect (wing tip leading edge goes down) (Jutte et al. 2015). The primary stiffness direction of the composite wing can be achieved by tailoring either the laminate thickness distributions or the fibre orientation angle of the composite material. This effect can be seen on the aerodynamic and structural attributes, many of which can only be improved at the expense of others (Shirk et al. 1986). The work in the past few decades by Hollowell and Dugundji (1984), Weisshaar (1987) and Weisshaar and Ryan (1986) focused on stiffness-based methods via composite materials, although the mass distribution can have a large effect upon the aeroelastic behaviour as well. For example, Stanford and Beran (2011) shows that having some masses around tip leading edge can increase the aeroelastic stability of the wing. Therefore, by considering the parameters that affect both stiffness and mass distributions at an early stage may be expected to provide more superior structures compared to traditional design methods. With the aid of vast development of computational requirements and optimisation

techniques, there have been many attempts to explore aeroelastic optimisation of wing box structures.

Aeroelastic optimisation is particularly important in designing a wing box structure because the wing box design process involves interactions among several disciplines such as aerodynamics, structural analysis, and aeroelasticity. The optimisation problem that is related to a wing box design, involves multiple objectives and constraints pertaining to the design criteria associated with each one of these disciplines (Gasbarri et al. 2009). Some approaches consider simple constraint such as volume, whilst optimising objectives such as compliance (Balabanov and Haftka 1996; James and Martins 2012), natural frequency (Gomes and Suleman 2008), aileron reversal speed (Stanford and Dunning 2014) and aeroelastic stability (Stanford and Beran 2011; Dunning et al. 2014). Stodieck et al. (2013) and Stodieck et al. (2015) examined the effects on free vibration, flexural axis, flutter and divergence speeds on an unswept wing by tow steering the composite fibre orientations along the wing span. In the other words, these approaches improve the wing performance and achieve the aeroelastic stability whilst satisfying a target wing volume or mass.

Another primary application for aeroelastic optimisation procedure is the design of wing box structures with mass minimisation subject to multiple types of aeroelastic stability constraints such as flutter and divergence (Stroud et al. 2002; Arizono and Isogai 2005; Chedrik et al. 2010; Kennedy et al. 2014; Dunning et al. 2014). Wing mass is widely chosen as a primary objective to be minimised because reducing the wing mass will reduce the fuel consumption. There have been many studies attempted to minimise wing mass via structural optimisation of thickness distribution of a beam of plate. Examples include Seyranian (1982) and Butler and Banerjee (1996), where a beam modelled is coupled with strip-theory aerodynamics, Barboni et al. (1999) and Pastilha (2007) model the wing as a simple supported panel under supersonic flow via piston theory, and Stroud et al. (2002) develop a plate model coupled with a doublet lattice method for

reliability-based design. Odaka and Furuya (2005) study the aeroelastic stability of a clamped delta wing under supersonic flow via piston theory.

In more recent years, higher fidelity 3D finite element model has been used to minimise the wing mass under an aeroelastic stability constraint. This allows even greater freedom to determine the sizes of wing skins, ribs and spars, or even the entire internal configuration inside the wing box if topology optimisation method is employed. The parameters of wing box layout including spar position, skin thickness and spar section sizes have direct or indirect effects on aerodynamic characteristics, structural stiffness, and structural strength. For example, Chedrik et al. (2010) optimise the thickness of wing skin using both metallic and composite materials subject to von Mises stress and flutter constraints. Maute and Allen (2004) and Stanford and Dunning (2014) optimise a rib and spar type wing structure, where the layout of ribs and spars are fixed. Krog et al (2004) focus on optimising individual rib sections along the wing span. Arizono and Isogai (2005) optimise the spars, ribs, and skin thicknesses for 2D composite wings. All these studies are based on a conventional wing box structure.

As aforementioned, topology optimisation can be used to explore novel configurations for the wing because the entire 3D wing box space is considered as the design domain. There are few examples of topology optimisation being employed to design the entire wing box structure. The approach by Eves et al. (2009) utilises topology optimisation to design the layout of major internal structural members for non-conventional wings under aerodynamic loading with deflection, manufacturing and volume constraints. Skin buckling is prevented by having a separate stage of rib pitch optimisation.

2.2.2 Importance of Aero-Structural Interaction

The first stage uses an aerodynamic solver to compute the pressure distribution over a wing during one flight condition. This load is subsequently applied to the structural model to compute the static displacement of the wing. The displacement

vector can then be stored to compute the classical topology optimisation objectives such as compliance. As the wing is deformed, the second stage uses the displacement vector to feed into the aerodynamic solver, and new aerodynamic loading is updated. This process is repeated until the work done on both aerodynamic and structural models are equivalent.

In order to obtain realistic wing box layout and sizes, it is important to use aeroelastic optimisation including aero-structural interaction. The earlier works by Balabanov and Haftka (1996), Eschenaur and Olhoff (2001) and Eves et al. (2009) compute the pressure distribution for an assumed wing shape and do not consider for aero-structural interaction. In recent years, Maute and Allen (2004) designed wing stiffeners using a 3D Euler aerodynamic solver and a linear finite element model to minimise wing mass subject to lift, drag and structural displacement constraints. Two cases are considered in the study, one with constant aerodynamic loading, and the second case is with aero-structural interaction. Figure 2.1 shows the optimum material distribution for two cases, where both cases lead to different stiffeners layout. The black regions in both figures represent solid materials, whereas the grey colour represent void regions. While the lift is approximately the same for both cases, the drag of the constant aerodynamic loading optimum wing is more than twice as large as the drag of the aero-structural interaction optimum wing. This work is later extended by Maute and Reich (2006) to optimise morphing aerofoils but account for large deformation in the structural model.

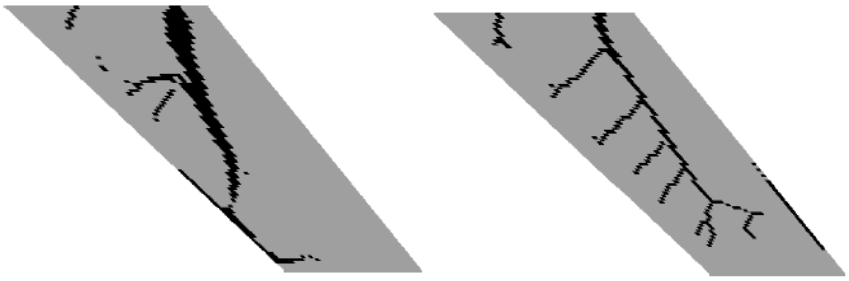

Figure 2.1: Optimum material distribution – left: case aero-structural interaction, right: case constant aerodynamic loading (Maute and Allen 2004).

It is important to transfer aerodynamic loads and structural displacements between the aerodynamic model and structural model accurately during the optimisation. Several numerical methods such as least squares technique for interpolation (Schmitt 1956), polynomial fit (Rodden 1959), finite plate spline (Appa 1989), surface spline (Harder and Desmarais 1972), radial basis function (Rendall and Allen 2008) and inversed isoparametric mapping (Pidaparti 1990) have been developed to transfer the information between the aerodynamic and structural meshes. Brown (1997) uses an extrapolative technique to transfer the interactive data between the high fidelity computational fluid dynamics (CFD) mesh and computational structural mechanics (CSM) finite element model. In all of these numerical methods, a system of equations has to be solved to compute the required information between the aerodynamic or structural meshes. Consequently, these methods are used widely and become very popular interfacing algorithms in the field of aeroelasticity.

2.3 Level Set Based Topology Optimisation

2.3.1 Introduction

The level set method was originally developed as a mathematical tool for computing the motion of interfaces in two or three dimensions (Sethian 1999). The interfaces are represented by an implicit function that can be easily updated under a velocity field to track the motion of the interfaces. This method allows for complicated phenomena to occur, for example, interface merging or splitting. Therefore, the level set method is attractive to a wide range of applications where the dynamic movement of interfaces is accurately and efficiently computed.

The level set method is also suitable for boundary based topology optimisation, where interfaces becomes structural boundaries and the velocity field is derived from shape sensitivity analysis to propagate the design towards an optimal design (Dunning 2011). The level set method has been applied to structural topology optimisation and aeroelastic topology optimisation in recent years to optimise

various structural designs. This section details the fundamental theoretical aspects of the level set method in the context of aeroelastic topology optimisation.

2.3.2 Level Set Method Fundamental Principles

The boundary of the structure is defined as the zero level set of an implicit function:

$$\begin{cases} \phi(x) \geq 0, x \in \Omega \\ \phi(x) = 0, x \in \Gamma \\ \phi(x) < 0, x \notin \Omega \end{cases} \tag{2.1}$$

where Ω is the domain for the structure, Γ is the boundary of the structure, $\phi(x)$ is the implicit function and $x \in \Omega_d$, where Ω_d is the design domain containing the structure, $\Omega \in \Omega_d$. This implicit description allows the boundary to break and merge naturally, allowing topological changes to occur during optimisation. The implicit function is initialised as a signed distance function, where the magnitude is the distance to the boundary and the sign is defined by Eq. (2.1).

The position, shape and topology of the structure boundary is optimised by iteratively solving a Hamilton-Jacobi type equation:

$$\frac{\partial \phi(x)}{\partial t} + \nabla \phi(x,t) \frac{\partial x}{\partial t} = 0 \tag{2.2}$$

where t is the fictitious time domain. If Eq. is discretised and solved using explicit forward Euler scheme, the following update rule for the discrete implicit function values is obtained:

$$\phi_i^{k+1} = \phi_i^k - \Delta t \left| \nabla \phi_i^k \right| V_n \tag{2.3}$$

where k is the current iteration number, i is a discrete point in the design domain, Δt is a discrete time step, and V_n is a velocity function defined normal to the boundary, such that a positive velocity moves the boundary inwards. The sign convention is used throughout this thesis. The change in shape through a velocity

function is only dependent on the component normal to the boundary and therefore only this part will be considered during optimisation (Allaire et al. 2004).

2.3.3 Review of Level Set Method for Constraint Problems

A number of practical engineering problems often involve multiple constraints. There have been various approaches developed to handle constraints in level set based optimisation. Some approaches are limited to problems with a single constraint, such as the compliance or the maximum volume. Allaire et al. (2004) propose that a constraint can be added to the objective using a fixed Lagrange multiplier. However, this is very similar to a penalty method, which cannot guarantee the constraint is satisfied. Wang et al. (2003) obtain the Lagrange multiplier with the assumption of the volume remains constant during the level set update although conserving the volume with the level set method can be difficult. This method can be improved by using Newton's method to correct the Lagrange multiplier if the constraint becomes infeasible (Osher and Santosa 2001). Dunning and Kim (2013) explicitly compute the Lagrange multiplier every iteration using a one dimensional optimisation technique to ensure constraint feasibility.

The methods discussed so far have been applied to a single constraint problems. A gradient projection method has been used to handle multiple constraints problem, where the decent direction of the objective function is projected onto the tangential space of the active constraints (Wang and Wang 2004). Examples of the gradient projection method used in the level set optimisation are multiple volume constraints for multiple materials (Wang and Wang 2004) and volume and input displacement constraints for compliant mechanism design (Mei and Wang 2004). Luo et al. (2008) take another approach to handle multiple constraints by using the augmented Lagrangian multiplier method. However, Zhu et al. (2010) show that the choice of the penalty parameters can affect the overall optimisation efficiency and convergence.

A new approach for handling multiple constraints in the conventional level set topology method is developed by Dunning and Kim (2015). It is known as the Sequential Linear Programming (SLP) level set method. The key features of this method are discretised boundary integrals to estimate function changes and the formulation of an optimisation sub-problem to attain the velocity function (Dunning and Kim 2015). This approach does not require penalty parameters and has an additional benefit to optimise non-level set design variables.

2.4 Aeroelastic Topology Optimisation

2.4.1 Introduction

There are several methods to structural topology optimisation. The most popular topology optimisation method applied to aircraft wing design is the Solid Isotropic Material with Penalisation (SIMP) method (Bendsøe and Sigmund 2004). This is undertaken by discretising the wing box into finite elements, and each element is assigned as a design variable. The design variable represents the element density which may vary from 0 (void) to 1 (solid). The stiffness of each element is simply scaled proportionally to its density value and therefore this approach can produce optimal designs with a significant amount of intermediate density material around the structure boundary (Dunning et al. 2015). However, these boundaries with intermediate densities can make it difficult to interpret solutions as continuous solid structures, without using heuristic post processing methods (Tang et al. 2001). This is particularly noticeable when the optimisation problem involves multiple constraints and aero-structural interaction (Maute and Allen 2004; James et al. 2014). Due to the limitation of SIMP method, some alternative methods have been developed to address this challenge.

Kobayashi et al. (2010) develop a cellular division method to design the wing box of a fighter aircraft. This is a biological inspired method that does not require sensitivity analysis and hence it can be applied to a wide range of problems. However, one drawback of this method is that the convergence can be slow, as the

search is not directed by the sensitivities. Another recent approach that has been attracting significant attention is the level set based topology optimisation method (Allaire et al. 2004; Wang et al. 2003; van Dijk et al. 2013). The level set method defines the structure using an implicit function and produces solutions with clear boundaries with no intermediate density material. The implicit function also allows boundary merging and splitting in a continuous manner. The level set method always defines clear boundaries and therefore avoid solutions with intermediate densities (Dunning et al. 2013).

The level set method has been applied to wing optimisation considering aeroelastic effects. For example, Gomes and Suleman (2008) use the spectral level set method to optimise skin reinforcement for enhanced roll manoeuvres. Duan et al. (2012) use the level set method to minimise the compliance of a 2D plate-like wing subject to volume constraint, however aero-structural interaction is not considered. Minimisation of compliance is also considered by James and Martin (2012) using an isoparametric level set method subject to the static aerodynamic loads for 3D wing. Brampton et al. (2012) apply level set based optimisation to a simple 3D wing model with coupled aerodynamic and structural analysis. The work is later proceeded by Dunning et al. (2014) to minimise the compliance of a more realistic 3D wing box under static aeroelastic and self-weight body force loading. A 3D unstructured level set method is developed to optimise the entire volume of the 3D wing box and thus the solution is not restricted by a predefined structural layout (Dunning et al. 2015). As the level set method has been more maturely developed, researchers attempt to apply this method to overcome more sophisticated wing optimisation problem with the consideration of dynamic aeroelastic stability such as flutter. Two main issues are identified and discussed in this chapter. The first issue is concerned with mode switching found in flutter problem during topology optimisation, the second discusses the local modes phenomenon due to the dynamic characteristics of the wing box.

2.4.2 Mode Switching Problem

In the recent work by Dunning et al. (2015), the Sequential Linear Programming (SLP) level set topology optimisation method is developed to design an aircraft wing considering skin buckling under static aeroelastic loads and flutter. The optimisation problem involves minimisation of wing mass subject to a flutter constraint. When performing flutter constraint optimisation, typically more than 15 modes are chosen in order to predict the critical flutter points (Stanford and Beran 2011; Dunning et al. 2015). It is well known that in aeroelastic flutter problems, the flutter point is defined as the flight speed at which one of the eigenvalues in a particular mode becomes dynamically unstable (positive real part of the eigenvalue). However, there are potentially more than one eigenvalues that can become unstable. As a result, there may be discontinuities in the design space because of mode switching. In topology optimisation, every iteration requires computation of flutter sensitivity and mode switching problem changes the sensitivities drastically between the iterations, and hence it will slow down the convergence of the optimisation. An example of mode switching problem between the iterations is shown in Figure 2.2 taken from Stanford et al. (2014), where q is the dynamic pressure, and g is the real part of each eigenvalue. A direct method to solve this problem is to have a larger design space by increasing the range of the dynamic pressure, q to capture all possible flutter points.

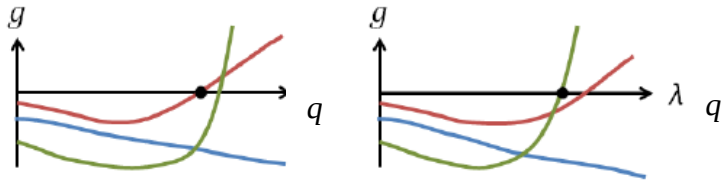

Figure 2.2: Mode switching: change in critical flutter points from one design iteration (left) to the next iteration (right) (Stanford et al. 2014).

Alternatively, the flutter mode may switch in such a way that the flutter speed drastically decreases. This is shown in Figure 2.3 (Stanford et al. 2014), where the lower flutter point manifests itself through a “hump mode” (Stanford et al. 2014).

Point A in Figure 2.3 (left) represents the flutter point as it crosses the $g = 0$ line, whereas point B is not a crossing and therefore it does not represent a flutter point. It is, however, possible that a change in a structural parameter may cause the peak at point B to shift upwards and cross the $g = 0$ line (Haftka 1975), as shown in Figure 2.3 (right). This is a severe discontinuity in the design space which causes the gradient based optimiser to be entirely ineffective and hence fails to converge.

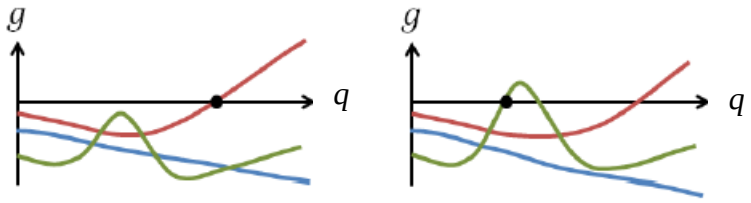

Figure 2.3: Mode switching: change in critical flutter points due to hump mode from one design iteration (left) to the next iteration (right) (Stanford et al. 2014).

Langthjem and Sugiyama (1999) and Odaka and Furuya (2005) have utilised a series of frequency separation constraint to prevent the mode switching during the optimisation for higher mode flutter. Higher mode flutter usually occurs when two oscillatory frequencies are coalesced. A frequency separation constraint is imposed to keep the frequencies separated and prevent the associated discontinuities. Figure 2.4 illustrates how the frequencies, ω between the modes are separated (Stanford et al. 2014). For every value of q starting from 0 to the critical flutter point, the oscillatory frequencies (imaginary part of eigenvalues) of modes 2 and 3 must always be separated by some margin. The same constraint is imposed between modes 3 and 4, modes 4 and 5, etc., up to the number of eigenvalues retained in the analysis (Stanford et al. 2014). However, flutter is also observed to occur without coalescence of two frequencies, particularly for cases with strong pre-flutter aeroelastic damping which is neglected by Odaka and Furuya (2005). Mode switching can still occur even though large frequency separation constraint is imposed.

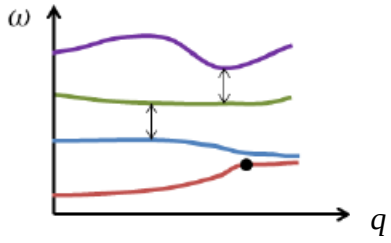

Figure 2.4: Frequency separation constraints (Stanford et al. 2014).

Another solution introduced by Haftka (1975) is to enforce a series of critical damping constraints. For every value of dynamic pressure q between 0 and the flutter point, the damping (real part of eigenvalues) of mode 2, 3, 4, etc. must always be less than some threshold shown by the dashed line on Figure 2.5 (Stanford et al. 2014). The advantage of this constraint is to prevent the mode switching of Figure 2.2 and the hump mode of Figure 2.3.

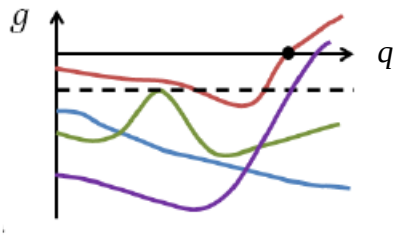

Figure 2.5: Critical damping constraints (Stanford et al. 2014).

2.4.3 Local Modes Phenomenon

The fixed grid method is usually used in topology optimisation so that in the final design, the element in the finite element model should either be a solid element or a void element. This leads to a number of problems because there is a large difference in the mass and stiffness of the void and solid elements. One idea is to remove the void elements from the finite element model when they become void. However this cannot be achieved in topology optimisation because the algorithm must be allowed to add material to these low density areas. Once the elements are removed from the algorithm, it is not possible to add them back.

The SIMP method is proposed to reduce the some of the element densities which result in a mixture of void and solid elements on a fixed grid. For the level set method, although the method produces a clear boundary, the element can still be cut and create some void around the element. This can reduce the element density dramatically. Although the final design consists of both solid and void elements, the physical behaviour is desired to be controlled solely by the solid elements. One physical behaviour could be the eigenfrequencies or flutter of a design (Neves et al. 1995). Low density areas are very flexible compared with areas with full densities, and will therefore control the lowest eigenmodes of the entire structure. As a result, there is the possibility of what could be termed local modes. Local modes are characteristic for designs where there is a high variation of densities, and they are also present in a final solid and void design (Pederson 2000). In reality, these local modes are completely non-existent since the low density area represents a void region in the structure.

There have been some attempts to resolve the local modes problem. For example, Pedersen (2000) proposes a solution in which the ratio between the density and the elastic modulus associated with low density elements was set to be a constant value. Tcherniak (2002) avoids local modes by setting the density values to zero for low density elements. Du and Olhoff (2007) place a heavier penalty on the density when the relative density is below the threshold. Stolpe and Svanberg (2001) use a material interpolation model based on a rational function to penalise the elemental density. The methods described above can be classified into constructing a more suitable penalty function of the density, which could reduce the local modes problem. However, this does not totally eliminate the local modes, and the penalty function parameters must be adjusted depending on the specific optimisation problems. Besides, these methods are developed for SIMP topology optimisation method, but they are not suitable for the level set topology optimisation method.

In the aeroelastic topology optimisation model, if flutter is imposed as a constraint, the free vibration analysis must be performed first to compute the order

of the global modes because of the dynamic characteristics. The order of the global modes can be confirmed by mode identification technology. Clough and Penzien (1975) define the effective modal mass method to identify the global modes, and it is used by different industries in different ways. Yuan (2004) compute the effective modal mass fraction in satellite design to identify the global modes and the local modes. Li et al (2015) further extend the research on the satellite design by adding the effective modal mass method to form an improved optimisation model. With the information of effective modal mass fraction, whether the constraints in the optimisation are set correctly or not can be checked. One limitation in this method is that a tolerance value has to be set to separate the global modes and the local modes, depending on the optimisation problem. The effective modal mass method will be used in this thesis and the procedure will be discussed in more detail in Chapter 5.

2.5 Conclusions

Aeroelastic optimisation is important in designing wing box structure because the wing box design process involves a number of discipline such as aerodynamics, structures and aeroelasticity. There has been many research on optimising the conventional wing box design, such that the thickness of skins and spars, position of ribs are the design parameters. With the aid of vast development of computational requirements and optimisation techniques, the topology optimisation method is used to optimise the wing box structure because it allows more freedom to design the internal structural layout. In addition, aero-structural interaction has been considered in many cases so that the problem is closer to the reality.

The level set based topology optimisation is a boundary based method of topology optimisation where an implicit function usually represents the structural shape. The level set method has been used to solve aeroelastic topology optimisation, including compliance, divergence and flutter problems, limit cycle

oscillations and aileron reversal problems. Sensitivity analysis of the objective and constraints at the nodal points are usually computed and interpolated to the structural boundaries. The conventional level set method can handle a single constraint problem by adding the constraint into the objective by using a Lagrange multiplier. However, this method struggles to handle multiple constraints problem. Sequential Linear Programming (SLP) level set method has been developed to handle more complex problems with multiple constraints.

Although aeroelastic topology optimisation provides more freedom to optimise the wing structure, there are some issues exist in this types of problem. Firstly the optimisation problem subject to a flutter constraint may have a mode switching issue. Mode switching can cause a discontinuity during the optimisation and hence slow down the convergence. Another issue is known as the 'hump mode', where it is commonly found in high aspect ratio wings. Although the past literature has introduced frequency separation and damping separation methods to prevent mode switching, these methods are applicable to certain type of problems. In level set topology optimisation, there may be some finite elements in the structural domain that are cut and these cut elements means that the stiffness of that element is reduced. The reduced stiffness elements can cause local mode phenomenona. There have been some attempts to solve the local modes problem for SIMP topology optimisation method. An alternative method must be developed to eliminate the local modes for level set topology optimisation method.

2.6 Research Aims and Objectives

The aim of this research is to design and optimise the internal configuration of high aspect ratio wings using level set based aeroelastic topology optimisation. Considering the scope of this thesis and the conclusions of the literature review, the research objectives are listed below:

(i) To derive and implement an aeroelastic analysis including the aero-structural interaction for the 3D high aspect ratio wings.

(ii) To derive and implement a compliance and flutter sensitivity analysis that can be applied to the level set based topology optimisation.

(iii) To investigate the dynamic problems such as mode switching, hump modes, and local modes for the high aspect ratio wings during the aeroelastic topology optimisation.

(iv) To use the SLP level set method to optimise the internal configuration of high aspect ratio wings. Both compliance and flutter constraints will be added in the optimisation problem. Finally a series of parametric studies will be conducted for various high aspect ratio wings.

Chapter 3

Aeroelastic Analysis

3.1. Introduction

This chapter describes the analysis tools that are used in the aeroelastic design framework. The analysis tools consist of aerodynamic solver, structural solver, procedure for aero-structural coupling and dynamic flutter solver.

3.2. Aerodynamic Analysis

Computational cost is a major concern since each module may be required to perform hundreds of evaluations during aeroelastic optimisation depending on the number of design variables. Some well-known methods such as Euler and Navier-Stokes analysis for fluid flow are too costly. Instead, the Doublet Lattice Method (DLM) has been employed, as it is relatively simple to implement and there are significant savings in solution time.

The DLM was formulated by Albano and Rodden (1969) to calculate unsteady aerodynamic loading and it has been widely used for aeroelasticity analysis of aircraft at subsonic speeds. It is part of family techniques which employ the incompressible, inviscid and irrotational form of the Navier-Stokes equations, simplifying to the Laplace equation of potential flow. Roughen *et al.* (2001) have compared the results between doublet lattice, Navier-Stokes and experimental data. The results indicate a relatively good agreement between these two methods with the experimental data for purely subsonic condition.

3.2.1. Doublet Lattice Method

The DLM is a finite element method for the solution of the oscillatory subsonic pressure-downwash integral equation for lifting surfaces (Albano and Rodden, 1969):

$$\bar{\boldsymbol{w}}(x,\xi) = \frac{1}{8}\sum_{n=1}^{N}\iint_{S} \Delta\bar{\boldsymbol{p}} \cdot \Im(x,\xi;s,\sigma;k,M_\infty)\, d\xi d\sigma \tag{3.1}$$

where $\Im(x,\xi;s,\sigma;k,M_\infty)$ represents the kernel function. The kernel function is a function of the coordinate system of a lifting surface, (x,ξ) and (s,σ) as shown in Figure 3.1, reduced frequency, k and Mach number M_∞. The other part of the integrand, $\Delta\bar{\boldsymbol{p}}$, is the pressure difference across the surface. The left hand side $\bar{\boldsymbol{w}}(x,\xi)$, is the geometric normalwash which is calculated from the prescribed motion of the surface. The integration is carried out over the wing surface, S. Note that the reduced frequency in this context is defined as:

$$k = \frac{\omega \cdot c}{U_\infty} \tag{3.2}$$

where ω as the harmonic frequency, c the reference chord length, and U_∞ the freestream velocity.

The derivation of the theory behind the DLM presented here follows very closely to Albano and Rodden (1969), Kalman *et al.* (1970) and Rodden *et al.*

(1972). The method divides the lifting surfaces into small trapezoidal elements (panels) such that the panels are arranged in strips parallel to the free stream, as shown in Figure 3.2. There are a few basic assumptions made in the application of the DLM for subsonic flow:

(a) The geometry is assumed to be symmetric – only the right wing is represented (Figure 3.1).

(b) The lifting pressure with an unknown strength is assumed to be concentrated along the ¼-chord line on each panel surface (Figure 3.2). The flow tangency boundary condition is satisfied at a control point located in the middle of the ¾-chord line on each panel.

(c) The steady flow effects are represented by a horseshoe vortex on each of the panels whereas the incremental oscillatory effects are represented by a distribution of acceleration potential doublets, which is equivalent to a pressure jump across the surface.

(d) The DLM theory breaks down when applied to a highly flexible wing as the lift vector is no longer vertical (Howcroft 2016).

Based on the assumptions described above, the numerical form of the integral equation, Eq. (2.1), can be written in matrix notation as:

$$\boldsymbol{D} \cdot \Delta\overline{\boldsymbol{p}} = \overline{\boldsymbol{w}} \tag{3.3}$$

where $\boldsymbol{D}$ is the non-dimensional downwash factor matrix. From Eq. (3.3), the inverse of the $\boldsymbol{D}$ matrix is known as the aerodynamic influence coefficient matrix (AIC). The AIC matrix can be used to calculate the pressure distribution and the aerodynamic lift (Silva *et al.*, 2008).

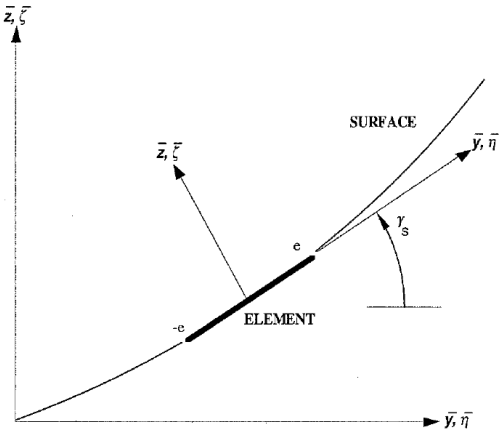

Figure 3.1: Lifting surface coordinate system (Rodden et al., 1972).

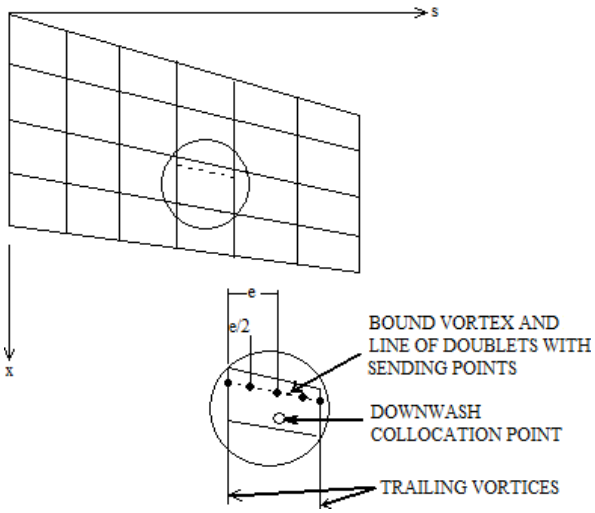

Figure 3.2: Idealisation of the lifting surface using trapezoidal boxes (Rodden *et al.*, 1972).

3.2.2. Calculation of Aerodynamic Lift

There are three sources of downwash at each control point, $\boldsymbol{w_c}$ is the slope of the aerofoil centreline (from built-in camber and twist), α is the angle of attack at the wing root, and $\boldsymbol{w(u)}$ is the additional downwash dependent on the deformed shape of the wing. Therefore, the downwash $\bar{\boldsymbol{w}}$ in Eq. (3.3) can be expressed as:

$$\bar{\boldsymbol{w}} = \boldsymbol{w_c} - \alpha \cdot \boldsymbol{z} + \boldsymbol{w(u)} \tag{3.4}$$

where $\boldsymbol{z}$ is the column vector of ones. The aerodynamic lift force can be evaluated by combining Eq. (3.3) and (3.4), and multiplying with the dynamic pressure q_∞ and integration matrix $\boldsymbol{S}$:

$$\boldsymbol{L}(\boldsymbol{u}) = q_\infty \cdot \boldsymbol{S}^T \cdot \boldsymbol{D}^{-1}\{\boldsymbol{w_c} - \alpha \cdot \boldsymbol{z} + \boldsymbol{w}(\boldsymbol{u})\} \tag{3.5}$$

where the dynamic pressure q_∞ is a scalar function of air density, ρ_{air} and freestream velocity, U_∞:

$$q_\infty = \frac{1}{2} \cdot \rho_{air} \cdot U_\infty^2 \tag{3.6}$$

3.3. Structural |Analysis

The structure of the aircraft wing is typically modelled by a wing box as it carries approximately 80% of the structural loads. The wing box model must be able to represent its structural behaviour to yield the displacements, natural frequencies, and mode shapes.

3.3.1. Finite Element Method

The finite element method (FEM) is a technique that discretises the wing box into one of more sets of basic structural components. Each set of the component exhibit a similar geometry and physical properties that corresponds to a specific type of finite element. The finite elements are connected to adjacent elements by nodal points. When forces are applied on the nodal points, the node is subjected to displacements which represent the degrees of freedom. Each element is formed by a few nodal points. Then the entire structure is formed by physically assembling these elements. This results in a large set of simultaneous equations which can be solved numerically. After applying the loads and boundary conditions, the set of equations can be written as:

$$\boldsymbol{K}(\boldsymbol{\Omega}) \cdot \boldsymbol{u} = \boldsymbol{f_t}(\boldsymbol{u}, \boldsymbol{\Omega}) = \boldsymbol{f_a}(\boldsymbol{u}, \boldsymbol{\Omega}) + N \cdot \boldsymbol{f_g}(\boldsymbol{\Omega}) \tag{3.7}$$

where $\boldsymbol{K}$ is the global stiffness matrix of the wing structure, $\boldsymbol{\Omega}$ is the structural design variables, $\boldsymbol{u}$ is the vector of nodal displacements, N is the load factor (N = 1 is the steady level flight), and $\boldsymbol{f}_t$ is the vector of total loads applied on the structure. The global stiffness matrix is assembled by superimposing the element stiffness matrices. If the row and columns of the global stiffness matrix corresponding to fixed degrees of freedom are eliminated, then the matrix is symmetric and non-singular. The total loads can also be decomposed into aerodynamic load vector ($\boldsymbol{f}_a$) and gravity load vector due to the wing weight ($\boldsymbol{f}_g$)

The vector $\boldsymbol{u}$ in Eq. (3.7) represents the global displacements of the wing structure. To determine the displacement field within an element, finite element theory assumes shape functions that interpolate the nodal displacements, the simplest of which are linear functions. The displacement of any point $\boldsymbol{x}$ in the structure can be written as:

$$\boldsymbol{u}(\boldsymbol{x}) = \sum \boldsymbol{N}_e \cdot \boldsymbol{u}_e \tag{3.8}$$

where $\boldsymbol{N}_e$ is the shape functions for each element and $\boldsymbol{u}_e$ is the vector of nodal displacements for that particular element.

The strains at the element level depend on the nodal displacements in Eq. (3.8):

$$\boldsymbol{\varepsilon}_e = \boldsymbol{B}_e \cdot \boldsymbol{u}_e \tag{3.9}$$

where $\boldsymbol{B}_e$ represents the strain-displacement matrix and is obtained by differentiating the shape functions $\boldsymbol{N}_e$ with respect to the point $\boldsymbol{x}$.

The compliance of the structure is computed using elemental strain vector in Eq. (3.9):

$$\boldsymbol{C} = \sum E \cdot \boldsymbol{\varepsilon}_e(\boldsymbol{u}_e) \cdot \boldsymbol{\varepsilon}_e(\boldsymbol{u}_e) = E \cdot \boldsymbol{\varepsilon}(\boldsymbol{u}) \cdot \boldsymbol{\varepsilon}(\boldsymbol{u}) \tag{3.10}$$

where E is the material property tensor.

3.3.2. Wing Box Structural Model

The wing box is created in 3D in order to capture the topology of the internal configuration during the optimisation. Shell elements are used for the top and bottom skin, as well as the front and rear spars. These shell elements are treated as fixed variables, which means they will not be varied throughout the optimisation. Solid elements are used for the structural domain inside the wing box.

When discretising the 3D model, finite elements of high aspect ratios: elongated or "skinny" elements are avoided. The aspect ratio of a 3D element is the ratio between its largest and smallest dimension. This is to reduce the numerical errors in the finite element analysis. In this study, the aspect ratio of each element is set to be less than five (Rodden and Johnson 1995).

3.4. Aero-structural Analysis Coupling

The coupling of the aerodynamic and structural solvers is one of the most important in the aeroelastic optimisation. This is because the aerodynamic solution depends on the position and shape of the solid boundary, which is affected by the structural displacements. The structural displacements which in turn depend on the aerodynamic loading applied to the structure. However, due to the different set of grid points between the DLM and the FEM, a finite plate spline method is implemented to connect those grid points to ensure the loads and displacement information is accurately transferred.

3.4.1. Finite Plate Spline Method

The Finite Plate Spline (FPS) method (Appa 1989) is used to communicate the loads and displacements information between the DLM and the FEM meshes. A flat plate finite element mesh is constructed between the DLM and FEM discretisation. Discrete Kirchoff Triangular (DKT) plate elements (Cook et al.

2002) are used to form the FPS mesh. Displacement constraints are enforced at locations that coincide with the DLM box centre and a subset of FEM nodes. Solving the FPS finite element equation under these displacement constraints allows the formulation of two transfer matrices that relate the aerodynamic and structural quantities:

$$\boldsymbol{f}_a = q \cdot \boldsymbol{T}_l \cdot \Delta \boldsymbol{p} \tag{3.11}$$

$$\boldsymbol{w}(\boldsymbol{u}) = \boldsymbol{T}_u \cdot \boldsymbol{u} \tag{3.12}$$

where $\boldsymbol{T}_l$ is a matrix that computes the work-equivalent loading on the wing structure from the pressure coefficient and $\boldsymbol{T}_u$ is a matrix that converts the structural displacement vector into the downwash component dependent on the deformed wing shape in a work-equivalent method.

At the trim condition, the total lift derived in Eq. (3.5) equals to the total weight of the aircraft:

$$\boldsymbol{L}(\boldsymbol{u}) = q \cdot \boldsymbol{S} \cdot \boldsymbol{D}^{-1}\{\boldsymbol{w_c} - \alpha(\boldsymbol{u}, \Omega) \cdot \boldsymbol{z} + \boldsymbol{w}(\boldsymbol{u})\} = N \cdot (W_b(\Omega) + W_c) \tag{3.13}$$

where N is the load factor, $W_b(\Omega)$ is the weight of the wing box that can change during the optimisation and is dependent on the position of the structural boundary, and W_c is the remaining "fixed" weight of the aircraft.

After re-arranging Eq. (3.13), the required angle of attack for trim condition in terms of the deformed shape of the wing and current wing box weight can be written as:

$$\alpha(\boldsymbol{u}, \Omega) = \frac{L_c + \boldsymbol{b} \cdot \boldsymbol{u} - N \cdot (W_b(\Omega) + W_c)}{L_\alpha} \tag{3.14}$$

where L_c and L_α are constants defined as:

$$L_c = q \cdot \boldsymbol{S}^T \cdot \boldsymbol{D}^{-1} \cdot \boldsymbol{w_c} \tag{3.15}$$

$$L_\alpha = q \cdot \boldsymbol{S}^T \cdot \boldsymbol{D}^{-1} \cdot \boldsymbol{z} \tag{3.16}$$

and b^T is a constant vector defined as:

$$\boldsymbol{b}^T = q \cdot \boldsymbol{S}^T \cdot \boldsymbol{D}^{-1} \cdot \boldsymbol{T}_u \tag{3.17}$$

The two constants L_c and L_α from Eq. (3.15) and Eq. (3.16) can be transferred to the constant load vectors using the load transfer matrix $\boldsymbol{T}_l$:

$$\boldsymbol{f}_c = q \cdot \boldsymbol{T}_l \cdot \boldsymbol{D}^{-1} \cdot \boldsymbol{w_c} \tag{3.18}$$

$$\boldsymbol{f}_\alpha = q \cdot \boldsymbol{T}_l \cdot \boldsymbol{D}^{-1} \cdot \boldsymbol{z} \tag{3.19}$$

The matrices $\boldsymbol{T}_l$ and $\boldsymbol{T}_u$ allow information to pass between the DLM and FEM. In addition, they can be used to formulate an aerodynamic stiffness matrix:

$$\boldsymbol{Q} = q \cdot \boldsymbol{T}_l \cdot \boldsymbol{D}^{-1} \cdot \boldsymbol{T}_u \tag{3.20}$$

Note that the $\boldsymbol{Q}$ matrix is constant for a given wing planform and flight condition, which is defined by Mach number, flight velocity and air density. If the Mach number is changed, then the $\boldsymbol{D}^{-1}$ matrix has to be recomputed to update the $\boldsymbol{Q}$ matrix. If the flight velocity and air density are changed, then the update of $\boldsymbol{Q}$ only involves the dynamic pressure, q, which is a scalar value. The aerodynamic load vector in Eq. (3.7) can be computed from Eq. (3.3), (3.11), (3.18), (3.19) and (3.20):

$$\boldsymbol{f}_a = \boldsymbol{f}_c - \alpha(\boldsymbol{u}, \Omega) \cdot \boldsymbol{f}_\alpha + \boldsymbol{Q} \cdot \boldsymbol{u} \tag{3.21}$$

where $\alpha(\boldsymbol{u},\Omega)$ is defined by Eq. (3.14).

3.4.2. Aero-structural Coupling Convergence

The displacement vector $\boldsymbol{u}$ is computed by solving the static aeroelastic equation:

$$\boldsymbol{K}(\boldsymbol{\Omega}) \cdot \boldsymbol{u} = \boldsymbol{f_t}(\boldsymbol{u}, \boldsymbol{\Omega}) = \boldsymbol{f_a}(\boldsymbol{u}, \boldsymbol{\Omega}) + N \cdot \boldsymbol{f_g}(\boldsymbol{\Omega}) \tag{3.22}$$

where $\boldsymbol{f_t}$ is the total load vector, N is the load factor and $\boldsymbol{f_g}$ is the body load vector due to the wing weight. The global stiffness matrix $\boldsymbol{K}$ is calculated using FEM, and the aerodynamic load vector $\boldsymbol{f_a}$ is calculated in Eq. (3.21).

Although the static aeroelastic equation in Eq. (3.22) is linear, it is solved using an iterative approach. The process starts with the aerodynamic load vector in Eq.

(3.21) computed using an assumed $\boldsymbol{u}$ vector, usually from a previously converged analysis. The deformed wing shape is obtained for the current load vector, which is then used to update the load vector by including the coupling terms. This process is repeated until the difference between the previous and updated load vectors is below a small value. The process can be summarised as:

i. Initialise the total load vector: $\boldsymbol{f}_t^0 = \boldsymbol{f_a}(\boldsymbol{u}^0, \alpha^0) + N \cdot \boldsymbol{f_g}$

ii. Solve the static aeroelastic linear equation: $\boldsymbol{K} \cdot \boldsymbol{u}^{i+1} = \boldsymbol{f}_t^i$

iii. Update the angle of attack using Eq. (3.14) to meet the trim condition for $\boldsymbol{u}^{i+1}$:

$$\alpha\left(\boldsymbol{u}^{i+1}\right) = \frac{L_c + \boldsymbol{b} \cdot \boldsymbol{u}^{i+1} - N \cdot (W_b(\Omega) + W_c)}{L_\alpha}$$

iv. Update the load vector: $\boldsymbol{f}_t^{i+1} = \boldsymbol{f_a}\left(\boldsymbol{u}^{i+1}, \alpha^{i+1}\right) + N \cdot \boldsymbol{f_g}$

v. Check for convergence: $\left\|\boldsymbol{f}_t^{i+1} - \boldsymbol{f}_t^i\right\| < small\ value$

This iterative approach to find the convergence has been shown to be efficient. However, it can be unstable and fail to converge, especially for more flexible and high aspect ratio wings. To overcome this, a non-converging solution is detected by tracking the relative difference in subsequent load vectors. If the solution is not converging, especially if $\left\|\boldsymbol{f}_t^{i+1} - \boldsymbol{f}_t^i\right\| > \left\|\boldsymbol{f}_t^i - \boldsymbol{f}_t^{i-1}\right\|$, then an under-relaxation approach is used to obtain the next vector:

$$\boldsymbol{f}_t^{i+1} = 0.25 \times \boldsymbol{f_a}\left(\boldsymbol{u}^i\right) + 0.75 \times \boldsymbol{f_a}\left(\boldsymbol{u}^{i-1}\right) + N \cdot \boldsymbol{f_g} \tag{3.23}$$

The relaxation factor 0.25 is chosen to give a good compromise between efficiency and stability for the examples studied in this work.

3.5. Flutter Analysis

The equation of motion of the aeroelastic system can be derived based on the equilibrium condition of the unsteady aerodynamic load vector $\boldsymbol{f}_a$:

$$\boldsymbol{M} \cdot \ddot{\boldsymbol{u}} + \boldsymbol{K} \cdot \boldsymbol{u} = \boldsymbol{f}_a(\boldsymbol{u}, \ddot{\boldsymbol{u}}) \tag{3.24}$$

where $\boldsymbol{M}$ is the structural mass matrix which is calculated using FEM. The structural damping is not considered in this study. In Eq. (3.24), the unsteady aerodynamic load, $\boldsymbol{f}_a$ can be written in the form of unsteady matrix (Haviland and Yoo, 1973):

$$\boldsymbol{f}_a(\boldsymbol{u}, \ddot{\boldsymbol{u}}) = q_\infty \cdot \boldsymbol{A}(M_\infty, k) \tag{3.25}$$

where $\boldsymbol{A}(M_\infty, k)$ is the unsteady aerodynamic matrix and is non-linearly dependent on the Mach number M_∞ and reduced frequency k. Substituting Eq. (3.25) into Eq. (3.24) gives:

$$\boldsymbol{M} \cdot \ddot{\boldsymbol{u}} + \boldsymbol{K} \cdot \boldsymbol{u} - q_\infty \cdot \boldsymbol{A}(M_\infty, k) = 0 \tag{3.26}$$

The unsteady aerodynamic matrix in Eq. (3.26) is obtained using the DLM and FPS method (Dunning et al, 2015) :

$$\boldsymbol{A}(M_\infty, k) = \boldsymbol{T}_l \cdot \boldsymbol{D}^{-1}(M_\infty, k) \cdot \left(\boldsymbol{T}_u \cdot \boldsymbol{u} + i \cdot \frac{k}{b} \cdot \boldsymbol{T}_v \cdot \dot{\boldsymbol{u}} \right) \tag{3.27}$$

where $\boldsymbol{T}_v$ is a matrix computed by the FPS method that determines the downwash due to the wing motion normal to the wing planform from the structural velocity vector. The AIC matrix, $\boldsymbol{D}^{-1}$ used in the static aeroelastic analysis, Eq. (3.5) is evaluated for $k = 0$ and is real, whereas the AIC matrix used in Eq. (3.27) is evaluated for $k > 0$ and is complex. The unsteady aerodynamic matrix in Eq. (3.27) can be separated into real and imaginary parts and substitute into Eq. (3.26) such that:

$$\boldsymbol{M} \cdot \ddot{\boldsymbol{u}} - q_\infty \cdot \boldsymbol{A_i} \cdot \dot{\boldsymbol{u}} + (\boldsymbol{K} - q_\infty \cdot \boldsymbol{A_r}) \cdot \boldsymbol{u} = 0 \tag{3.28}$$

where $\boldsymbol{A}_r$ and $\boldsymbol{A}_i$ are the real and imaginary parts of the unsteady aerodynamic matrix, respectively. In the *p-k* method, the motion of the displacement is assumed to be harmonic, i.e. $\boldsymbol{u} = \boldsymbol{\eta} \cdot e^{ikt}$, and then substitute into Eq. (3.28):

$$\left[\left(\frac{U_\infty}{c}\right)^2 \boldsymbol{M} \cdot p^2 + \frac{q_\infty}{k} \cdot \boldsymbol{A_i} \cdot p + (\boldsymbol{K} - q_\infty \cdot \boldsymbol{A_r})\right] \cdot \boldsymbol{\eta} = 0 \tag{3.29}$$

where p is the complex eigenvalue, i.e. $p = i \cdot k$, and $\boldsymbol{\eta}$ is the eigenvector. Eq. (3.29) is usually not solved directly since the order of the 3D wing model are very large and the eigenvalue analysis is computationally expensive. In order to reduce the cost of the eigenvalue analysis, typically first 15 free vibration modes of the structure are used to decrease the degrees of freedom in Eq. (3.29) (Stanford and Beran 2011). The eigenvector is approximated as:

$$\boldsymbol{\eta} = \boldsymbol{\Phi} \cdot \boldsymbol{\varphi} \tag{3.30}$$

where $\boldsymbol{\Phi}$ is a modal matrix which contains the modes in each column, and $\boldsymbol{\varphi}$ is a vector of modal amplitudes in generalised coordinates. Inserting the approximation of Eq. (3.30) into the Eq. (3.29), and pre-multiplying each term by $\boldsymbol{\Phi}^{\mathrm{T}}$ provides:

$$\left[\left(\frac{U_\infty}{c}\right)^2 \boldsymbol{\Phi}^T \cdot \boldsymbol{M} \cdot \boldsymbol{\Phi} \cdot p^2 + \frac{q_\infty}{k} \cdot \boldsymbol{\Phi}^T \cdot \boldsymbol{A_i} \cdot \boldsymbol{\Phi} \cdot p + (\boldsymbol{\Phi}^T \cdot \boldsymbol{K} \cdot \boldsymbol{\Phi} - q_\infty \cdot \boldsymbol{\Phi}^T \cdot \boldsymbol{A_r} \cdot \boldsymbol{\Phi})\right] \cdot \boldsymbol{\varphi} = 0 \tag{3.31}$$

$$\left[\left(\frac{U_\infty}{c}\right)^2 \widetilde{\boldsymbol{M}} \cdot p^2 + \frac{q_\infty}{k} \cdot \widetilde{\boldsymbol{A_i}} \cdot p + \left(\widetilde{\boldsymbol{K}} - q_\infty \cdot \widetilde{\boldsymbol{A_r}}\right)\right] \cdot \boldsymbol{\varphi} = 0 \tag{3.32}$$

where $\widetilde{\boldsymbol{M}}$ is the reduced mass matrix, $\widetilde{\boldsymbol{K}}$ is the reduced stiffness matrix, $\widetilde{\boldsymbol{A_i}}$ and $\widetilde{\boldsymbol{A_r}}$ are the reduced unsteady aerodynamic matrices. Alternatively, the *p-k* equation is a quadratic eigenvalue problem. Therefore, Eq. (3.32) can also be written in first order form as:

$$\left\{p \cdot \begin{bmatrix} \boldsymbol{I} & 0 \\ 0 & \left(\frac{U_\infty}{c}\right)^2 \widetilde{\boldsymbol{M}} \end{bmatrix} - \begin{bmatrix} 0 & \boldsymbol{I} \\ q_\infty \cdot \widetilde{\boldsymbol{A_r}} - \widetilde{\boldsymbol{K}} & \frac{q_\infty}{k} \cdot \widetilde{\boldsymbol{A_i}} \end{bmatrix}\right\} \cdot \begin{Bmatrix} \boldsymbol{\varphi} \\ p \cdot \boldsymbol{\varphi} \end{Bmatrix} = 0 \tag{3.33}$$

For a matched point solution to Eq. (3.33) the input reduced frequency k must equal the imaginary part of the resulting eigenvalue: $\mathrm{Im}(p) = k$, and the air speed and Mach number must correspond for a given altitude. The real part of the matched point eigenvalue indicates the stability of the system at the current q_∞ value. If $\mathrm{Re}(p) < 0$, the system is stable, whereas if $\mathrm{Re}(p) > 0$ in any mode, then the system is unstable and flutter will occur in that particular mode. If all the modes are stable, then the complete system of the wing is stable. The flutter point in this study is defined as the matched point solution with the lowest dynamic pressure that produces a single eigenvalue with $\mathrm{Re}(p) = 0$, with all other modes stable (Dunning et al, 2015). The matched flutter design point can be written as two equations that are dependent on the solution of Eq. (3.33):

$$\begin{Bmatrix} \mathrm{Re}(p) \\ \mathrm{Im}(p) - k \end{Bmatrix} = 0 \tag{3.34}$$

The flutter point can usually be found by incrementally increasing the dynamic pressure, or air speed, until both conditions in Eq. (3.34) are satisfied by a solution to Eq. (3.33). The aerodynamic matrices are non-linearly dependent on the Mach number, M_∞ and reduced frequency, k, and they are contained within the DLM numerical procedure. Both of these non-linear effects should be taken into consideration when searching for a matched point solution to Eq. (3.33). Large computation and storage are required to model the entire non-linear space via interpolation by considering sufficient number of aerodynamic matrices at various M_∞ and k values. In order to reduce the burden of the computation, the Mach number is fixed during the analysis. If the maximum flight speed is relatively small compared to the speed of sound at the design altitude, then compressibility effects can be ignored, and the Mach number can be fixed at zero. If this is not possible, another alternative is to fix both flight speed and Mach number in Eq. (3.33), while defining the flutter point in terms of dynamic pressure or air density. This approach is equivalent to defining the matched flutter point as the minimum altitude at a given speed where: $\mathrm{Re}(p) = 0$. As the speed of sound is generally not constant with the altitude, therefore this approach is also an approximation, but

the dependence is relatively weak. In this study, the flight speed and Mach number are fixed, and the flutter point is defined as the minimum dynamic pressure that produces an eigenvalue solution to Eq. (3.33) that satisfies Eq. (3.34).

The flutter point is first approximately found by gradually increasing the dynamic pressure from zero until the real part of an eigenvalue, p becomes positive. The exact matched flutter point is then found using Newton's method to satisfy the residual in Eq. (3.34). Matched points in the k space at a specific dynamic pressure value are found using a non-iterative frequency sweeping technique. For a range of dynamic pressure, the reduced frequency, k is incrementally increased and the corresponding eigenvalue p is computed until a crossing with the unit-slope line in the (Im(p) – k) space is noted. The matched point solution for k = Im(p) is then obtained by linear interpolation. The frequency sweeping method is more efficient than frequency iteration method because it requires fewer solves of Eq. (3.33). In addition, the frequency iteration has a limitation of converging to a matched point. Using the frequency sweep method, the eigenvalues can be tracked as the reduced frequency, k increased (for a given dynamic pressure, q) and also as q increased. The detail of the mode tracking in flutter analysis will be further explained in Chapter 5.

Chapter 4

Derivation of the Analytical Sensitivities

In this chapter the analytical sensitivities that are used to solve the final optimisation problem are presented. The following section introduces the aeroelastic optimisation formulation, which includes the objective function as well as the constraint functions. The sensitivity derivation of these functions are then derived in the later sections.

4.1 Optimisation Formulation

The objective function studied in this work is to minimise the wing mass of the internal wing box structure. Two structural constraints, i.e. compliance and flutter constraints are added into the optimisation problem formulation in order to prevent the structural failure. The third constraint is the static equilibrium equation for the coupled aero-structural system, which is implicitly satisfied when solving for the displacement, $\boldsymbol{u}$. Hence, the optimisation problem can be stated as:

$$\text{Minimise: } M_w = \rho \cdot Vol \tag{4.1}$$

$$\text{Subject to: } C(\boldsymbol{u},\boldsymbol{\Omega}) \leq \boldsymbol{f_t}(\boldsymbol{u},\boldsymbol{\Omega})^T \cdot \boldsymbol{u} \tag{4.2}$$

$$q^* \geq q_{lim} \tag{4.3}$$

$$\boldsymbol{K}(\boldsymbol{\Omega}) \cdot \boldsymbol{u} = \boldsymbol{f_t}(\boldsymbol{u},\boldsymbol{\Omega}) = \boldsymbol{f_a}(\boldsymbol{u},\boldsymbol{\Omega}) + N \cdot \boldsymbol{f_g}(\boldsymbol{\Omega}) \tag{4.4}$$

where M_w is the wing box structural mass, ρ is the material density, *Vol* is the volume of the wing box, C is the compliance, $\boldsymbol{u}$ is the deformation vector of the wing, $\boldsymbol{f_t}$ is the total load vector, q^* is the flutter dynamic pressure, q_{lim} is the limit on the flutter dynamic pressure.

Before performing level set topology optimisation, the sensitivity analysis of the objective function (wing mass) and constraints (compliance and flutter) are required. This chapter will detail the derivations of the sensitivity analysis. In order to aid the understanding of the derivations of compliance and flutter sensitivities, they are first derived in discrete form and then transfer to continuous form in an equivalent manner.

4.2 Mass sensitivity

The structural mass of the wing box, M_w can be written in the continuous form as:

$$M_w = \rho \int_{\Omega} H(\Omega) d\Omega \tag{4.5}$$

where ρ is the material density and $H(\Omega)$ is the Heaviside step function:

$$H(\Omega) = \begin{cases} 1, & \Omega \geq 0 \\ 0, & \Omega < 0 \end{cases} \tag{4.6}$$

To perform optimisation using the level-set method, the velocity function in Eq. (2.3) is often defined from shape derivatives. Shape derivatives take the form of a boundary integral of a shape sensitivity function multiplied by the velocity function:

$$\frac{\partial f(\Omega)}{\partial \Omega} = \int_{\Gamma} \left(s_f \cdot V_n\right) d\Gamma \tag{4.7}$$

where f is a function dependent on the structural domain and s_f is the shape sensitivity function for f, which is continuous along the boundary. Hence, the derivative of the mass of the wing box with respect to the design variable can be written as:

$$\frac{\partial M_w}{\partial \Omega} = \rho \int_{\Gamma} \left(s_{M_w} \cdot V_n\right) d\Gamma \tag{4.8}$$

where the shape sensitivity function for s_{Mw} is:

$$s_{M_w} = \int_{\Omega} \frac{\partial H(\Omega)}{\partial \Omega} d\Omega = 1, \quad \text{for } \Omega \geq 0 \tag{4.9}$$

4.3 Static Aeroelastic Sensitivity

Before deriving the compliance sensitivity analysis, we start with a general function, g($\boldsymbol{x}$, $\boldsymbol{u}$), that is dependent on some vector of structural design variables, $\boldsymbol{x}$, and the solution to the static aeroelastic equation, $\boldsymbol{u}$, which is also a function of design variables. The adjoint method is used to obtain the derivative of the general function with respect to the design variables. First, the residual of the static equation is added to the function:

$$G(\boldsymbol{x}, \boldsymbol{u},) = g(\boldsymbol{x}, \boldsymbol{u}) - \boldsymbol{w}^T \left[\boldsymbol{K} \cdot \boldsymbol{u} - \boldsymbol{f_a}(\boldsymbol{u}, \alpha) - N \cdot \boldsymbol{f_g}(\boldsymbol{\Omega})\right] \tag{4.10}$$

where $\boldsymbol{w}$ is the adjoint vector. Taking the total derivative of Eq. (4.10) with respect to the design variables, $\boldsymbol{x}$ gives:

$$\begin{aligned} \frac{\partial G}{\partial \boldsymbol{x}} = \frac{\partial g}{\partial \boldsymbol{x}} + \frac{\partial g}{\partial \boldsymbol{u}} \cdot \frac{\partial \boldsymbol{u}}{\partial \boldsymbol{x}} - \boldsymbol{w}^T \left[\frac{\partial \boldsymbol{K}}{\partial \boldsymbol{x}} \cdot \boldsymbol{u} + \boldsymbol{K} \cdot \frac{\partial \boldsymbol{u}}{\partial \boldsymbol{x}} - \frac{\partial \boldsymbol{f_a}}{\partial \boldsymbol{u}} \cdot \frac{\partial \boldsymbol{u}}{\partial \boldsymbol{x}} \right. \\ \left. - \frac{\partial \boldsymbol{f_a}}{\partial \alpha} \cdot \left(\frac{\partial \alpha}{\partial \boldsymbol{x}} + \frac{\partial \alpha}{\partial \boldsymbol{u}} \cdot \frac{\partial \boldsymbol{u}}{\partial \boldsymbol{x}}\right) - N \cdot \frac{\partial \boldsymbol{f_g}}{\partial \boldsymbol{x}}\right] \end{aligned} \tag{4.11}$$

Re-arranging Eq. (4.11) results in:

$$\frac{\partial G}{\partial \boldsymbol{x}} = \frac{\partial g}{\partial \boldsymbol{x}} - \boldsymbol{w}^T \cdot \frac{\partial \boldsymbol{K}}{\partial \boldsymbol{x}} \cdot \boldsymbol{u} - \boldsymbol{w}^T \left[N \cdot \frac{\partial \boldsymbol{f_g}}{\partial \boldsymbol{x}} + \frac{\partial \boldsymbol{f_a}}{\partial \alpha} \cdot \frac{\partial \alpha}{\partial \boldsymbol{x}}\right] \tag{4.12}$$

$$+\left[\frac{\partial g}{\partial \boldsymbol{u}}-\boldsymbol{w}^{T}\cdot\left(\boldsymbol{K}-\frac{\partial \boldsymbol{f_a}}{\partial \boldsymbol{u}}-\frac{\partial \boldsymbol{f_a}}{\partial \alpha}\cdot\frac{\partial \alpha}{\partial \boldsymbol{u}}\right)\right]\cdot\frac{\partial \boldsymbol{u}}{\partial \boldsymbol{x}}$$

The aeroelastic adjoint equation for $\boldsymbol{w}$ is then:

$$\boldsymbol{K^{T}}\cdot\boldsymbol{w}=\left[\frac{\partial \boldsymbol{f_a}}{\partial \boldsymbol{u}}+\frac{\partial \boldsymbol{f_a}}{\partial \alpha}\cdot\frac{\partial \alpha}{\partial \boldsymbol{u}}\right]^{T}\cdot\boldsymbol{w}+\frac{\partial g}{\partial \boldsymbol{u}}=\boldsymbol{Q_d}\cdot\boldsymbol{w}+\frac{\partial g}{\partial \boldsymbol{u}} \tag{4.13}$$

The term $\boldsymbol{Q_d}$ in Eq. (4.13) is the dual aerodynamic stiffness matrix, which is constant and includes the effect of the angle of attack for trim. The term $\frac{\partial \boldsymbol{f_a}}{\partial \alpha}$ is equal to the aerodynamic force generated per angle of attack, termed $\boldsymbol{f}_{\alpha}$. The term $\frac{\partial \alpha}{\partial \boldsymbol{u}}$ can be obtained by differentiating α in Eq. (3.14) with respect to u:

$$\frac{\partial \alpha(\Omega,u)}{\partial u}=\frac{b_i}{L_\alpha} \tag{4.14}$$

where only the aircraft weight, W is dependent on $\boldsymbol{x}$. Thus the gradient for a general function that depends on the static aeroelastic equation is:

$$\frac{\partial G}{\partial \boldsymbol{x}}=\frac{\partial g}{\partial \boldsymbol{x}}-\boldsymbol{w}^{T}\cdot\frac{\partial \boldsymbol{K}}{\partial \boldsymbol{x}}\cdot\boldsymbol{u}+N\cdot\boldsymbol{w}^{T}\left[\frac{\partial \boldsymbol{f_g}}{\partial \boldsymbol{x}}+\boldsymbol{f}_{\alpha}\cdot\frac{\partial W}{\partial \boldsymbol{x}}\right] \tag{4.15}$$

where $\boldsymbol{w}$ is the solution to the adjoint equation Eq. (4.13).

4.4 Compliance Sensitivity Analysis

4.4.1 Compliance Sensitivity Analysis in Discrete Form

The compliance function, $C(\boldsymbol{u}, \boldsymbol{x})$ is the multiplication of the total load vector and the displacement vector:

$$C(\boldsymbol{u},\boldsymbol{x})=\boldsymbol{f_t}(\boldsymbol{u},\boldsymbol{x})^{T}\cdot\boldsymbol{u}=\left(\boldsymbol{f_a}(\boldsymbol{u},\alpha)+\ N\cdot\boldsymbol{f_g}(\boldsymbol{x})\right)^{T}\cdot\boldsymbol{u} \tag{4.16}$$

where N is a load factor (N = 1 for steady level flight). The total load vector, $\boldsymbol{f_t}$ is comprised of aerodynamic load vector, $\boldsymbol{f_a}$ and gravity load vector, $\boldsymbol{f_g}$. Differentiating Eq. (4.16) by $\boldsymbol{u}$ and $\boldsymbol{x}$ gives:

$$\frac{\partial C}{\partial \boldsymbol{u}} = \left(\boldsymbol{f_a} - N \cdot \boldsymbol{f_g}\right) + \left(\frac{\partial \boldsymbol{f_a}}{\partial \boldsymbol{u}} + \frac{\partial \boldsymbol{f_a}}{\partial \alpha} \cdot \frac{\partial \alpha}{\partial \boldsymbol{u}}\right) \cdot \boldsymbol{u} = \left(\boldsymbol{f_a} - N \cdot \boldsymbol{f_g}\right) + \boldsymbol{Q_d} \cdot \boldsymbol{u} \tag{4.17}$$

$$\frac{\partial C}{\partial \boldsymbol{x}} = \left(\frac{\partial \boldsymbol{f_a}}{\partial \boldsymbol{x}} + N \cdot \frac{\partial \boldsymbol{f_g}}{\partial \boldsymbol{x}}\right)^{\boldsymbol{T}} \cdot \boldsymbol{u} \tag{4.18}$$

Substituting Eq. Into results in the adjoint equation for aeroelastic compliance:

$$\boldsymbol{K^T} \cdot \boldsymbol{w} = \boldsymbol{Q_d} \cdot (\boldsymbol{u} + \boldsymbol{w}) + \boldsymbol{f_a}(\boldsymbol{u}, \alpha) + N \cdot \boldsymbol{f_g}(\boldsymbol{x}) \tag{4.19}$$

where $\boldsymbol{u}$ and α are obtained from the solution to the static aeroelastic equation Eq. (3.7).

Substituting Eq. (4.18) into Eq. (4.15), the gradient for aeroelastic compliance is:

$$\frac{\partial C}{\partial \boldsymbol{x}} = -\boldsymbol{w}^T \cdot \frac{\partial \boldsymbol{K}}{\partial \boldsymbol{x}} \cdot \boldsymbol{u} + N \cdot \left[\left(\frac{\partial \boldsymbol{f_g}}{\partial \boldsymbol{x}}\right)^T \cdot (\boldsymbol{u} + \boldsymbol{w}) + (\boldsymbol{w}^T \cdot \boldsymbol{f_\alpha}) \cdot \frac{\partial W}{\partial \boldsymbol{x}}\right] \tag{4.20}$$

where the adjoint is found from the solution to Eq. (4.19).

4.4.2 Compliance Sensitivity Analysis in Continuous Form

The derivative of the compliance function in Eq. (4.22) was formulated in discrete form, which are discretisation of the continuous equation. For level-set based optimisation, the design variable is the position of the boundary, characterised by the domain of the structure Ω. The shape derivative of a general function, g takes the form of a continuous boundary integral:

$$\frac{\partial g}{\partial \Omega} = \int_{\Gamma} \left(s_g \cdot V_n\right) d\Gamma \tag{4.21}$$

where s_f is the shape sensitivity of g, and V_n is the velocity function.

The aerodynamic load vector, $\boldsymbol{f_a}$ in Eq. (4.16) can be expanded by combining with Eq. (3.7) which was previously explained in Chapter 3. Thus, the compliance function in discrete form becomes:

$$C(\boldsymbol{u},\boldsymbol{x}) = \left(\boldsymbol{f_c} - \alpha(\boldsymbol{u},\boldsymbol{x}) \cdot \boldsymbol{f_\alpha} + \boldsymbol{Q} + N \cdot \boldsymbol{f_g}(\boldsymbol{x})\right)^T \cdot \boldsymbol{u} \tag{4.22}$$

In order to obtain the shape derivative for the compliance in Eq. (4.22), the continuous forms obtained from Allaire et al. (2004) are used. The compliance function can be written in a continuous form as:

$$\begin{aligned} C(u,\Omega) = \int_{\Gamma_N} (f_c \cdot u) d\Gamma_N - \alpha(u,\Omega) \int_{\Gamma_N} (f_\alpha \cdot u) d\Gamma_N \\ + \int_{\Gamma_N} \left(Q_{i,j} u_i \cdot u_j\right) d\Gamma_N + N \int_\Omega \left(f_g \cdot u\right) d\Omega \end{aligned} \tag{4.23}$$

where Γ_N is the part of the boundary where the aerodynamic loads are applied and $Q_{i,j}$ is the continuous tensor form of the aerodynamic stiffness. Note that the aerodynamic loads (f_c, f_α and $Q_{i,j} \cdot u_i$) are applied on the boundary of the upper wing surface Γ_N, whereas the body load due to the wing weight, f_g is applied to the entire structural domain, Ω. The continuous form of the aero-structural equilibrium equation is:

$$\begin{aligned} \int_\Omega \left(E\varepsilon(u) \cdot \varepsilon(v)\right) d\Omega = \int_{\Gamma_N} (f_c \cdot v) d\Gamma_N - \alpha(v,\Omega) \int_{\Gamma_N} (f_\alpha \cdot v) d\Gamma_N \\ + \int_{\Gamma_N} \left(Q_{i,j} v_i \cdot u_j\right) d\Gamma_N + N \int_\Omega \left(f_g \cdot v\right) d\Omega \\ + \int_{\Gamma_D} (v \cdot E\varepsilon(u) n + u \cdot E\varepsilon(v) n)\, d\Gamma_D \end{aligned} \tag{4.24}$$

where E is the material property tensor, $\varepsilon(u)$ is the strain tensor, v is the virtual displacement, n is a unit vector normal to the boundary and Γ_D is the part of the boundary where displacement boundary conditions are applied.

The adjont method is used to obtain the shape derivative of Eq. (4.23). A Lagrangian function is formed by adding the aero-structural equilibrium equation, Eq. (4.24) to the compliance equation, Eq. (4.23), using a Lagrange multiplier, λ:

$$\begin{aligned}\mathcal{L}(\Omega, v, \lambda) = C(v, \Omega) - \int_{\Omega} \left(E\varepsilon(v) \cdot \varepsilon(\lambda)\right) d\Omega + \int_{\Gamma_N} (\lambda \cdot f_c) d\Gamma_N \\ - \alpha(v, \Omega) \int_{\Gamma_N} (\lambda \cdot f_\alpha) d\Gamma_N + \int_{\Gamma_N} \left(Q_{i,j}\lambda_i \cdot v_j\right) d\Gamma_N \\ + N \int_{\Omega} \left(\lambda \cdot f_g\right) d\Omega \\ + \int_{\Gamma_D} (\lambda \cdot E\varepsilon(v)n + v \cdot E\varepsilon(\lambda)n)\, d\Gamma_D\end{aligned} \tag{4.25}$$

The adjoint equation is derived by differentiating Eq. (4.25) with respect to v in the direction θ and defining (u, w) as a stationary point, where w is an adjoint state vector. The adjoint equation now becomes:

$$\begin{aligned}\langle \frac{\partial \mathcal{L}}{\partial v}(\Omega, u, w), \theta \rangle = 0 \\ = - \int_{\Omega} \left(E\varepsilon(\theta) \cdot \varepsilon(w)\right) d\Omega + \int_{\Gamma_N} (f_c \cdot \theta) d\Gamma_N \\ - \frac{\partial \alpha(\Omega, u)}{\partial u} \int_{\Gamma_N} (f_\alpha \cdot (u + w) \cdot \theta) d\Gamma_N \\ + \int_{\Gamma_N} \left(Q_{i,j}(u_i \cdot w_i) \cdot \theta\right) d\Gamma_N + N \int_{\Omega} \left(f_g \cdot \theta\right) d\Omega \\ + \int_{\Gamma_D} (w \cdot E\varepsilon(\theta)n + \theta \cdot E\varepsilon(w)n)\, d\Gamma_D\end{aligned} \tag{4.26}$$

where the chevron brackets denote a vector inner product. In Eq. (4.26), the change in angle of attack with respect to the change in deformed wing shape is required. Differentiating Eq. (3.14) with respect to u gives:

$$\frac{\partial \alpha(\Omega, u)}{\partial u} = \frac{b_i}{L_\alpha} \tag{4.27}$$

By setting the displacement vector, u and adjoint state vector w equal to zero on the displacement boundary conditions, Γ_D and substituting Eq. (4.27) into Eq. (4.26), the adjoint equation can be written as:

$$\int_{\Omega} \left(E\varepsilon(\theta) \cdot \varepsilon(w)\right) d\Omega = \int_{\Gamma_N} (f_c \cdot \theta) d\Gamma_N - \frac{b_i}{L_\alpha} \int_{\Gamma_N} (f_\alpha \cdot (u + w) \cdot \theta) d\Gamma_N + \int_{\Gamma_N} \left(Q_{i,j}(u_i \cdot w_i) \cdot \theta\right) d\Gamma_N + N \int_{\Omega} \left(f_g \cdot \theta\right) d\Omega \tag{4.28}$$

The shape derivative can now be computed by differentiating the Lagrangian equation, Eq. (4.25) with respect to the shape in the direction, θ, at the stationary point (u, w). During optimisation,

$$\frac{\partial \mathcal{L}}{\partial \Omega}(\Omega, u, w)(\theta) = \int_{\Gamma_0} \theta \cdot n \left(N \cdot f_g \cdot (u + w) - E\varepsilon(u) \cdot \varepsilon(w)\right) d\Gamma_0 - \frac{\partial \alpha}{\partial \Omega}(\Omega, u) \int_{\Gamma_N} f_\alpha (u + w) d\Gamma_N \tag{4.29}$$

The term $\frac{\partial \alpha}{\partial \Omega}(\Omega, u)$ in Eq. (4.29) is the derivative of the angle of attack, α which can be obtained by differentiating Eq. (3.14) with respect to the shape. At the stationary point, this term is simply the shape derivative of the structural weight multiplied by the load factor over L_α:

$$\frac{\partial \alpha(\Omega, u)}{\partial \Omega} = -\frac{N}{L_\alpha} \int_{\Gamma_0} \theta \cdot n (\rho \cdot g_r) d\Gamma_0 \tag{4.30}$$

where ρ is the material density and g_r is the acceleration due to gravity. Setting $\theta \cdot n$ equal to the normal velocity in the first term on the right hand side of Eq. (2.3), where a positive velocity is an inward movement, such that $\theta \cdot n = -V_n$, the final compliance derivative on free boundary becomes:

$$\frac{\partial C}{\partial \Omega}(\Omega, u, w) = \int_{\Gamma_0} V_n\big(E\varepsilon(u)\cdot\varepsilon(w) - N\cdot f_g\cdot(u+w) - A \cdot \rho g\big)\, d\Gamma_0 \tag{4.31}$$

$$A_c = \frac{N}{L_\alpha}\int_{\Gamma_N}\big(f_\alpha\cdot(u+w)\big)d\Gamma_N$$

where A_c is a constant factor over the entire boundary. This factor relates the change in compliance due to a change in the angle of attack, resulting from a change in the wing box weight.

4.5 Flutter Sensitivity

This section details the gradient computation for the matched flutter point and the formulation of a continuous flutter constraint function and its gradient in both discrete and continuous forms.

4.5.1 Gradient of the Matched Flutter Point

The *p-k* eigenvalue equation with reduced order mass and stiffness matrices Eq. (3.32) is placed in first order form:

$$f(k) = \left\{p\cdot\left[\begin{Bmatrix}\boldsymbol{I} & 0\\ 0 & \left(\frac{U_\infty}{c}\right)^2\widetilde{\boldsymbol{M}}\end{Bmatrix} - \begin{bmatrix} q\cdot\widetilde{\boldsymbol{A_r}}(k) - \widetilde{\boldsymbol{K}} & \frac{q}{k}\cdot\widetilde{\boldsymbol{A_i}}(k)\end{bmatrix}\right\}\cdot\begin{Bmatrix}\boldsymbol{\varphi}\\ p\cdot\boldsymbol{\varphi}\end{Bmatrix} = 0 \tag{4.32}$$

For clarity in the sequel, the eigenvectors of Eq. (3.33) are split into two parts. These two parts are known as the left eigenvector, $\{\boldsymbol{L}_1, \boldsymbol{L}_2\}^{\mathrm{T}}$, and the right eigenvector, $\{\boldsymbol{R}_1, \boldsymbol{R}_2\}^{\mathrm{T}}$, which are defined by:

$$\begin{Bmatrix}\boldsymbol{L}_1\\ \boldsymbol{L}_2\end{Bmatrix}^H\cdot\left\{p\cdot\left[\begin{Bmatrix}\boldsymbol{I} & 0\\ 0 & \left(\frac{U_\infty}{c}\right)^2\widetilde{\boldsymbol{M}}\end{Bmatrix} - \begin{bmatrix} q\cdot\widetilde{\boldsymbol{A_r}}(k) - \widetilde{\boldsymbol{K}} & \frac{q}{k}\cdot\widetilde{\boldsymbol{A_i}}(k)\end{bmatrix}\right\} = 0 \tag{4.33}$$

$$\left\{p\cdot\left[\begin{Bmatrix}\boldsymbol{I} & 0\\ 0 & \left(\frac{U_\infty}{c}\right)^2\widetilde{\boldsymbol{M}}\end{Bmatrix} - \begin{bmatrix} q\cdot\widetilde{\boldsymbol{A_r}}(k) - \widetilde{\boldsymbol{K}} & \frac{q}{k}\cdot\widetilde{\boldsymbol{A_i}}(k)\end{bmatrix}\right\}\cdot\begin{Bmatrix}\boldsymbol{R}_1\\ \boldsymbol{R}_2\end{Bmatrix} = 0 \tag{4.34}$$

where the superscript H in Eq. (4.33) denotes the complex conjugate transpose. By using chain rule differentiation method, the derivatives of the eigenvalue can be obtained by taking the total derivatives of the eigenvalue problem in Eq. (3.33) with respect to the dynamic pressure, q:

$$\frac{\partial f(k,q)}{\partial q} = \frac{\partial f(k,q)}{\partial q} + \frac{\partial f(k,q)}{\partial p} \cdot \frac{\partial p}{\partial q} = 0 \tag{4.35}$$

Re-arranging Eq. (4.35) gives:

$$\frac{\partial p}{\partial q} = -\frac{\partial f(k,q)}{\partial q} \Big/ \frac{\partial f(k,q)}{\partial p} \tag{4.36}$$

Similarly, the eigenvalue derivative with respect to the reduced frequency, k can also be derived as:

$$\frac{\partial p}{\partial k} = -\frac{\partial f(k,q)}{\partial k} \Big/ \frac{\partial f(k,q)}{\partial p} \tag{4.37}$$

The derivatives of the real and imaginary parts of the eigenvalue with respect to q and k are simply the real and imaginary parts of Eq. (4.36) and Eq. (4.37), respectively. Pre-multiplying Eq. (3.33) by the conjugate transpose of the left eigenvector and differentiating by p, q and k gives:

$$\begin{aligned} \frac{\partial f}{\partial p} &= \begin{Bmatrix} \boldsymbol{L}_1 \\ \boldsymbol{L}_2 \end{Bmatrix}^H \cdot \begin{bmatrix} \boldsymbol{I} & 0 \\ 0 & \left(\frac{U_\infty}{c}\right)^2 \widetilde{\boldsymbol{M}} \end{bmatrix} \cdot \begin{Bmatrix} \boldsymbol{R}_1 \\ \boldsymbol{R}_2 \end{Bmatrix} \\ &= \boldsymbol{L}_1^H \cdot \boldsymbol{R}_1 + \left(\frac{\mathrm{U}_\infty}{c}\right)^2 \cdot \boldsymbol{L}_2^H \cdot \widetilde{\boldsymbol{M}} \cdot \boldsymbol{R}_2 \end{aligned} \tag{4.38}$$

$$\begin{aligned} \frac{\partial f}{\partial q} &= \begin{Bmatrix} \boldsymbol{L}_1 \\ \boldsymbol{L}_2 \end{Bmatrix}^H \cdot \begin{bmatrix} 0 & 0 \\ -\widetilde{\boldsymbol{A}_r}(k) & -\frac{\widetilde{\boldsymbol{A}_i}(k)}{k} \end{bmatrix} \begin{Bmatrix} \boldsymbol{R}_1 \\ \boldsymbol{R}_2 \end{Bmatrix} \\ &= -\boldsymbol{L}_2^H \cdot \widetilde{\boldsymbol{A}_r}(k) \cdot \boldsymbol{R}_1 - \boldsymbol{L}_2^H \cdot \frac{\widetilde{\boldsymbol{A}_i}(k)}{k} \cdot \boldsymbol{R}_2 \end{aligned} \tag{4.39}$$

$$\begin{aligned} \frac{\partial f}{\partial k} &= \begin{Bmatrix} \boldsymbol{L}_1 \\ \boldsymbol{L}_2 \end{Bmatrix}^H \cdot \begin{bmatrix} 0 & 0 \\ -q \cdot \frac{\partial \widetilde{\boldsymbol{A}_r}(k)}{\partial k} & -\frac{q}{k}\left(\frac{\widetilde{\boldsymbol{A}_i}(k)}{k} - \frac{\partial \widetilde{\boldsymbol{A}_i}(k)}{\partial k}\right) \end{bmatrix} \cdot \begin{Bmatrix} \boldsymbol{R}_1 \\ \boldsymbol{R}_2 \end{Bmatrix} \\ &= -q \cdot \boldsymbol{L}_2^H \cdot \frac{\partial \widetilde{\boldsymbol{A}_r}(k)}{\partial k} \cdot \boldsymbol{R}_1 + \left(\frac{q}{k}\right) \cdot \boldsymbol{L}_2^H \cdot \left(\frac{\widetilde{\boldsymbol{A}_i}(k)}{k} - \frac{\partial \widetilde{\boldsymbol{A}_i}(k)}{\partial k}\right) \cdot \boldsymbol{R}_2 \end{aligned} \tag{4.40}$$

The partial derivatives of the reduced aerodynamic matrices with respect to k are found using the finite difference method. This approach is tractable because the reduced matrices are pre-computed for a range of k values and it is sufficient to assume that entries in the matrices are piecewise linear between the chosen k values. Therefore, the gradients of the aerodynamic matrices with respect to k are piecewise constant.

Now the derivative of the dynamic pressure at the matched flutter point with respect to the structural design variables can be computed. First the values of q and k at the matched flutter point are denoted, q^* and k^*, respectively. The matched point residual from Eq. (3.34) is now written as:

$$F(\boldsymbol{Y},\boldsymbol{x}) = \begin{Bmatrix} \mathrm{Re}(p) \\ \mathrm{Im}(p) - k \end{Bmatrix} \quad , \; \boldsymbol{Y} = \{q^*, k^*\} \tag{4.41}$$

Differentiating the total derivative of the flutter residual, Eq. (4.41) with respect to $\boldsymbol{x}$ gives:

$$\frac{dF(\boldsymbol{Y},\boldsymbol{x})}{d\boldsymbol{x}} = \frac{\partial F}{\partial \boldsymbol{x}} + \frac{\partial F}{\partial \boldsymbol{Y}} \cdot \frac{\partial \boldsymbol{Y}}{\partial \boldsymbol{x}} = 0 \tag{4.42}$$

Re-arranging Eq. (4.42) and expanding $\boldsymbol{Y}$ gives:

$$\begin{Bmatrix} \partial q^*/\partial \boldsymbol{x} \\ \partial k^*/\partial \boldsymbol{x} \end{Bmatrix} = -\left(\frac{\partial F}{\partial \boldsymbol{Y}}\right)^{-1} \cdot \frac{\partial F}{\partial \boldsymbol{x}} = -\begin{bmatrix} \dfrac{\partial \mathrm{Re}(p)}{\partial q^*} & \dfrac{\partial \mathrm{Re}(p)}{\partial k^*} \\ \dfrac{\partial \mathrm{Im}(p)}{\partial q^*} & \dfrac{\partial \mathrm{Im}(p)}{\partial k^*} \end{bmatrix}^{-1} \begin{Bmatrix} \mathrm{Re}\left(\dfrac{\partial p}{\partial \boldsymbol{x}}\right) \\ \mathrm{Im}\left(\dfrac{\partial p}{\partial \boldsymbol{x}}\right) \end{Bmatrix} \tag{4.43}$$

The Jacobian matrix in Eq. (4.43) is obtained at the end of the Newton's iterations used to find the matched flutter point. The eigenvalue derivative with respect to the design variable $\boldsymbol{x}$ required for Eq. (4.43) is:

$$\frac{\partial p}{\partial \boldsymbol{x}} = -\frac{\partial f}{\partial \boldsymbol{x}} \Big/ \frac{\partial f}{\partial p} \tag{4.44}$$

where the term $\frac{\partial f}{\partial p}$ was previously computed by Eq. (4.38). Pre-multiplying Eq. (3.33) by the conjugate transpose of the left eigenvector and differentiating by $\boldsymbol{x}$ gives:

$$\begin{aligned}\frac{\partial f}{\partial \boldsymbol{x}} &= \begin{Bmatrix}\boldsymbol{L}_1\\ \boldsymbol{L}_2\end{Bmatrix}^H \cdot \begin{bmatrix}0 & 0\\ \frac{\partial \widetilde{\boldsymbol{K}}}{\partial \boldsymbol{x}} & p \cdot \left(\frac{U_\infty}{c}\right)^2 \cdot \frac{\partial \widetilde{\boldsymbol{M}}}{\partial \boldsymbol{x}}\end{bmatrix} \cdot \begin{Bmatrix}\boldsymbol{R}_1\\ \boldsymbol{R}_2\end{Bmatrix} \\ &= \boldsymbol{L}_2^H \cdot \frac{\partial \widetilde{\boldsymbol{K}}}{\partial \boldsymbol{x}} \cdot \boldsymbol{R}_1 + p \cdot \left(\frac{U_\infty}{c}\right)^2 \cdot \boldsymbol{L}_2^H \cdot \frac{\partial \widetilde{\boldsymbol{M}}}{\partial \boldsymbol{x}} \cdot \boldsymbol{R}_2\end{aligned} \tag{4.45}$$

Recalling Eq. (3.31), the derivatives of the reduced order mass and stiffness matrices required for Eq. (4.45) are:

$$\begin{aligned}\frac{\partial \widetilde{\boldsymbol{M}}}{\partial \boldsymbol{x}} &= \boldsymbol{\Phi}^T \frac{\partial \boldsymbol{M}}{\partial \boldsymbol{x}} \boldsymbol{\Phi} + 2\left(\frac{\partial \boldsymbol{\Phi}}{\partial \boldsymbol{x}}\right)^T \cdot \boldsymbol{M} \cdot \boldsymbol{\Phi} \\ \frac{\partial \widetilde{\boldsymbol{K}}}{\partial \boldsymbol{x}} &= \boldsymbol{\Phi}^T \frac{\partial \boldsymbol{K}}{\partial \boldsymbol{x}} \boldsymbol{\Phi} + 2\left(\frac{\partial \boldsymbol{\Phi}}{\partial \boldsymbol{x}}\right)^T \cdot \boldsymbol{K} \cdot \boldsymbol{\Phi}\end{aligned} \tag{4.46}$$

The derivatives of the structural eigenvectors, $\frac{\partial \boldsymbol{\Phi}}{\partial \boldsymbol{x}}$ in Eq. (4.46) are expensive to compute. If we assumed that the modes do not change when the design is updated, then the eigenvector derivatives are zero. This is called the "fixed-mode" approach. Thus, the derivatives of the mass and stiffness matrices are now:

$$\begin{aligned}\frac{\partial \widetilde{\boldsymbol{M}}}{\partial \boldsymbol{x}} &\approx \boldsymbol{\Phi}^T \frac{\partial \boldsymbol{M}}{\partial \boldsymbol{x}} \boldsymbol{\Phi} \\ \frac{\partial \widetilde{\boldsymbol{K}}}{\partial \boldsymbol{x}} &\approx \boldsymbol{\Phi}^T \frac{\partial \boldsymbol{K}}{\partial \boldsymbol{x}} \boldsymbol{\Phi}\end{aligned} \tag{4.47}$$

4.5.2 Continuous Flutter Constraint and Gradient in Discrete Form

During the optimisation process, the flutter point can be discontinuous with respect to a change in the design variables, primarily due to a switching of the critical mode. This causes difficulties when the flutter point is considered as a constraint. Haftka (1975) proposed an idea of a continuous flutter constraint. The continuous flutter constraint is defined as:

$$G_f(q) < 0 \quad , \; q \in \{q_{\min}, q_{\max}\} \tag{4.48}$$

$$G_f(q) = \begin{cases} 1 - (q/q_{\lim}) & \text{if } q > q_{\lim} \;\&\; \mathrm{Re}(p) > 0 \\ \mathrm{Re}(p)/p_{\mathrm{ref}} & \text{if } q < q_{\lim} \;\&\; \mathrm{Re}(p) < 0 \\ (\mathrm{Re}(p)/p_{\mathrm{ref}}) \cdot \left(1 - (q/q_{\lim})\right)^2 & \text{if } q < q_{\lim} \;\&\; \mathrm{Re}(p) > 0 \\ 1 - (q/q_{\lim}) + (\mathrm{Re}(p)/p_{\mathrm{ref}}) & \text{if } q > q_{\lim} \;\&\; \mathrm{Re}(p) < 0 \end{cases} \tag{4.49}$$

The third row in Eq. (4.49) is an addition to Haftka (1975)'s original formulation to make the constraint function continuous over all possible q and Re(p) values. During optimisation we are interested in points where $G_f(q)$ is a local maximum:

$$\frac{\partial G_f(q)_{\max}}{\partial q} = 0, \qquad \frac{\partial^2 G_f(q)_{\max}}{\partial q^2} < 0 \tag{4.50}$$

At each optimisation iteration, there may be some local maximum points in the dynamic pressure range of interest. This is not a problem because each point can be treated as a separate constraint. In practice, local maximum points are found using a dynamic pressure sweeping method. Starting from $q_{\min}$ all matched points (Im(p) = k) and associated modes are obtained. The dynamic pressure is then increased and the new matched point eigenvalues, p, are correlated to the eigenvalues at the previous q value. During this process, the values of $G_f(q)$ are also tracked for each mode of interest. When the slope of a tracked $G_f(q)$ function goes through a sign change from positive to negative, then an approximate local maximum has been found. However, there is no condition that Re(p) = 0 and the q value at the approximate local maximum is assumed to be accurate. Therefore, the matched point for the local maximum can be located by using Newton's iterations to minimise the following residual equation:

$$F(k, \boldsymbol{x}) = \mathrm{Im}(p) - k \tag{4.51}$$

where the necessary first order gradient, $\frac{\partial p}{\partial k}$ as shown in Eq. (4.37) can be obtained from Eq. (4.38) and Eq. (4.40).

The derivative of the continuous flutter function with respect to $\boldsymbol{x}$ is:

$$\frac{dG_f}{d\boldsymbol{x}} = \frac{\partial G_f}{\partial \boldsymbol{x}} + \frac{\partial G_f}{\partial q}\,\frac{\partial q}{\partial \boldsymbol{x}} \tag{4.52}$$

If Eq. (4.52) is evaluated at a local maximum of $G_f(q)$, then from Eq. (4.50) the partial derivative of $G_f(q)$ with respect to q is zero. Thus, the derivative of $G_f(q)$ with respect to $\boldsymbol{x}$ is simplified to:

$$\frac{dG_{f\,\max}}{d\boldsymbol{x}} = \frac{\partial G_{f\,\max}}{\partial \boldsymbol{x}} \tag{4.53}$$

Differentiating Eq. (4.49) with respect to the design variable $\boldsymbol{x}$ gives:

$$\frac{dG_f(q)}{d\boldsymbol{x}} = \begin{cases} 0 & \text{if } q > q_{\text{lim}} \;\&\; \text{Re}(p) > 0 \\ (1/p_{\text{ref}})(d\text{Re}(p)/d\boldsymbol{x}) & \text{if } q < q_{\text{lim}} \;\&\; \text{Re}(p) < 0 \\ (1/p_{\text{ref}})\left(\dfrac{d\text{Re}(p)}{d\boldsymbol{x}}\right)\cdot\left(1-\left(\dfrac{q}{q_{\text{lim}}}\right)\right)^2 & \text{if } q < q_{\text{lim}} \;\&\; \text{Re}(p) > 0 \\ (1/p_{\text{ref}})(d\text{Re}(p)/d\boldsymbol{x}) & \text{if } q > q_{\text{lim}} \;\&\; \text{Re}(p) < 0 \end{cases} \tag{4.54}$$

where the derivative of Re(p) with respect to $\boldsymbol{x}$, $\frac{d\text{Re}(p)}{d\boldsymbol{x}}$ has an implicit dependence on q and the reduced frequency k through the matched point condition in Eq. (4.51). Thus, the derivative is:

$$\frac{d\text{Re}(p)}{d\boldsymbol{x}} = \frac{\partial \text{Re}(p)}{\partial \boldsymbol{x}} + \frac{\partial \text{Re}(p)}{\partial q}\,\frac{\partial q}{\partial \boldsymbol{x}} + \frac{\partial \text{Re}(p)}{\partial k}\,\frac{\partial k}{\partial \boldsymbol{x}} \tag{4.55}$$

For a small change in the design variables, the continuous constraint function about the current q value, which is at a local maximum can be approximated (Haftka 1975). If that is the case, the partial derivative term $\frac{\partial q}{\partial \boldsymbol{x}}$ in Eq. (4.55) can be set to zero. The explicit derivatives of Re(p) with respect to $\boldsymbol{x}$ and k are computed from Eq. (4.44) and Eq. (4.37), respectively. The derivative of k with respect to $\boldsymbol{x}$ can be obtained by taking the total derivative of the matched point condition Eq. (4.51):

$$\frac{dF}{d\boldsymbol{x}} = \left(\frac{\partial \text{Im}(p)}{\partial \boldsymbol{x}} - \frac{\partial k}{\partial \boldsymbol{x}}\right) + \left(\frac{\partial \text{Im}(p)}{\partial k} - 1\right)\cdot\frac{\partial k}{\partial \boldsymbol{x}} = 0 \tag{4.56}$$

where the term $\frac{\partial \mathrm{Im}(p)}{\partial k}$ can be found at the end of the Newton's iterations to find the matched point. Re-arranging Eq. (4.56) for the derivative *k* with respect of $\boldsymbol{x}$ gives:

$$\frac{\partial k}{\partial \boldsymbol{x}} = \frac{\partial \mathrm{Im}(p)}{\partial \boldsymbol{x}} \Big/ \left(2 - \frac{\partial \mathrm{Im}(p)}{\partial k}\right) \tag{4.57}$$

The derivative of Re(*p*) with respect to the design variables $\boldsymbol{x}$ required for the derivative of the continuous flutter constraint in Eq. (4.54) is then:

$$\frac{d\mathrm{Re}(p)}{d\boldsymbol{x}} = \frac{\partial \mathrm{Re}(p)}{\partial \boldsymbol{x}} + \frac{\partial \mathrm{Re}(p)}{\partial k} \cdot \frac{\partial \mathrm{Im}(p)}{\partial \boldsymbol{x}} \Big/ \left(2 - \frac{\partial \mathrm{Im}(p)}{\partial k}\right) \tag{4.58}$$

4.5.3 Flutter Sensitivity Analysis in Continuous Form

The approached detailed in Section 4.5.1 and Section 4.5.2 are extended to compute the continuous shape derivative of the flutter point. The start point is to take the reduced order structural mass and stiffness matrices from Eq. (3.31) and multiply out each entry:

$$\begin{aligned} \widetilde{\boldsymbol{M}} = \boldsymbol{\Phi}^T \boldsymbol{M} \boldsymbol{\Phi} &= \begin{bmatrix} m_{1,1} & m_{1,2} & \cdots & m_{1,n} \\ m_{2,1} & m_{2,2} & \cdots & m_{2,n} \\ & & \ddots & \\ & & & m_{n,n} \end{bmatrix} \\ \widetilde{\boldsymbol{K}} = \boldsymbol{\Phi}^T \boldsymbol{K} \boldsymbol{\Phi} &= \begin{bmatrix} s_{1,1} & s_{1,2} & \cdots & s_{1,n} \\ s_{2,1} & s_{2,2} & \cdots & s_{2,n} \\ & & \ddots & \\ & & & s_{n,n} \end{bmatrix} \end{aligned} \tag{4.59}$$

where *n* is the number of structural eigenvectors used to form the reduced order model and the matrix entries are defined as:

$$m_{i,j} = \boldsymbol{\phi}_i^T \boldsymbol{M} \boldsymbol{\phi}_j \quad , \quad c_{i,j} = \boldsymbol{\phi}_i^T \boldsymbol{K} \boldsymbol{\phi}_j \tag{4.60}$$

The definitions in Eq. (4.60) can be written in the continuous weak formulation:

$$m_{i,j} \approx \int_{\Omega} \rho \cdot \phi_i \cdot \phi_j \, d\Omega \quad , \quad c_{i,j} \approx \int_{\Omega} E\varepsilon(\phi_i) \cdot \varepsilon(\phi_j) \, d\Omega \tag{4.61}$$

The derivatives of a reduced order matrix with respect to the structural design variables can be obtained by computing the shape derivative of each matrix entry, as defined by the weak continuous form Eq. (4.61):

$$\begin{aligned} \frac{\partial m_{i,j}}{\partial \Omega} &= -\int_{\Gamma} \rho \cdot \phi_i \cdot \phi_j \cdot V_n \, d\Gamma + \int_{\Omega} \rho \cdot \frac{\partial \phi_i}{\partial \Omega} \cdot \phi_j \, d\Omega \\ &\quad + \int_{\Omega} \rho \cdot \phi_i \cdot \frac{\partial \phi_j}{\partial \Omega} d\Omega \\ \frac{\partial c_{i,j}}{\partial \Omega} &= -\int_{\Gamma} E\varepsilon(\phi_i) \cdot \varepsilon(\phi_j) \cdot V_n \, d\Gamma + \int_{\Omega} E\varepsilon\left(\frac{\partial \phi_i}{\partial \Omega}\right) \cdot \varepsilon(\phi_j) \, d\Omega \\ &\quad + \int_{\Omega} E\varepsilon(\phi_i) \cdot \varepsilon\left(\frac{\partial \phi_j}{\partial \Omega}\right) d\Omega \end{aligned} \tag{4.62}$$

where $\frac{\partial \phi_i}{\partial \Omega}$ and $\frac{\partial \phi_j}{\partial \Omega}$ terms are the shape derivatives of the eigenvectors. If the 'fixed-mode' approach is used, then those two terms are zero. The shape derivatives are simplified to:

$$\begin{aligned} \frac{\partial m_{i,j}}{\partial \Omega} &= -\int_{\Gamma} \rho \cdot \phi_i \cdot \phi_j \cdot V_n \, d\Gamma \\ \frac{\partial c_{i,j}}{\partial \Omega} &= -\int_{\Gamma} E\varepsilon(\phi_i) \cdot \varepsilon(\phi_j) \cdot V_n \, d\Gamma \end{aligned} \tag{4.63}$$

Using the result of Eq. (4.63) the shape derivatives of the reduced order stiffness and mass matrices are obtained. Substituting these derivatives into Eq. (4.45), where the design variable is the shape, Ω, gives:

$$\frac{\partial f}{\partial \Omega} = \boldsymbol{L}_2^H \cdot \frac{\partial \widetilde{\boldsymbol{K}}}{\partial \Omega} \cdot \boldsymbol{R}_1 + p \cdot \left(\frac{U_\infty}{b}\right)^2 \cdot \boldsymbol{L}_2^H \cdot \frac{\partial \widetilde{\boldsymbol{M}}}{\partial \Omega} \cdot \boldsymbol{R}_2 \tag{4.64}$$

$$\frac{\partial f}{\partial \Omega} = -\int_{\Gamma} \left[\sum_{i=1}^{n} \sum_{j=1}^{n} \left(\boldsymbol{L}_{2,i}^{H} \cdot \boldsymbol{R}_{1,j} \cdot E\varepsilon(\phi_i) \cdot \varepsilon(\phi_j) + p \cdot \left(\frac{V}{b}\right)^2 \right.\right.$$

$$\left.\left. \cdot \boldsymbol{L}_{2,i}^{H} \cdot \boldsymbol{R}_{2,j} \cdot \rho \cdot \phi_i \cdot \phi_j \right) \cdot V_n \right] d\Gamma$$

where *n* is the number of modes used in the reduced order, or number of columns in Φ. Substituting Eq. (4.38) and Eq. (4.64) into Eq. (4.44), where the design variable is now the shape, Ω, gives:

$$\frac{\partial p}{\partial \Omega} = -\frac{\partial f}{\partial \Omega} \Big/ \frac{\partial f}{\partial p} = \int_{\Gamma} \varphi_p \cdot V_n \, d\Gamma \tag{4.65}$$

where:

$$\varphi_p = \frac{\sum_{i=1}^{n} \sum_{j=1}^{n} \left(\boldsymbol{L}_{2,i}^{H} \cdot \boldsymbol{R}_{1,j} \cdot E\varepsilon(\phi_i) \cdot \varepsilon(\phi_j) + p \cdot \left(\frac{V}{b}\right)^2 \cdot \boldsymbol{L}_{2,i}^{H} \cdot \boldsymbol{R}_{2,j} \cdot \rho \cdot \phi_i \cdot \phi_j \right)}{\boldsymbol{L}_1^H \cdot \boldsymbol{R}_1 + \left(\frac{V}{b}\right)^2 \cdot \boldsymbol{L}_2^H \cdot \widetilde{\boldsymbol{M}} \cdot \boldsymbol{R}_2} \tag{4.66}$$

Finally, Eq. (4.43) with Eq. (4.65) are used to obtain the shape derivative of the flutter dynamic pressure:

$$\frac{\partial q^*}{\partial \Omega} = -\int_{\Gamma} \left[\left(J_{1,1} \cdot \mathrm{Re}(\varphi_p) + J_{1,2} \cdot \mathrm{Im}(\varphi_p) \right) \cdot V_n \right] d\Gamma \tag{4.67}$$

where the $J_{i,j}$ terms are entries in the inverse Jacobian matrix found from the end of the Newton's iterations used to locate the matched flutter point, Eq. (4.43). Using the results above, the derivative in Eq. (4.58) can be extended to compute the shape derivative of the continuous flutter constraint:

$$\frac{\partial \mathrm{Re}(p)}{\partial \Omega} = -\int_{\Gamma} \left[\left(\mathrm{Re}(\varphi_p) + J \cdot \mathrm{Im}(\varphi_p) \right) \cdot V_n \right] d\Gamma \tag{4.68}$$

where *J* is:

$$J = \frac{\partial \mathrm{Re}(p)}{\partial k} \Big/ \left(2 - \frac{\partial \mathrm{Im}(p)}{\partial k} \right) \tag{4.69}$$

where the derivatives of p with respect to k are obtained at the end of the Newton's iterations to find the matched point in Eq. (4.51). Eq. (4.68) is used with Eq. (4.54) to complete the shape derivatives of the continuous flutter constraint.

4.6 Least Squares Interpolation Method

The mass sensitivity $\frac{\partial M_w}{\partial \Omega}$ in Eq. (4.8), the compliance sensitivity $\frac{\partial C}{\partial \Omega}$ in Eq. (4.31) and the flutter sensitivity $\frac{\partial q^*}{\partial \Omega}$ in Eq. (4.67) are calculated on the Gauss points in every finite elements. During level set optimisation, the structural boundary is allowed to moved, and thus the sensitivities at the boundary nodes are required for computing the velocity function. A least squares interpolation method is used, where the sensitivities at Gauss integration points are weighed by distance and element volume ratio (Dunning et al. 2011). Only the Gauss points within a user set radius of the boundary points are considered to increase computational efficiency, as shown in Figure 4.1. Detailed research studies by Dunning et al. (2011) have shown that this approach creates a continuous boundary sensitivity field that is comparable to one produced by a fitted mesh.

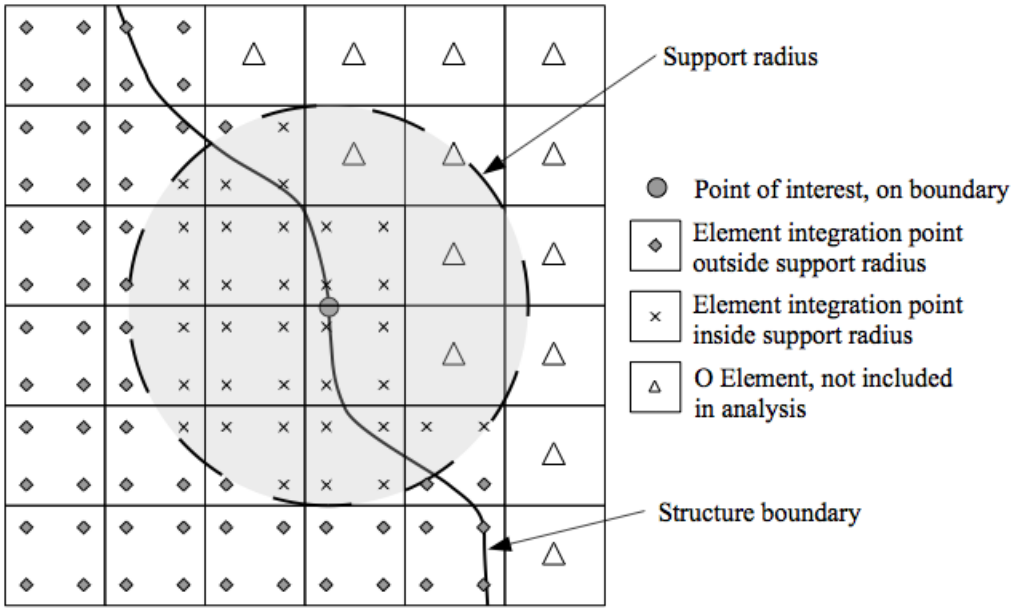

Figure 4.1: Gauss point sampling scheme for the least squares interpolation method (Dunning 2011).

4.7 Conclusions

This chapter presents the analytical sensitivities that are required for the level set based optimisation method. In the aeroelastic optimisation studies, the objective functions and constraints can be wing mass, compliance or flutter dynamic pressure. The analytical sensitivities for wing mass, compliance and flutter dynamic pressure are derived in both discrete form and continuous form. The derivation of the flutter sensitivities in continuous form is the key contribution in the chapter. A least squares interpolation method is used to ensure the sensitivities are interpolated accurately to other boundary nodes in the fixed grid mesh. The wing mass, compliance and flutter sensitivities will be used for the aeroelastic optimisation studies in the following chapters.

Chapter 5

Investigation of the Mode Switching Problem

5.1 Introduction

Mode tracking is particularly important in flutter analysis using the *p-k* method. The modes need to be tracked as the reduced frequency, *k* value is changed or the dynamic pressure is increased. Additional modes also need to be tracked from one speed increment to the next. The *p-k* method was formulated in Chapter 3.5 where a non-self-adjoint eigenvalue problem was solved and there will be a number of complex eigenvalues equal to the order of the system (Eldred et al. 1995). Care must be taken to select the correct eigenvalue that corresponds to the current mode of interest. Various mode tracking techniques have been developed in the past to track the modes during the maximisation of eigenfrequency or flutter problem. This chapter will discuss the existing techniques and present an improved mode tracking method. This improved mode tracking method is implemented in a flutter maximisation problem using a level set based topology optimisation method.

5.2 Existing Mode Tracking Techniques

5.2.1 Modal Assurance Criterion (MAC) Method

One of the first original developments of mode tracking techniques, known as the modal assurance criterion (MAC) was introduced by Allemang and Brown (1982). The MAC is a method of evaluating the consistency between different estimates of a modal vector, and so of matching the corresponding modes between different analyses. This method is widely used in the verification of finite element models (FEM) by comparing predicted and experimental frequency response matrices or mode shapes. The definition of MAC is (Ewins 1986):

$$\mathrm{MAC}(\boldsymbol{\Phi}_o, \boldsymbol{\Phi}_t) = \frac{(\boldsymbol{\Phi}_o^T \boldsymbol{\Phi}_t)^2}{(\boldsymbol{\Phi}_o^T \boldsymbol{\Phi}_o)(\boldsymbol{\Phi}_t^T \boldsymbol{\Phi}_t)} \tag{5.1}$$

where $\boldsymbol{\Phi}_t$ and $\boldsymbol{\Phi}_o$ are targeted and objective mode shapes respectively. The MAC represents the degree of correlation between the two vectors, where a higher value indicates a greater degree of similarity. In the application of MAC to the mode tracking topology optimization (Kim and Kim 2000; Tsai and Cheng 2012), a reference mode shape is defined as a desired mode shape at the initial configuration. To track the desired mode shape during iterations, the MAC value of each of the extracted modes of the updated structure is examined with respect to the reference mode. Tsai and Cheng (2012) added MAC as additional constraints in the structural topology optimisation to maximise the natural frequencies, where the eigenvectors are real. The first order derivative of the MAC must be carefully derived. Ting et al. (1994) and Desforges et al. (1996) implemented the MAC method in flutter analysis and verified the approach with experimental flutter test data. However, there was a big discrepancy in flutter analysis between the MAC method and the experimental flutter test data when the reduced order models were used due to the noise effect. The accuracy of the flutter analysis also depends on the number or position of the response transducers at the experiment model for reasonable estimates of the mode shapes to be obtained.

5.2.2 Eigenvector Orthogonality Correlation Method

A more robust method to track modes is to compare the orthogonality between the current modes and the converged modes from the previous speed or reduced frequency value. This can be achieved using the eigenvector orthogonality correlation method proposed by van Zyl (1993) and the MAC method by Desforges et al. (1996) that was mentioned in previous section. The only difference compared to van Zyl (1993) is that the eigenvector matrix is transformed into the LR decomposition. Based on the flutter equation in Eq. (3.33), the complex eigenvectors can be split into left eigenvector $\boldsymbol{L}$ and right eigenvector $\boldsymbol{R}$. Eq. (3.33) is equivalent to:

$$\{\boldsymbol{L}\}^H \cdot \left\{ p \cdot \begin{bmatrix} \boldsymbol{I} & 0 \\ 0 & \left(\frac{U_\infty}{c}\right)^2 \widetilde{\boldsymbol{M}} \end{bmatrix} - \begin{bmatrix} 0 & \boldsymbol{I} \\ q \cdot \widetilde{\boldsymbol{A_r}}(k) - \widetilde{\boldsymbol{K}} & \frac{q}{k} \cdot \widetilde{\boldsymbol{A_\iota}}(k) \end{bmatrix} \right\} = 0 \tag{5.2}$$

$$\left\{ p \cdot \begin{bmatrix} \boldsymbol{I} & 0 \\ 0 & \left(\frac{U_\infty}{c}\right)^2 \widetilde{\boldsymbol{M}} \end{bmatrix} - \begin{bmatrix} 0 & \boldsymbol{I} \\ q \cdot \widetilde{\boldsymbol{A_r}}(k) - \widetilde{\boldsymbol{K}} & \frac{q}{k} \cdot \widetilde{\boldsymbol{A_\iota}}(k) \end{bmatrix} \right\} \cdot \{\boldsymbol{R}\} = 0 \tag{5.3}$$

where the eigenvectors $\boldsymbol{L}$ and $\boldsymbol{R}$ terms are dependent on the number of modes n and are written in a transpose form:

$$\begin{aligned} \boldsymbol{L} &= \{L_1, L_2, \dots, L_n\}^T \\ \boldsymbol{R} &= \{R_1, R_2, \dots, R_n\}^T \end{aligned} \tag{5.4}$$

The scalar products of the converged eigenvectors of the previous dynamic pressure and the current eigenvectors are calculated using Eq. (5.5) and formed in a single matrix. Each row i and column j of the matrix correspond to the scalar product of an old eigenvector and a current eigenvector, respectively. The scalar product between two complex eigenvectors must be defined such that it is independent of scaling and phase (van Zyl, 1993). A definition which satisfies these conditions is:

$$\boldsymbol{L} \cdot \boldsymbol{R} = \frac{\sqrt{S_1^2 + S_2^2}}{\sqrt{S_3 S_4}} \tag{5.5}$$

where:

$$S_1 = \sum_{i=1}^{n} Re(L_i)Re(R_i) + Im(L_j)Im(R_j) \tag{5.6}$$

$$S_2 = \sum_{i=1}^{n} Re(L_i)Im(R_j) - Im(L_i)Re(R_j) \tag{5.7}$$

$$S_3 = \sum_{i=1}^{n} \|L_i\|^2 \tag{5.8}$$

$$S_4 = \sum_{i=1}^{n} \|R_j\|^2 \tag{5.9}$$

Once the correlation matrix has been computed, the matrix is then searched for the largest element. The corresponding old and current eigenvectors that are taken belong to the same mode at different speeds or reduced frequencies. The corresponding row and column are removed (or zeroed) and the process is repeated until there are no more modes to match.

5.3 Improved Eigenvector Orthogonality Method

The orthogonality correlation method is not guaranteed to successfully track the modes. One way in which they can fail is due to the selection of the largest remaining value in the correlation matrix. For example, if the correlation matrix is computed as:

$$\begin{bmatrix} 0.9 & 0.1 & 0.2 \\ 0.3 & 0.8 & 0.7 \\ 0.5 & 0.7 & 0.1 \end{bmatrix} \tag{5.10}$$

The following correlations would be made (highlighted in red):

$$\begin{bmatrix} 0.9 & 0.1 & 0.2 \\ 0.3 & 0.8 & 0.7 \\ 0.5 & 0.7 & 0.1 \end{bmatrix} \tag{5.11}$$

It can be observed from Eq. (5.11) that the correlations for modes 1 and 2 seem to be good, with correlation values of 0.9 and 0.8, respectively. However, for mode 3, the selected correlation coefficient is poor, at 0.1. This may signify an error in the mode tracking.

The premise of the improved version of the eigenvector orthogonality correlation method is to choose correlation coefficients from the matrix in such a way to maximise their total. This can be efficiently achieved using the well-known Hungarian algorithm (Kuhn 2009). This algorithm works out the minimum cost or maximum matching by performing row and column operations on the matrix. When the algorithm is applied to the example in Eq. (5.10), the following solution is found for the maximum matching:

$$\begin{bmatrix} 0.9 & 0.1 & 0.2 \\ 0.3 & 0.8 & 0.7 \\ 0.5 & 0.7 & 0.1 \end{bmatrix} \tag{5.12}$$

In order to guarantee successful mode correlation to detect a failure, the step size can be reduced and the step is repeated (Eldred et al. 1995). However, the number of failures detected with the improved correlation method will be fewer than the original method. Therefore, larger steps can be used leading to faster convergence and faster identification of the flutter speed. The improved eigenvector orthogonality method is implemented to maximise the flutter dynamic pressure in next section.

5.4 Maximisation of Flutter Dynamic Pressure

5.4.1 Optimisation Problem Definition

The optimisation problem is to maximise the flutter dynamic pressure subject to a mass constraint:

$$\begin{aligned} &\text{Maximise:} \quad q^* \\ &\text{Subject to:} \quad M_w \leq M_w^* \end{aligned} \tag{5.13}$$

where q^* is the matched flutter dynamic pressure and M_w^* is the mass upper limit. q^* is obtained by satisfying both conditions in Eq. (5.14) below as previously discussed in Chapter 3.5:

$$\begin{Bmatrix} \mathrm{Re}(p) \\ \mathrm{Im}(p) - k \end{Bmatrix} = 0 \tag{5.14}$$

The derivative of q^* and M_w^* are derived and obtained from Eq. (4.67) and Eq. (4.8), respectively. The final derivations are presented as:

$$\frac{\partial q^*}{\partial \Omega} = -\int_{\Gamma} \left[\left(J_{1,1} \cdot \mathrm{Re}(\varphi_p) + J_{1,2} \cdot \mathrm{Im}(\varphi_p) \right) \cdot V_n \right] d\Gamma \tag{5.15}$$

$$\frac{\partial M_w}{\partial \Omega} = \rho \int_{\Gamma} \left(s_{M_w} \cdot V_n \right) d\Gamma \tag{5.16}$$

where the shape sensitivity function for s_{Mw} is:

$$s_{M_w} = \int_{\Omega} \frac{\partial H(\Omega)}{\partial \Omega} d\Omega = 1, \quad \text{for } \Omega \geq 0 \tag{5.17}$$

The Sequential Linear Programming (SLP) level set method is used to solve the aeroelastic optimisation problem for high aspect ratio wing outlined in Eq. (5.13). The wing is modelled by a 25 ×40 aerodynamic mesh (Figure 5.1) and the wing box is modelled by 12400 solid elements (Figure 5.2). The computation of the aerodynamic load that is applied to the finite element model is previously discussed in Chapter 3. All the solid elements are treated as design variables and the stiffness of each element is allowed to vary (Dunning and Kim 2013). Frst 15 modes is considered in the flutter analysis to compute the reduced order models.

The *p-k* method described in Chapter 3.5 is validated against results obtained from MSC NASTRAN.

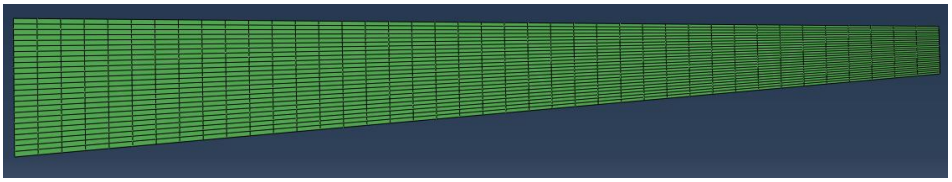

Figure 5.1: Aerodynamic (Doublet Lattice) 2D model

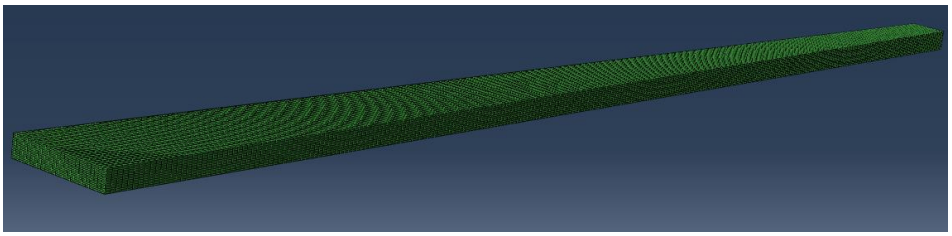

Figure 5.2: Structural Finite Element 3D model

The internal structure of the wing box is represented by the level set implicit function in Eq. (2.1), discretised on a 3D grid fitted to the wing box shape. This part of the structure is optimised by iteratively solving Eq. (2.3), where the velocity function V_n is obtained from shape sensitivities in Eq. (4.67) and Eq. (4.8). A modified fast marching method is used to extend the velocity function values to all grid points (Dunning et al. 2014). This approach has the benefit of maintaining the signed distance function, which is important for the stability of the level set method.

The aircraft flight conditions, wing external geometry, wing box geometry and wing material properties are described from Table 5.1 to Table 5.4 below:

Flight Conditions

Cruise Mach number, M_∞	0.85
Cruise altitude (*ft*)	28000
Cruise weight (*kg*)	2.5×10^5
Air density at cruise (kg/m^3)	0.5

Table 5.1: Aircraft flight conditions.

Wing External Geometry

Aspect ratio	18
Reference wing area (m^2)	222.22
Taper ratio	0.35
Root chord (m)	5.21
Tip chord (m)	1.82
Mean aerodynamic chord (m)	3.79
Half wing span, (m)	31.62
¼-chord sweep angle	0 º
Thickness-to-chord ratio (m)	0.15

Table 5.2: Properties of the wing external geometry.

Wing Box Geometry

Wing box root chord (m)	3.12
Wing box tip chord (m)	1.09

Table 5.3: Properties of the wing box geometry.

Wing Material Properties

Young's modulus (Pa)	70×10^9
Poisson's ratio	0.30

Table 5.4: Wing material properties.

5.4.2 Optimisation Results

The flutter dynamic pressure maximisation problem in Eq. (5.13), is solved with a wing mass constraint of 2495kg, which corresponds to a 50% mass fraction for the internal structure. The initial wing structure is shown in Figure 5.3 and the solution is shown in Figure 5.4. From the figures, the red regions represent solid material, whereas the grey regions represent void. The solution has several interesting features. Firstly, the outboard leading edge section is reinforced with materials, whereas the trailing edge region is mostly void, with the exception of the wing tip trailing edge. This moves the centre of gravity forward, which is a mass balancing effect known to be favourable for flutter (Dunning et al. 2015; Stanford and Beran 2011). Secondly, at the mid-span section, the material is formed diagonally between the leading edge and trailing edge. This strut-like structure adds bending stiffness to the structure.

The critical dynamic pressure of the initial wing structure has 16830Pa. From the convergence histories shown in Figure 5.5, divergence at mode 1 occurs for the initial wing. Divergence becomes critical during the first 27^{th} iterations (plotted in yellow line in Figure 5.5). A problem arises at 28^{th} iteration because there is no critical points found during the flutter analysis, as shown in Figure 5.6. The divergence derivative with respect to the dynamic pressure at the point where the damping ratio is -0.0037 (flutter dynamic pressure = 44844Pa) is computed to prevent discontinuity in the optimisation. This situation carries on until 30^{th} iteration, where the solution finds a critical flutter at mode 8. The flutter dynamic pressure is calculated to be 146406Pa.

Mode switching problem is found between the 30^{th} and 31^{st} iterations, where the critical mode is switched from mode 8 (flutter) to mode 1 (divergence). The improved eigenvector orthogonality correlation method is able to track the modes successfully in this case. The damping curve in Figure 5.8 shows that mode 1 is a hump mode. In the later iterations, the optimiser is trying to maximise the flutter dynamic pressure by suppressing the “hump”. This can be observed from 34^{th}

iteration that the critical flutter at mode 1 becomes dominant. The flutter dynamic pressure is increased and finally converged at 95th iteration (179290Pa).

Initial wing:
Mass = 4459kg
q^* = 16830Pa

Figure 5.3: Initial wing structure (top view). (Red regions represent solid material, whereas the grey regions represent void).

15th iteration:
Mass = 4308kg
q^* = 21818Pa

30th iteration:
Mass = 3840kg
q^* = 146342Pa

60th iteration:
Mass = 2621kg
q^* = 170983Pa

Final wing (95th iteration):
Mass = 2462kg
q^* =179290Pa

Figure 5.4: Flutter dynamic pressure maximisation solutions for M_w^* = 50% × $M_{w,initial}$. Wing mass (M_w) and critical divergence/flutter dynamic pressure (q^*) at the iterations shown. (Red regions represent solid material, whereas the grey regions represent void).

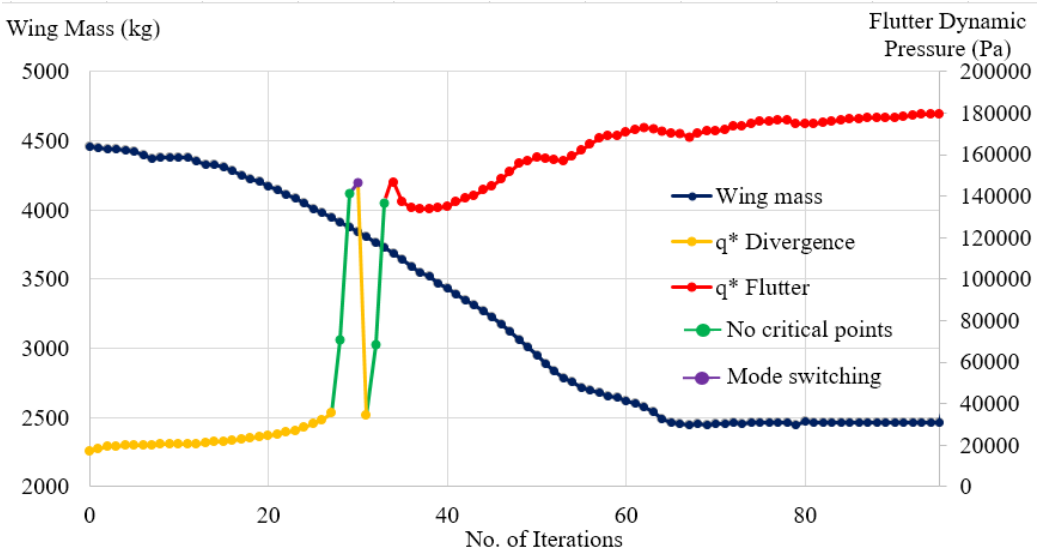

Figure 5.5: Convergence histories for flutter dynamic pressure maximisation problem subject to wing mass constraint.

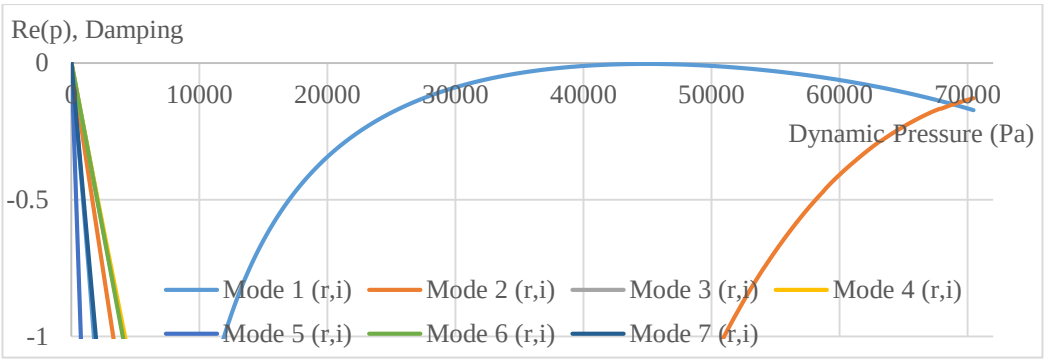

Figure 5.6: Damping curve at the 28th iteration.

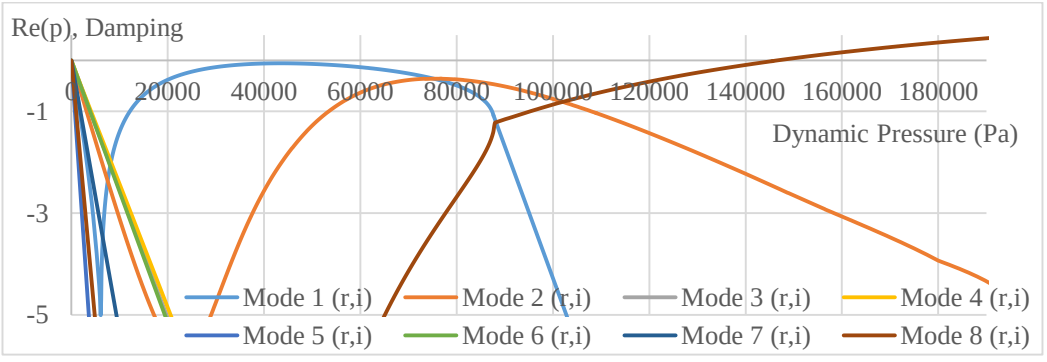

Figure 5.7: Damping curve at the 30th iteration.

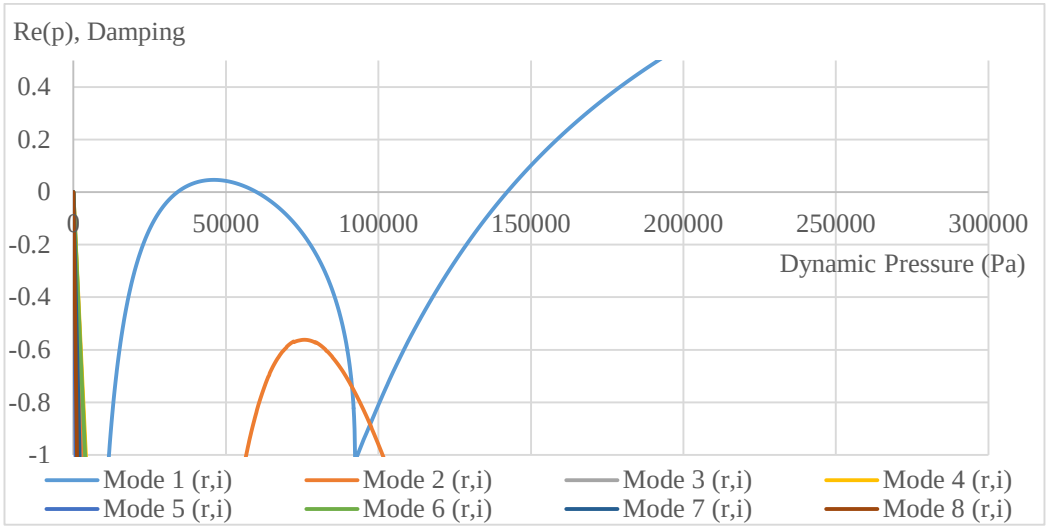

Figure 5.8: Damping curve at the 31st iteration.

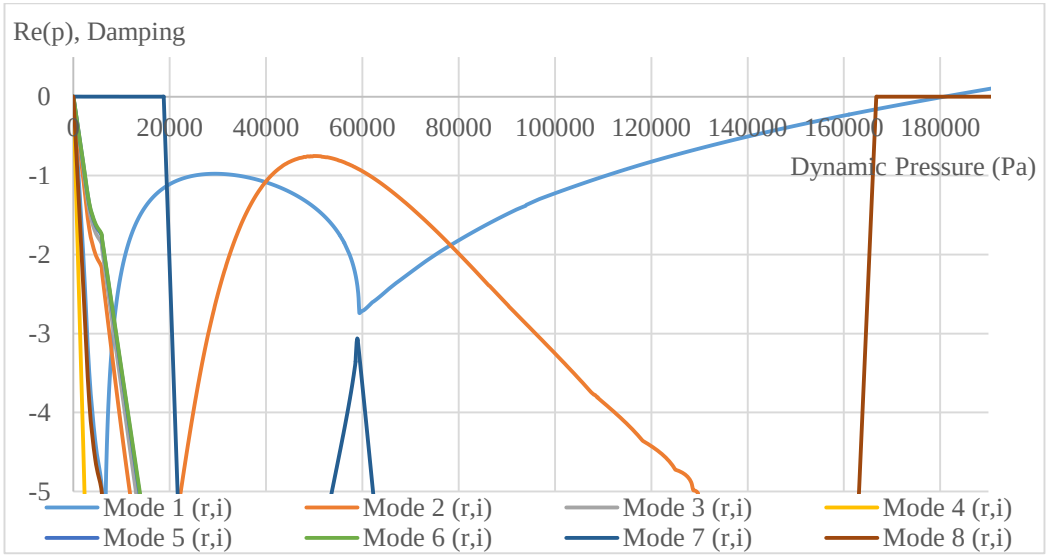

Figure 5.9: Damping curve at final solution (95st iteration).

The mass fraction, which is the constraint in Eq. (5.13) are varied between 0.4 and 0.7. A series of flutter maximisation is carried for the corresponding mass fraction constraints. Figure 5.10 shows the optimal wing topologies for various mass fractions. As the mass fraction increases, the trailing edge has more materials as the optimiser tries to find the feasible solution by satisfying the larger mass fraction constraint. The flutter dynamic pressures for the optimal wing topologies are plotted in Figure 5.11. The flutter dynamic pressure increases from mass fraction 0.4 to 0.6. However, the flutter dynamic pressure is reduced by 11.9% between mass fraction 0.6 and 0.7. When mass fraction is 0.7, the mass at the trailing edge causes the wing to flutter early, as compared to the other mass fraction designs. Therefore, mass distribution and its location are important in flutter optimisation.

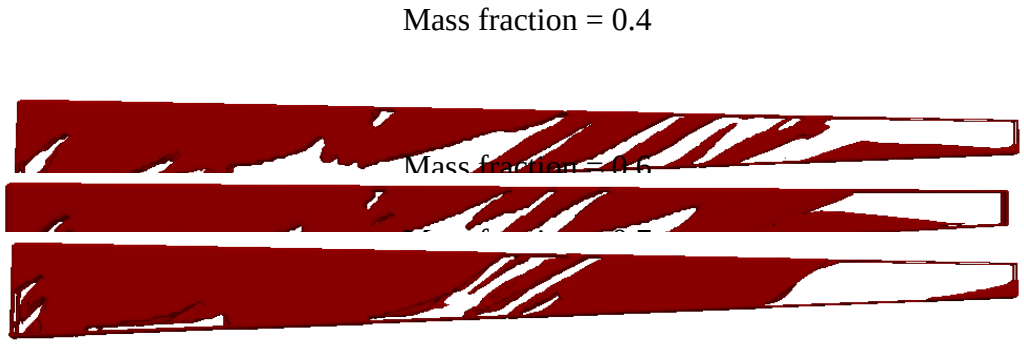

Figure 5.10: Optimal wing topologies (top view) for various mass fractions. (Red regions represent solid material, whereas the grey regions represent void).

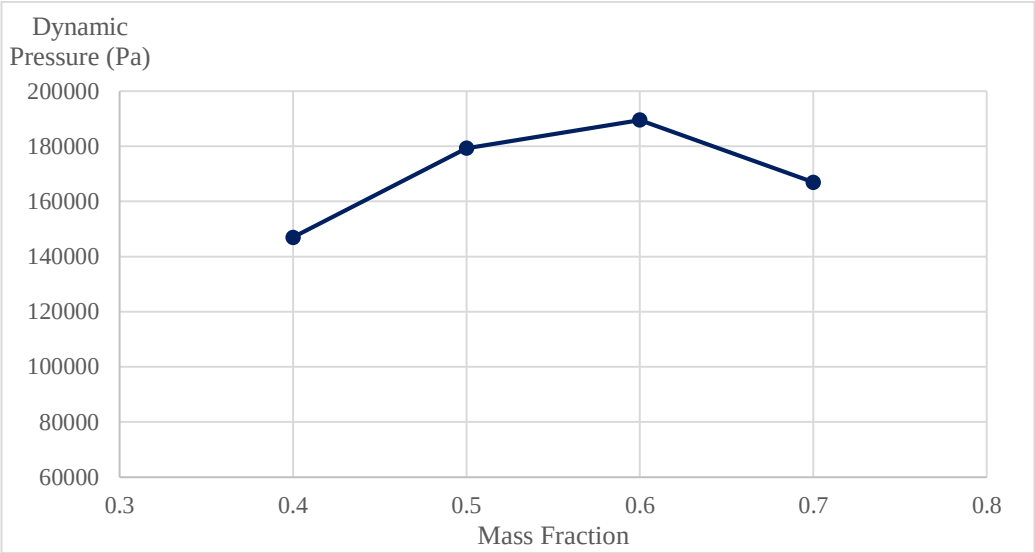

Figure 5.11: Flutter dynamic pressures corresponding to the mass fraction constraint.

5.5 Conclusion

Mode tracking is important during aeroelastic optimisation in order to track the critical modes. Existing mode tracking such as the modal assurance criterion method and eigenvector orthogonality correlation method were discussed. These methods can experience in failure to track modes. An improved eigenvector orthogonality correlation method was introduced in this work by employing the Hungarian algorithm to track the modes during divergence or flutter analysis.

To demonstrate whether the improved correlation method is working, flutter maximisation problem was formulated to maximise the divergence or flutter for high aspect ratio wings. The SLP level set method was used to solve the flutter maximisation problem. Mode switching was found during the optimisation as the critical point changed from divergence to flutter. The improved correlation method tracked the modes successfully and prevented discontinuity in the optimisation. Both divergence and flutter dynamic pressure were improved at a slow rate. A range of mass fraction constraints were imposed to optimise the same

wing model. The fact that all the optimisation cases were converged to similar topologies showed that improved correlation method was suitable for the flutter problem. The results showed that the mass distribution can directly affect the critical flutter dynamic pressure.

Chapter 6

Investigation of Local Modes

6.1 Introduction

When solving topology optimisation of a continuum structure with a dynamic constraint such as flutter, another challenge will arise is the local modes phenomenon due to the dynamic characteristics. When the level set method is used in topology optimisation, local modes appear in the low-density areas because of their reduced stiffness. In reality, these local modes are non-existent since the low density area represents a void region in the structure. This is an existing problem in aeroelastic optimisation with dynamic constraints (Pederson 2000).

In this chapter aeroelastic optimisation with natural frequency method is first conducted to identify the local modes. The assumed mode method and effective modal mass method are then proposed to try and eliminate the local modes. Before conducting the investigations, it is necessary to discuss the Sequential Linear Programming (SLP) level set optimisation method, which will be applied to solve the problems in this chapter. Both the aerodynamic and structural wing models that are used for the investigation will also be discussed.

6.2 Problem Definition

It is important to investigate what actually happens in the local modes. To demonstrate that, an optimisation model is formulated by minimising the wing mass, M_w subject to the continuous flutter constraint, G_f. Compliance is a static analysis and will not contribute to the dynamic part, therefore compliance is not considered in the optimisation problem. The optimisation formulation is described in the equations below:

$$\begin{aligned} &\text{Minimise: } M_w = \rho \cdot Vol \\ &\text{Subject to: } G_f(q) < 0 \ , \ q \in \{q_{min}, q_{max}\} \end{aligned} \tag{6.18}$$

where ρ is the material density, Vol is the volume of the wing box, $q_{\min}$ and $q_{\max}$ are the minimum and maximum flutter point dynamic pressure, respectively. The continuous flutter constraint, G_f is defined in previous chapter in Eq. (4.49) as:

$$G_f(q) = \begin{cases} 1 - (q/q_{\lim}) & \text{if } q > q_{\lim} \ \& \ \mathrm{Re}(p) > 0 \\ \mathrm{Re}(p)/p_{\mathrm{ref}} & \text{if } q < q_{\lim} \ \& \ \mathrm{Re}(p) < 0 \\ (\mathrm{Re}(p)/p_{\mathrm{ref}}) \cdot \left(1 - (q/q_{\lim})\right)^2 & \text{if } q < q_{\lim} \ \& \ \mathrm{Re}(p) > 0 \\ 1 - (q/q_{\lim}) + (\mathrm{Re}(p)/p_{\mathrm{ref}}) & \text{if } q > q_{\lim} \ \& \ \mathrm{Re}(p) < 0 \end{cases} \tag{6.19}$$

The wing mass sensitivity, $\frac{\partial M_w}{\partial \Omega}$ and the continuous flutter sensitivity, $\frac{dG_f(q)}{d\Omega}$ are previously derived in Chapter 4.4.2 and Chapter 4.5.3, respectively. The sensitivities are first calculated at the Gauss points in each finite elements. A least squares interpolation method is then used to calculate the sensitivities at the boundary nodes. The SLP level set method is used to solve the optimisation problem in Eq. (6.18) and the details of this method is explained in the next section.

6.3 Sequential Linear Programming Level Set Topology Optimisation

In this section the new SLP level set method outlined in Dunning and Kim (2014) is described. The level set method makes use of the discretised form of the Hamilton-Jacobi equation shown in Eq. (2.3) to update the structural shape. Gradient based methods are employed to solve the problem in Eq. (6.18). This requires the first derivatives of the objective and constraints with respect to the boundary, Ω. Shape derivatives provide information about how a function changes over time with respect to a movement of the boundary and usually takes the form of a boundary integral (Allaire et al. 2004). Hence the shape derivative for the wing mass, M_w is:

$$\Delta t \frac{\partial M_w}{\partial \Omega} = \Delta t \int_{\Gamma} \left(s_f \cdot V_n\right) d\Gamma \tag{6.20}$$

where Δt is the fictitious time step, V_n is a velocity function acting normal to the boundary, s_f is the shape sensitivity function for M_w, which is continuous along the boundary. The shape sensitivity and velocity functions vary along the boundary and are usually assumed to be smooth. Therefore, the shape derivative is characterised as a boundary integral involving a velocity function. The time step in Eq. (6.20) can be eliminated by replacing the velocity function by a boundary movement function, z:

$$\Delta t \frac{\partial M_w}{\partial \Omega} = \int_{\Gamma} \left(s_f \cdot z\right) d\Gamma, \quad z = \Delta t \cdot V_n \tag{6.21}$$

In order to evaluate the integral, the boundary is discretised. The discretisation of the shape derivative for the wing mass can be written as:

$$\Delta t \frac{\partial M_w}{\partial \Omega} \approx \sum_{i=1}^{n} \left(s_{f,i} \cdot z_i \cdot l_i\right) \tag{6.22}$$

where l_j is a discrete length of the surface area in 3D wing around a discrete point i, $s_{f,i}$ is the discrete value of the wing mass shape sensitivity, n is the number of discrete points. Similarly, discretisation of the constraint function shape derivatives (continuous flutter constraint, G_f) can be written as:

$$\Delta t \frac{\partial G_f}{\partial \Omega} \approx \sum_{i=1}^{n} \left(s_{g,i} \cdot z_i \cdot l_i \right) \tag{6.23}$$

where $s_{g,i}$ is the discrete value of the continuous flutter shape sensitivity.

To obtain a smooth boundary in the solution it is necessary to have a smooth update velocity. With smooth boundary sensitivities, this can be achieved by setting the normal velocity to be a weighted linear sum of the boundary sensitivities:

$$V_n(w) = w_f \cdot s_f + w_g \cdot s_g \tag{6.24}$$

where w is the velocity weights. The value of the velocity weights can be determined and optimised by formulating a linear sub-problem based on the sensitivities and solved using a SLP method. This is to find the maximum improvement in the objective function while satisfying the continuous flutter constraint. This formulation is shown in Eq. (6.25) below:

$$\begin{aligned} &\text{Minimise: } \frac{\partial M_w}{\partial \Omega} = \Delta t \left(s_f \cdot V_n(w) \right) \\ &\text{Subject to: } \frac{\partial G_f}{\partial \Omega} = \Delta t \left(s_g \cdot V_n(w) \right) \\ &w_{min} < w < w_{max} \end{aligned} \tag{6.25}$$

This SLP level set optimisation method is discussed in detail in Dunning and Kim (2014). Once the velocity function in Eq. (6.24) is evaluated, the updated velocity can be extended to the level set function values at the finite element nodes using the fast marching method (Sethian 1999). The main advantage of the SLP method is that it can simultaneously handle multiple constraints and non-level set design variables.

6.4 Aircraft Wing Model

The SLP level set topology optimisation method is applied to optimise a 3D wing box. The wing is modelled by a 25×40 aerodynamic mesh and the wing box is modelled by 136500 finite elements. The aerodynamic mesh and the structural mesh are modelled using the Doublet Lattice Method (DLM) and the Finite Element Method (FEM), respectively. Both models are shown in Figure 6.12 and Figure 6.13. The computation of the aerodynamic load that is applied to the finite element model is previously discussed in Chapter 3. The wing box structure consists of 3mm thickness of shell elements, which represents the wing skin. The wing skin has a total 12500 shell elements and they will not be optimised throughout the optimisation. The remaining structure consists of 124000 solid elements, and all the solid elements are design variables that will be optimised.

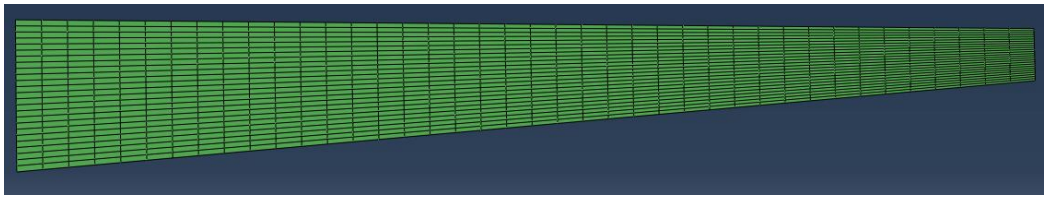

Figure 6.12: Aerodynamic (Doublet Lattice) 2D model

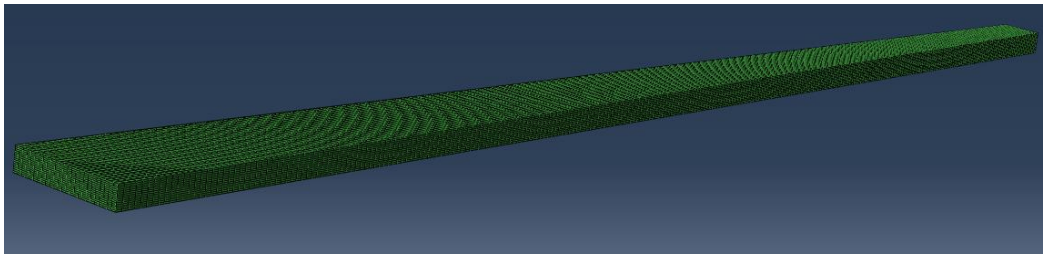

Figure 6.13: Structural Finite Element 3D model

The aircraft flight conditions, wing external geometry, wing box geometry and wing material properties are described from Table 6.5 to Table 6.8 below:

Flight Conditions

Cruise Mach number, M_∞	0.85
Cruise altitude (*ft*)	44000
Cruise weight (*kg*)	2.5×10^5
Air density at cruise (kg/m^3)	0.210

Table 6.5: Aircraft flight conditions.

Wing External Geometry

Aspect ratio	18
Reference wing area (m^2)	222.22
Taper ratio	0.35
Root chord (*m*)	5.21
Tip chord (*m*)	1.82
Mean aerodynamic chord (*m*)	3.79
Half wing span, (*m*)	31.62
¼-chord sweep angle	0 º
Thickness-to-chord ratio (*m*)	0.15

Table 6.6: Properties of the wing external geometry.

Wing Box Geometry

Wing box root chord (m)	3.12
Wing box tip chord (m)	1.09

Table 6.7: Properties of the wing box geometry.

Wing Material Properties

Young's modulus (Pa)	70×10^9
Poisson's ratio	0.30

Table 6.8: Wing material properties.

The design cruise speed, U_d is the multiplication of the given Mach number and the speed of sound of the cruising altitude, U_s:

$$U_d = M_\infty \cdot U_s \tag{6.26}$$

The critical flutter speed is set to be 20% above the design cruise speed in accordance to the Joint Aviation Requirements (JAR-25.629). Therefore, the critical flutter dynamic pressure can be obtained as:

$$q^* = 20\% \cdot \left(\frac{1}{2} \cdot \rho_\infty \cdot U_d^2\right) \tag{6.27}$$

The flutter analysis is previously described in Chapter 3.5 to calculate the critical flutter speed. Using the flight conditions in Table 6.5, the flutter dynamic pressure is deduced to be 22500Pa. The initial structural design consists of 150 holes (3 holes along the chordwise direction and 50 holes along the spanwise direction) as shown in Figure 6.14. The black region represents solid materials and the grey region represents void.

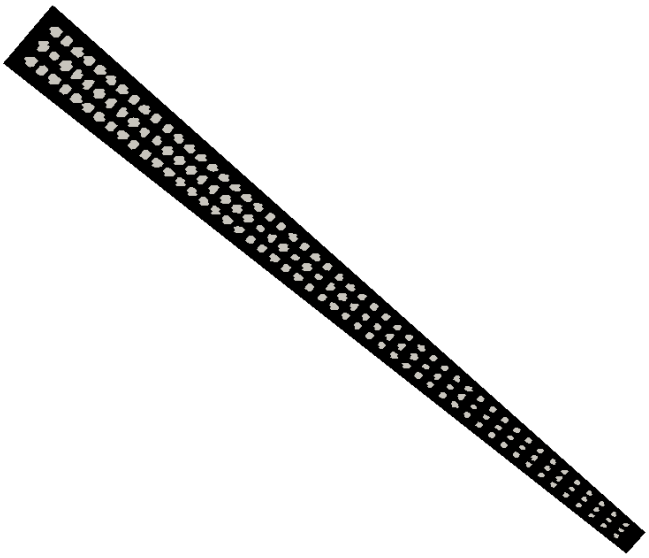

Figure 6.14: Initial structural wing design (top view).

6.5 Aeroelastic Optimisation with Natural Frequency Method

Aeroelastic optimisation is first carried out to solve the problem in Eq. (6.18) using the natural frequency method. In the natural frequency method, the natural frequencies and mode shapes are updated as the new wing topology structure is being updated in the new iteration.

The modal analysis is performed for the first 15 modes in this study. The natural frequencies and mode shapes for the initial wing are tabulated in Table 6.9. However, one issue is found when using the unsteady Doublet Lattice Method (DLM) in the flutter analysis. The unsteady model in the DLM is comprised of planar lifting surfaces. The lifting surface edges must be aligned along the far field streamlines and these surface produce only normal forces and moments about the vertical axis (Rodden and Johnson 1994). Therefore, only the vertical displacements are computed. Thus, only the bending modes and torsion modes can be interacted with the DLM. The edgewise bending modes and the translation modes will have no effect on the flutter results because there is no vertical motion

deflected from the wing. In order to increase the computational and numerical efficiency, the pure edgewise bending modes and the pure translation modes that are not contributed to flutter can be eliminated before performing the flutter analysis. The number of modes is now reduced to 10, without the edgewise bending modes and the translation mode, as shown in Table 6.10.

Mode	Natural Frequency (rad/s)	Mode Shapes
1	3.85	1st bending mode
2	18.28	1st edgewise bending mode
3	20.20	2nd bending mode
4	53.54	3rd bending mode
5	77.46	2nd edgewise bending mode
6	99.18	1st torsion mode
7	102.90	4th bending mode
8	168.32	5th bending mode
9	186.39	3rd edgewise bending mode
10	236.21	2nd torsion mode
11	249.51	6th bending mode
12	292.34	1st translation mode
13	336.86	4th edgewise bending mode
14	345.65	7th bending mode
15	379.55	3rd torsion mode

Table 6.9: Natural frequencies and mode shapes for initial wing (first 15 modes)

Mode	Natural Frequency (rad/s)	Mode Shapes
1	3.85	1st bending mode
2	20.20	2nd bending mode
3	53.54	3rd bending mode
4	99.18	1st torsion mode
5	102.90	4th bending mode
6	168.32	5th bending mode
7	236.21	2nd torsion mode
8	249.51	6th bending mode
9	345.65	7th bending mode
10	379.55	3rd torsion mode

Table 6.10: Natural frequencies and mode shapes for initial wing (after removing edgewise bending modes and translation mode)

The convergence histories of the aeroelastic optimisation are shown in Figure 6.15. Two issues are identified from the results. The first issue occurs between the 8th and 12th iterations, where the wing mass is not being optimised as only approximately 0.17% reduction in wing mass. This is caused by the mode switching between mode 9 and 10. At the 8th iteration, mode 9 has a combination of edgewise bending mode with slight torsion, whereas mode 10 is a pure torsion mode, as shown in Figure 6.16. However, these two modes switch around at the 9th iteration. The eigenvectors of both mode 9 and 10 are tracked. The damping curves in Figure 6.17 and Figure 6.18 show that the flutter dynamic pressure for both 8th and 9th iterations are calculated as 14865Pa (mode 1). The flutter sensitivities is computed at both critical flutter dynamic pressures so that the optimisation is not entirely discontinued. At the 12th iteration, the mode switching problem is resolved as the edgewise bending mode no longer exists. The critical dynamic pressure is increased by 25.1% to 19840Pa (mode 1).

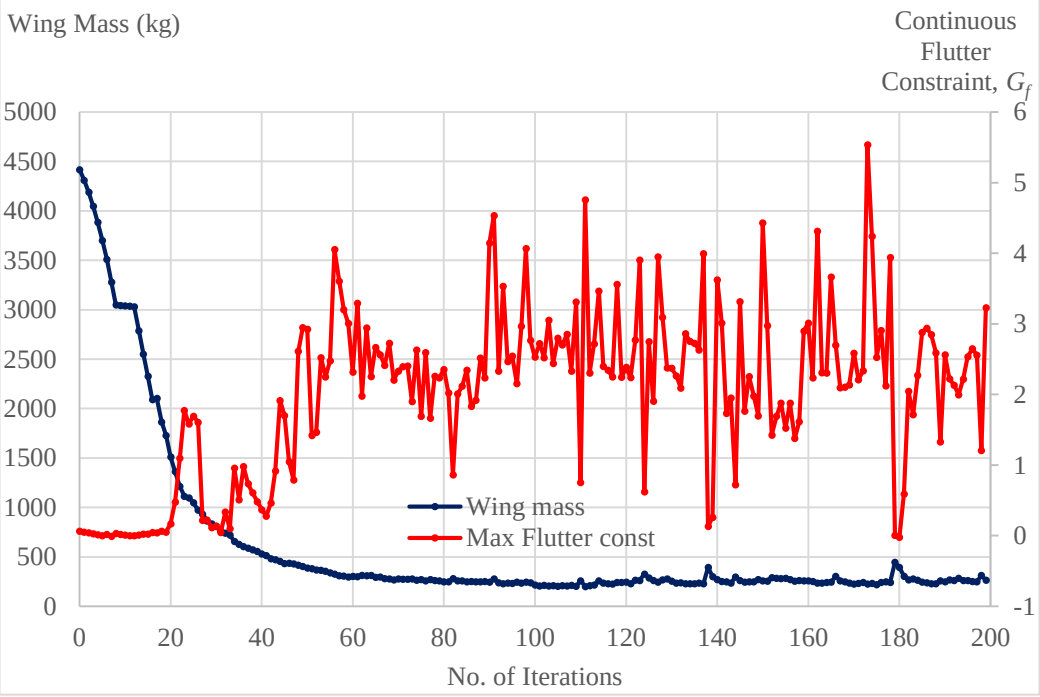

Figure 6.15: Convergence histories of the wing mass and continuous flutter constraint for natural frequency method.

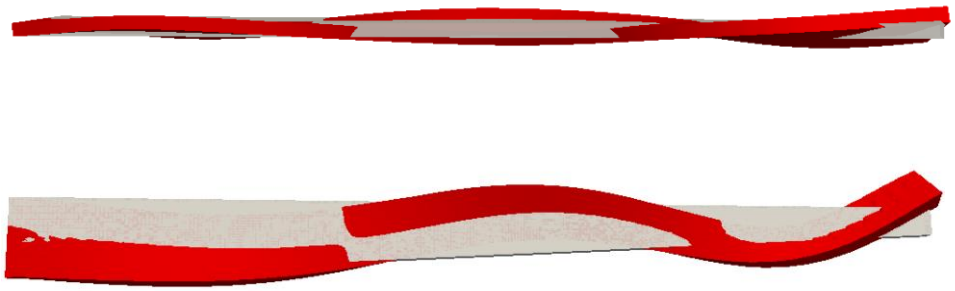

Figure 6.16: Mode shape of mode 9 at the 8th iteration (a) side view (b) top view (Red colour represents mode shape).

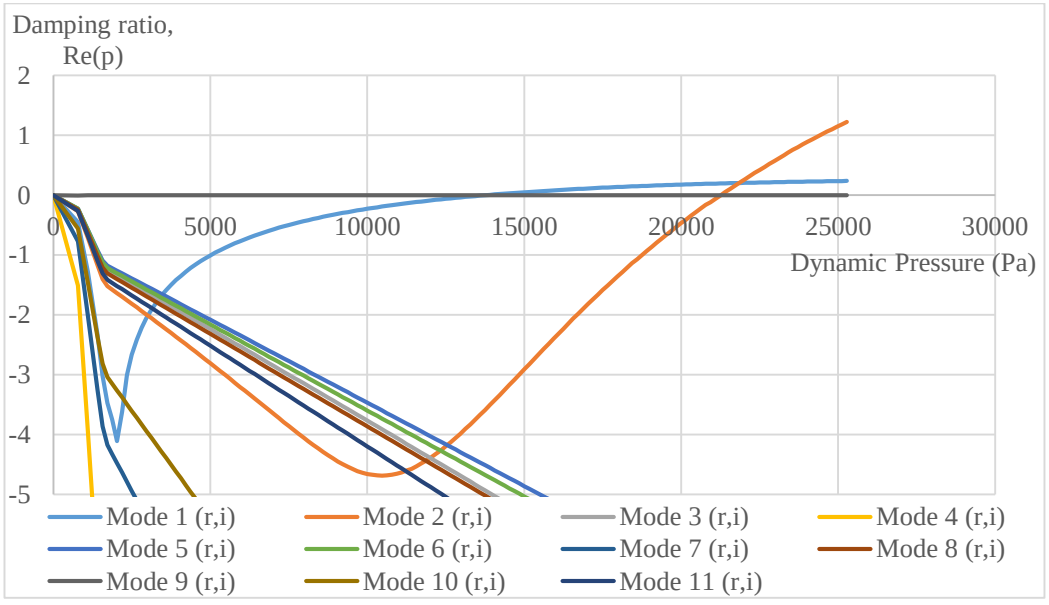

Figure 6.17: Damping ratio curve at the 8th iteration.

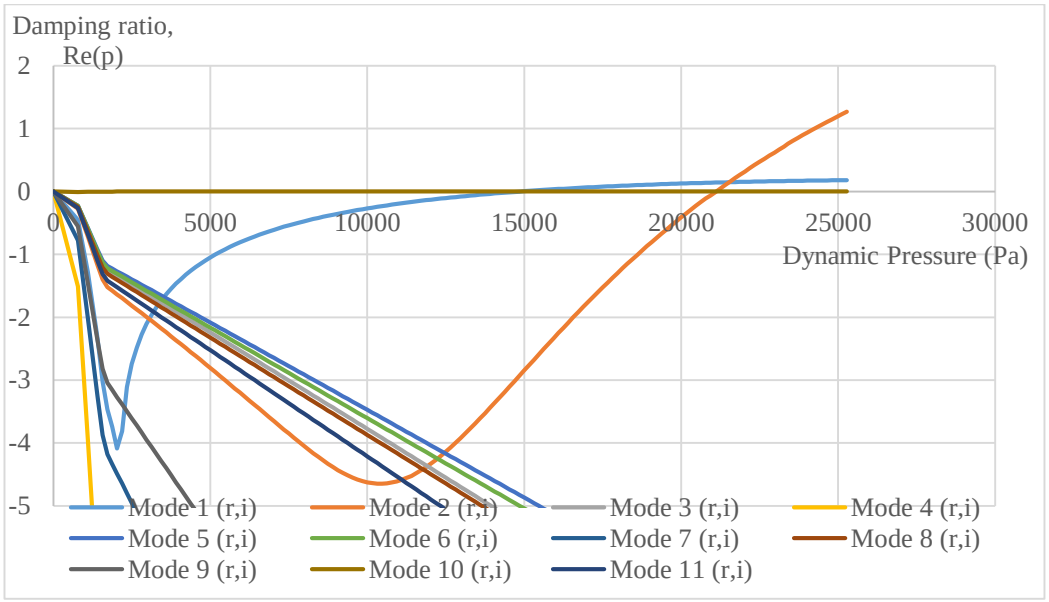

Figure 6.18: Damping ratio curve at 9th iteration.

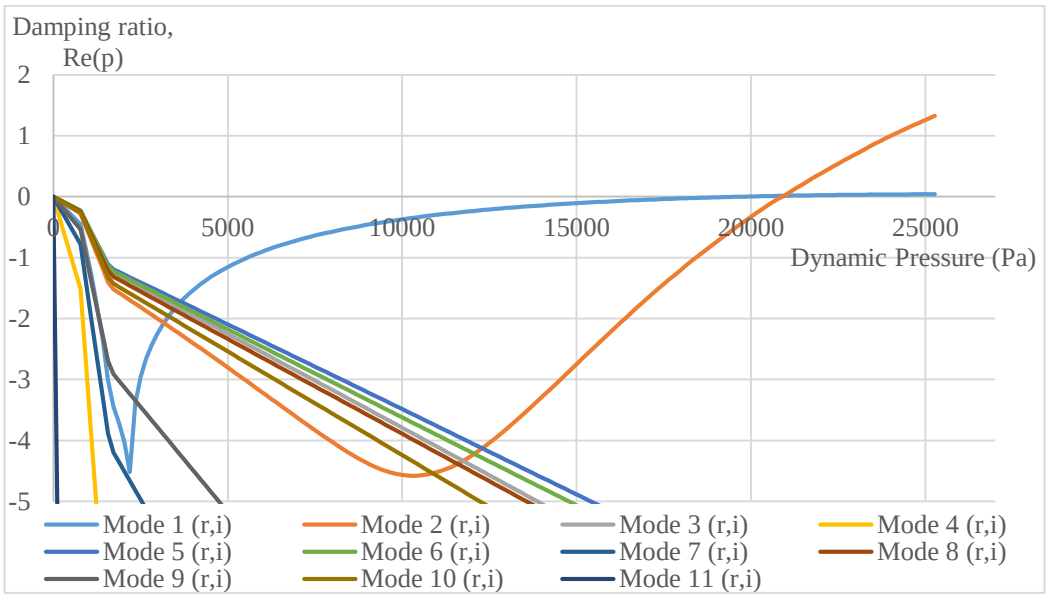

Figure 6.19: Damping ratio curve at 12th iteration.

The second issue is that the optimisation fails to converge, even at the 200th iteration. This phenomenon starts at the 22nd iteration in Figure 6.15, where local modes are found in the modal analysis. Both mode 5 and mode 9 are identified as local modes. The mode shapes for mode 5 and 9 are illustrated in Figure 6.20 and Figure 6.21. In both figures, there is a long 'spike' at the wing root. This can be explained by observing the structural topology at current iteration in Figure 6.22. The structural topology has many cut elements around the root chord. As the densities of these cut elements are vastly reduced, the elements are distorted and are leading to the local modes region. Figure 6.23 shows the damping curve for all the modes. Although the damping ratio for mode 5 and 9 remain at negative values and never cross the positive line, the perturbation from the local mode region creates a false implication that these two modes may become critical. Therefore, the flutter sensitivities for mode 5 and 9 are also calculated in this iteration. However, in reality, only mode 1 and 2 are critical. Since the flutter sensitivities for mode 1, 2, 5 and 9 are calculated, it is more difficult to satisfy all the flutter constraints. This explains why the solution in this iteration is infeasible. In the next iteration, the local modes disappear and the solution is becoming feasible. This problem carries on throughout the remaining optimisation and the solution never converges.

The local modes problem is found in the aeroelastic optimisation studies. In order to solve this problem, two different methods are proposed and investigated. The first method is the 'assumed mode method', and the second method is known as the 'effective modal mass method'. These two methods will be discussed and investigated in the next two sections.

Figure 6.20: Mode shape (side view) of mode 5 at 22nd iteration. (Red colour represents mode shape).

Figure 6.21: Mode shape (side view) of mode 9 at 22nd iteration. (Red colour represents mode shape).

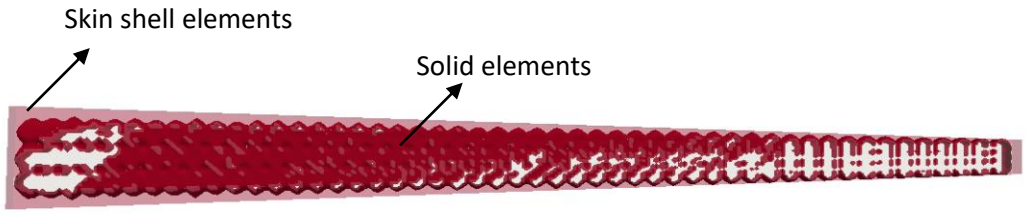

Figure 6.22: Structural topology at 22nd iteration (top view).

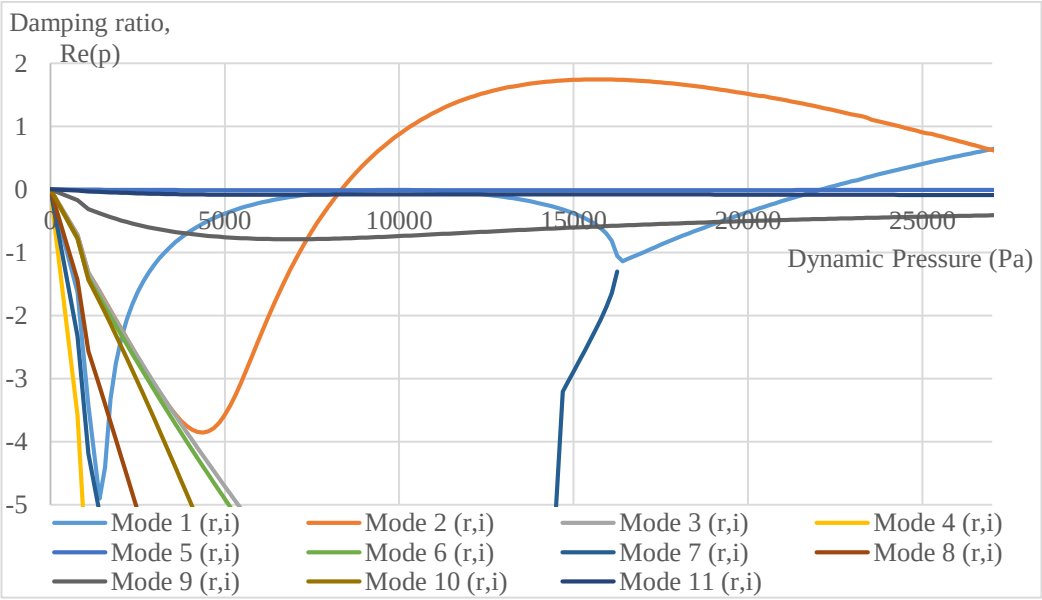

Figure 6.23: Damping ratio curve at 22nd iteration.

6.6 Investigation with Assumed Mode Method

The assumed mode method was introduced by Rule et al. (2001) to investigate the aeroelastic behaviour and active control of delta wings. This method involves the correct representation for replacing displacements with mode shapes and generalised coordinates. The displacements of a wing can be determined by the product of assumed mode shapes and the generalised coordinates. The modal basis function must be re-constructed at every iteration when using the assumed mode method. This is because the mode shapes (eigenvectors) are assumed be the same throughout the optimisation, but the mass and stiffness matrices are different as the structural topology is changing in every iteration.

The reduced mass and stiffness matrices are first calculated for the initial wing. If the eigenvector is normalised by the mass matrix, the reduced mass matrix $\widetilde{\boldsymbol{M}}$ becomes an identity matrix, whereas the reduced stiffness matrix $\widetilde{\boldsymbol{K}}$ becomes a diagonal matrix, as shown in Eq. (6.28):

$$\widetilde{\boldsymbol{M}} = \boldsymbol{\Phi}^T \boldsymbol{M} \boldsymbol{\Phi} = [\boldsymbol{I}] = \begin{bmatrix} 1 & 0 & \cdots & 0 \\ 0 & 1 & \cdots & 0 \\ \vdots & \vdots & \ddots & 0 \\ 0 & 0 & \cdots & 1 \end{bmatrix}$$
$$\widetilde{\boldsymbol{K}} = \boldsymbol{\Phi}^T \boldsymbol{K} \boldsymbol{\Phi} = \begin{bmatrix} \omega_1^2 & 0 & \cdots & 0 \\ 0 & \omega_2^2 & \cdots & 0 \\ \vdots & \vdots & \ddots & 0 \\ 0 & 0 & \cdots & \omega_n^2 \end{bmatrix} \tag{6.28}$$

For the assumed mode method, the mode shapes (eigenvectors, $\boldsymbol{\Phi}$) are retained throughout the optimisation. The global mass and stiffness matrices, $\boldsymbol{M}$ and $\boldsymbol{K}$, respectively, are varied during the optimisation. Substitute Eq. (6.28) into the flutter equation in Eq. (3.33), the new critical flutter points are computed in each iterations.

The optimisation problem in Eq. (6.18) is solved using the assumed mode method. The convergence history in Figure 6.24 shows that the solution is converged at the 120th iteration. Although there are some sudden jump in the continuous flutter constraint between 55th and 105th iterations, the difference is not as rigorous as compared to the natural frequency method (shown in Figure 6.15). To investigate what happens at the 55th, 81st, 85th and 103rd iterations where there is a sudden reduction in the continuous flutter constraint, the flutter analysis are plotted in Figure 6.25 for the critical flutter mode 1. A hump mode is discovered in mode 1 during these iterations, but the constraints have been imposed to suppress the hump mode. The critical flutter dynamic pressure is calculated to be 24650Pa. As the flutter constraint target is previously set as 22500Pa, the optimiser tries to find a better solution whilst reducing the flutter dynamic pressure to meet the constraint target. The solution is stabilised after the 105th iteration and it finally converges at the 120th iteration.

It is important to verify the solution for the assumed mode method. The reason is that the reduced mass and stiffness matrices in Eq. (6.28) are simply an approximation. One way to verify the final solution is by comparing the damping ratio from the assumed mode method to the natural frequency method. The critical

flutter dynamic pressure calculated in the assumed method and the natural frequency method are 22650Pa (mode 1) and 130Pa (mode 3), respectively. The damping curves for both methods are plotted in Figure 6.26 and Figure 6.27. This big difference is mainly caused by the inaccuracy of the reduced mass and stiffness matrices. The reduced mass stiffness matrix in Eq. (6.28) has become a non-identity matrix, and the reduced stiffness matrix has also become a non-diagonal matrix at 121st iteration. In reality, the wing mass is so small that most part of the wing box is hollow, so that the wing is going to cause flutter at the early stage. In addition, the assumed mode method also fails to capture many mode shapes compared to the natural frequency method. Some of the mode shapes are presented in Figure 6.28.

Therefore, the assumed mode method may improve the convergence of this problem by not considering the local modes, but the limitation is the accuracy of the results. An alternative method, known as the effective modal mass method will be discussed in the next section.

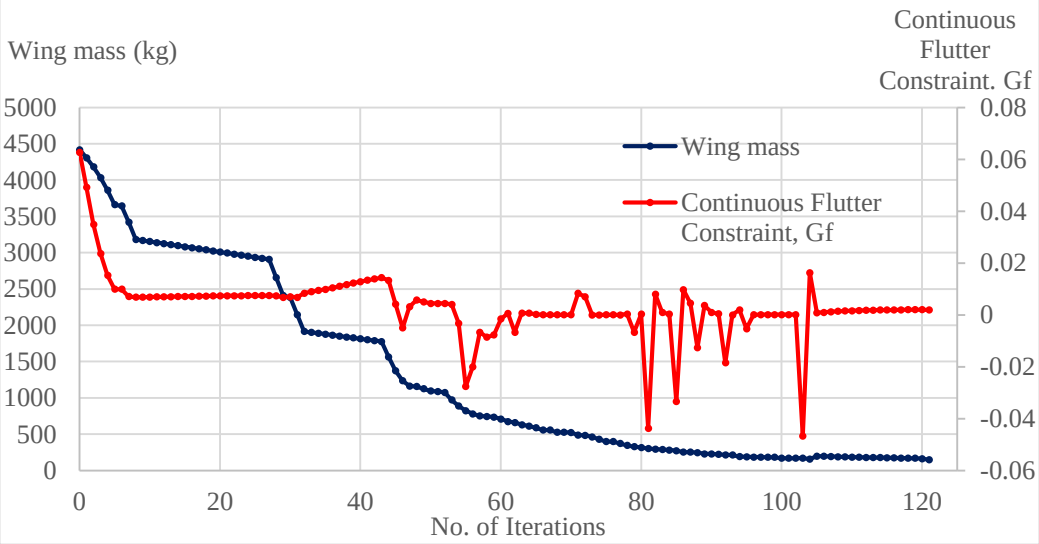

Figure 6.24: Convergence history of the wing mass and continuous flutter constraint for assumed mode method.

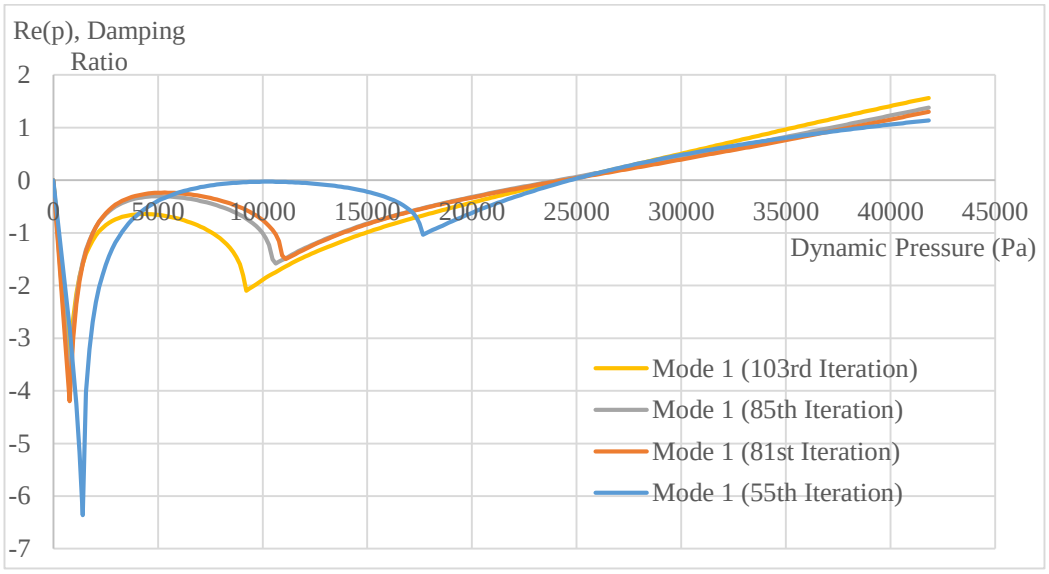

Figure 6.25: Convergence history of the wing mass and continuous flutter constraint for assumed mode method.

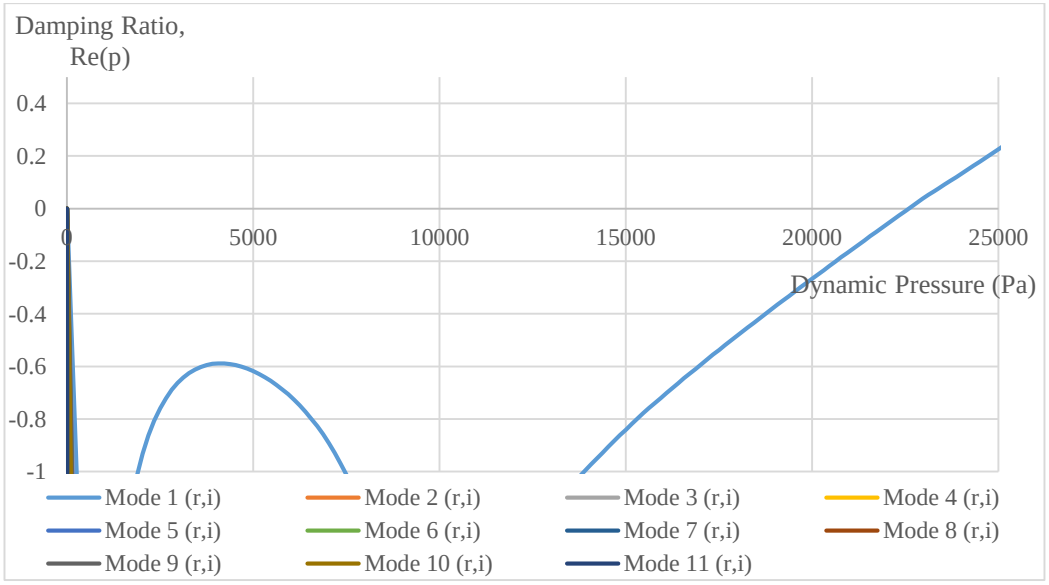

Figure 6.26: Damping ratio curve at the 121st iteration (assumed mode method).

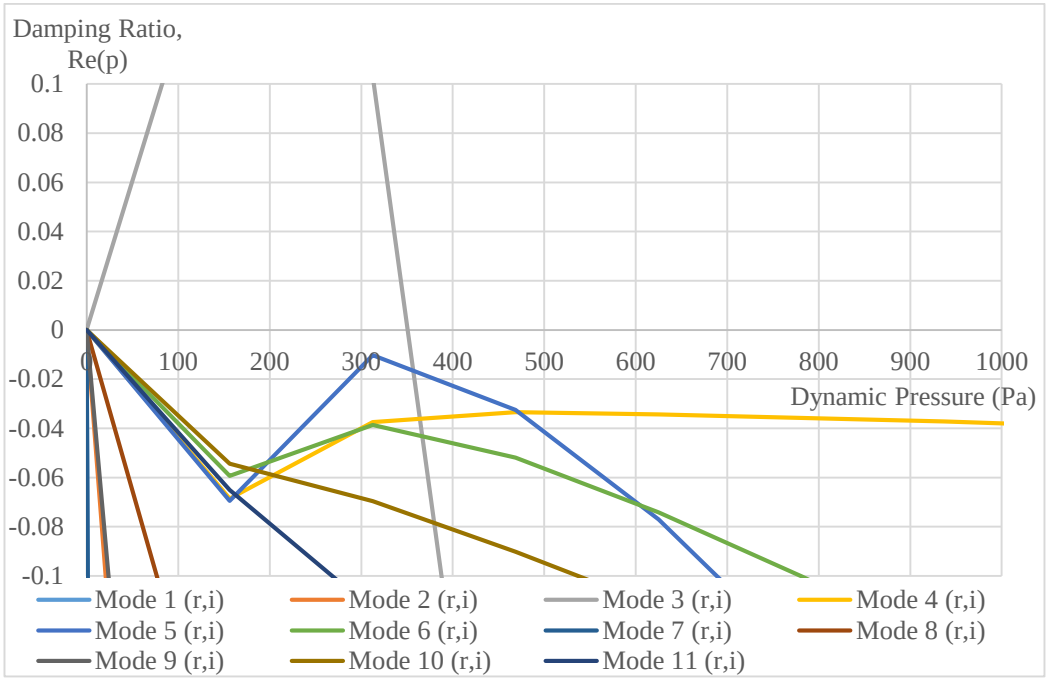

Figure 6.27: Damping ratio curve at the 121st iteration (natural frequency method).

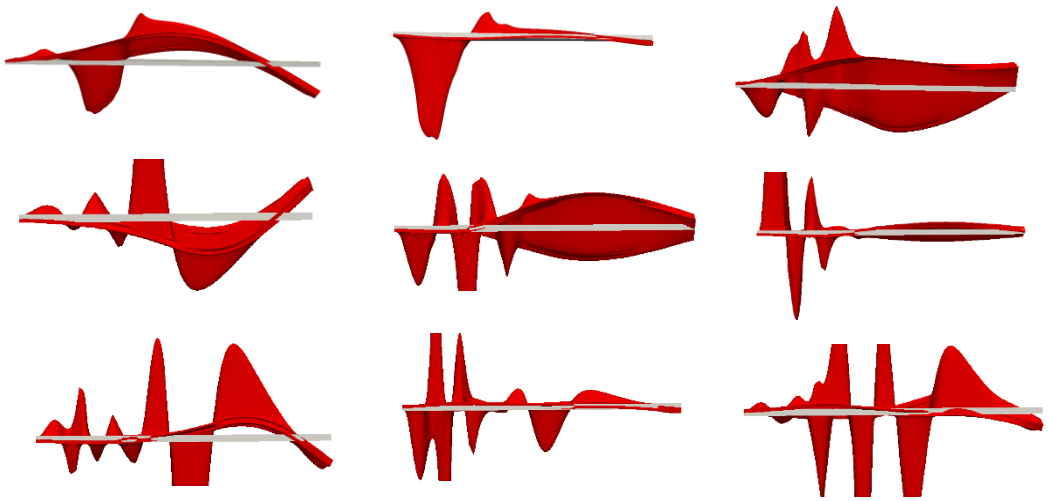

Figure 6.28: Example of mode shapes at the 121st iteration from the natural frequency method.

6.7 Investigation with Effective Modal Mass Method

The effective modal mass provides a method for judging the "significance" of a vibration mode. A particular effective modal mass may be a small fraction of an assembled system, say 5%, and could be deemed to be insignificant mode. Mode with relatively high effective mass can be readily excited by base excitation (Kim 2013). Consider an undamped system without rigid modes; the free vibration equation is:

$$\boldsymbol{M} \cdot \ddot{\boldsymbol{u}} + \boldsymbol{K} \cdot \boldsymbol{u} = 0 \tag{6.29}$$

The eigenproblem derived for the vibration and the structural systems can be written in terms of the eigenvalue ω_i^2 and eigenvector $\boldsymbol{\phi}_i$ of *i*-th mode as:

$$[\boldsymbol{K} - \omega_i^2 \cdot \boldsymbol{M}] \cdot \boldsymbol{\eta}_i = 0 \tag{6.30}$$

The eigenvector ϕ_i represents the mode shapes and is written in a matrix form:

$$\boldsymbol{\Phi} = \{\boldsymbol{\eta}_1, \boldsymbol{\eta}_2, \dots, \boldsymbol{\eta}_i\} \tag{6.31}$$

Pre-multiplying the mass matrix term by $\boldsymbol{\Phi}^{\mathrm{T}}$ provides:

$$\widetilde{\boldsymbol{M}} = \boldsymbol{\Phi}^T \cdot \boldsymbol{M} \cdot \boldsymbol{\Phi} \tag{6.32}$$

where $\widetilde{\boldsymbol{M}}$ is the diagonal matrix of generalised masses for the normal modes. Let τ be the influence vector which represents the displacements of the masses resulting from static application of a unit ground displacement. The influence vector induces a rigid body motion in all modes. A coefficient vector is defined as:

$$\bar{\boldsymbol{L}} = \boldsymbol{\Phi}^T \cdot \boldsymbol{M} \cdot \boldsymbol{\tau} \tag{6.33}$$

The modal participation factor matrix, Ψ_i for *i*-th mode is derived by taking the coefficient vector in Eq. (6.33) divide by the generalised mass matrix in Eq. (6.32):

$$\Psi_i = \frac{\bar{L}_i}{\widetilde{M}_{ii}} \tag{6.34}$$

The coefficient vector, $\bar{L}_{ij}$ may contain some negative values. The vector is squared so that all the values are positive. Therefore, the effective modal mass, $M_{eff,i}$ for i-th mode is derived as:

$$M_{eff,i} = \frac{\bar{L}_i^2}{\widetilde{M}_{ii}} \tag{6.35}$$

Note that the modal mass matrix $\widetilde{M}_{ii}$ = 1 for each index if the eigenvectors, ϕ_i have been normalised with respect to the mass matrix. Due to the orthogonality of the eigenvectors, the off-diagonal modal mass terms are zero regardless of the normalisation. Thus, the off-diagonal terms do not appear in Eq. (6.35).

From the results in Figure 6.20, it can be observed that the local modes are caused by the solid elements during the optimisation as the elemental densities are varied. The effective modal mass in Eq. (6.35) can be computed for shell and solid elements:

$$M_{eff,shell,i} = \frac{\bar{L}_{shell,i}^2}{\widetilde{M}_{shell,ii}} \tag{6.36}$$

$$M_{eff,solid,i} = \frac{\bar{L}_{solid,i}^2}{\widetilde{M}_{solid,ii}} \tag{6.37}$$

It has been shown in Figure 6.20 and Figure 6.21 that the distorted elements travel in vertical displacements. Thus, the ratio of effective modal mass between shell and solid elements for the vertical direction (z-axis) are:

$$R_{i,z} = \frac{M_{eff,shell,i,z}}{M_{eff,solid,i,z}} \tag{6.38}$$

The ratio of effective modal mass between shell and solid elements, $R_{i,z}$ is computed for all the interested modes, for every iteration. The data can then be analysed to retain the global modes and filter out the local modes.

Two examples are chosen to investigate the local mode problem using the effective modal mass method. The first example is to use the structural topology at the 22nd iteration from Figure 6.22 and the 27th iteration. The local modes occur at the 22nd iteration was explained with the aid of illustrations in Figure 6.20 and Figure 6.21. The $M_{eff,solid,z}$, $M_{eff,shell,z}$ and R_z values at 22nd iteration are calculated and plotted in Table 6.11. Note that the edgewise bending modes would have been removed prior to the effective modal mass method. The results show that the R_z values for the local modes in mode 5 and 9 are more than 1.0, whereas the remaining global modes are less than 1.0. For the global modes, the mass contribution for solid elements is at least three times higher than the shell elements. For the local modes, since only one small region around the root chord is excited and the remaining part has no movement, the mass contribution for solid elements are lower than the shell elements.

Mode	$M_{eff,solid,z}$	$M_{eff,shell,z}$	$R_z = M_{eff,shell,z} / M_{eff,solid,z}$
1	230.402041	55.089053	0.239100
2	101.868649	27.562500	0.270569
3	64.164906	6.888525	0.107357
4	2.585986	0.015906	0.006151
5	0.443796	0.497081	1.120068
6	4.640147	0.793632	0.171036
7	0.928795	0.282163	0.303795
8	23.943406	7.086776	0.295980
9	0.036092	0.112017	3.103628
10	0.083961	0.000177	0.002103

Table 6.11: Ratio of the effective modal mass at the 22nd iteration.

Another example is using the structural topology at the 27th iteration as shown in Figure 6.29. The wing structure in this iteration has three local modes, they are mode 5, 9 and 10. Figure 6.30 shows that these 3 local modes have similar mode shapes. Similar to the previous example, the results in Table 6.12 show that the R_z values for the local modes in mode 5, 9 and 10 are more than 1.0, which represents the local modes.

Figure 6.29: Structural topology at the 27th iteration (top view).

(a) (b) (c)

Figure 6.30: Mode shapes for (a) Mode 5 (b) Mode 9 (c) Mode 10.

Mode	$M_{eff,solid,z}$	$M_{eff,shell,z}$	$R_z = M_{eff,shell,z} / M_{eff,solid,z}$
1	139.877929	47.767450	0.341494
2	64.046408	27.323620	0.426622
3	7.247941	3.121936	0.430734
4	48.349772	3.838465	0.079390
5	0.342869	0.869911	2.537153
6	17.918289	7.637485	0.426240
7	0.049288	0.012129	0.246074
8	1.462165	0.231534	0.158350
9	0.012171	0.062345	5.122639
10	0.001447	0.161042	111.278596
11	2.956680	0.122430	0.041408

Table 6.12: Ratio of the effective modal mass at 27th iteration.

The results from the above two examples are consistent and clearly show that the local modes occur when $R_{i,z}$ values are more than 1.0. Therefore, the Eq. (6.38) below is applied in the optimisation problem in Eq. (6.18) as a constraint to retain the global modes:

$$R_{i,z} \leq 1.0, \text{ where } i = 1, 2, \ldots, \text{number of modes} \qquad (6.39)$$

The convergence histories of the wing mass and the continuous flutter constraint are shown in Figure 6.31. The problem converges reasonably smoothly towards an optimum solution, whilst the constraint is satisfied. The initial wing mass is 4395kg and the final wing mass is 1726kg, which is approximately 60.7%

reduction in mass. The optimum topology in Figure 6.32 suggests that more materials should be added between the root and the mid-span. It is also interesting to point out that at the initial wing topology, the critical flutter dynamic pressure is 15200Pa at mode 1, whereas at the final wing topology, the critical flutter dynamic pressure is around 28243Pa at mode 2. The damping ratio curves for both initial and final solutions are plotted in Figure 6.33. The reason why the critical flutter mode has changed is because initially the optimiser is trying to increase the flutter dynamic pressure at mode 1 (first bending mode) as the solution is infeasible. However, the flutter dynamic pressure at mode 2 (second bending mode) decreases at the same time. At 44th iteration mode 2 becomes critical, instead of mode 1.

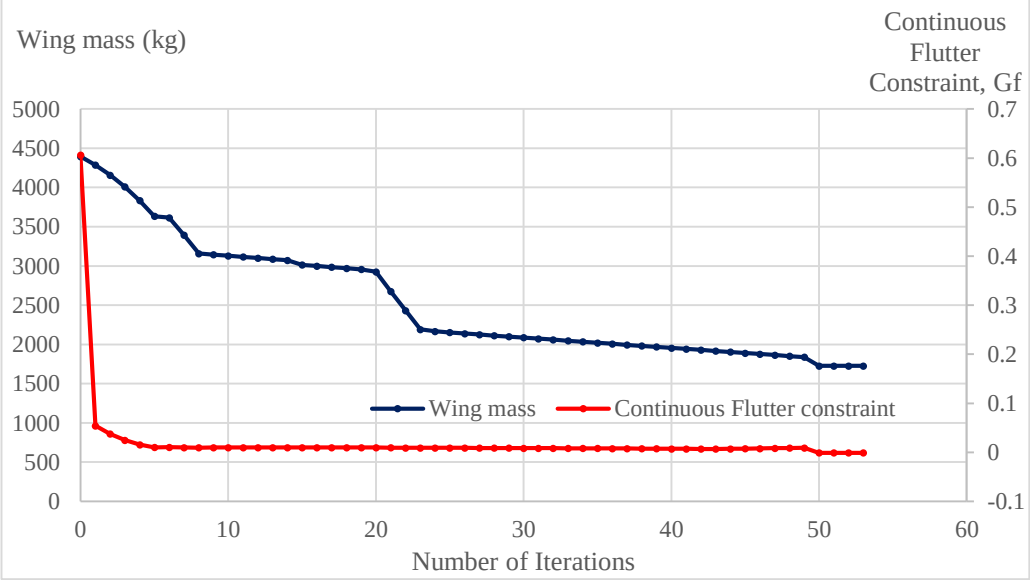

Figure 6.31: Convergence histories of the wing mass and continuous flutter constraint for using effective modal mass method.

Figure 6.32: Structural topology at final solution (53rd iteration).

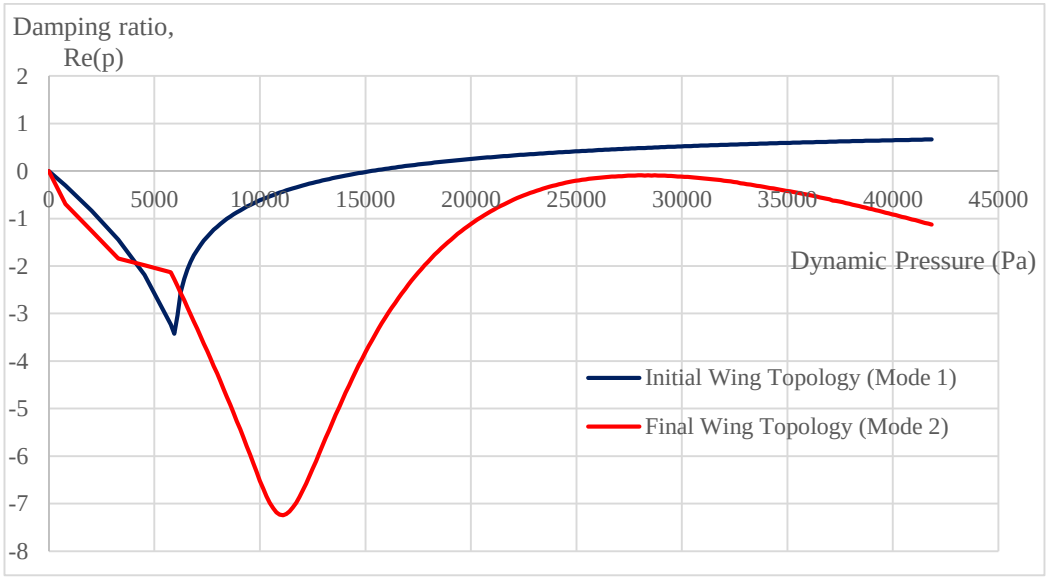

Figure 6.33: Damping ratio curve for initial and final solutions.

6.8 Conclusions

Local modes phenomenon is an existing issue in the aeroelastic topology optimisation and it causes discontinuity during the optimisation. High aspect ratio wing was modelled using doublet lattice method and finite element method. The aeroelastic topology optimisation study in this chapter is wing mass minimisation to satisfy the continuous flutter constraint. The analytical sensitivities of the wing mass sensitivity and flutter were derived in Chapter 4. The problem was optimised using the Sequential Linear Programming (SLP) level set based method.

The natural frequency method is adopted where the mode shapes are updated in every iteration, whilst updating the mass and stiffness matrices. A couple of local modes were observed as the solution failed to converge. To investigate the local modes problem, assumed mode method was implemented by retaining the same mode shapes of the initial wing topology throughout the optimisation. This method produced a much smoother convergence. However, when the final solution was verified against the natural frequency method, a big difference in the

critical dynamic pressure was found. Therefore, the assumed mode method was not ideal to resolve the local modes problem.

Effective modal mass method was developed and implemented to calculate the ratio of effective modal mass for shell and solid elements of the structural wing. Two examples from the natural frequency method was chosen to identify the local modes. An inequality constraint was set to eliminate the potential local modes in the optimisation. The results showed the effective modal mass method produced smooth convergence, as well as predicted the accurate critical flutter dynamic pressures.

Chapter 7

Aeroelastic Optimisation of High Aspect Ratio Wings

7.1 Introduction

The previous chapter on topology optimisation of an aeroelastic wing was to investigate and resolve the local mode problems but the structural stiffness was not considered in the optimisation. The structural stiffness can be represented by a compliance or strain energy. There are many works related to compliance based topology optimisation (Bendsøe and Sigmund 1999; Eschenauer and Olhoff 2001; Bruggi and Duysinx 2012). In order to ensure that the wing structure maintains some requisite stiffness, it is vital to enforce a constraint on the compliance while minimising the weight. This chapter consists of two optimisation stages. The first stage is to obtain a suitable compliance value by minimising the compliance subject to a volume constraint. The next stage is to minimise the high aspect ratio wing mass whilst satisfying both compliance and continuous flutter constraints using the Sequential Linear Programming (SLP) level set based method as

discussed in Chapter 6.3. Three different high aspect ratio wings are chosen for this study.

7.2 Minimisation of Compliance Subject to Volume Constraint

7.2.1 Optimisation Problem Definition

The optimisation problem is to minimise the compliance of the wing subject to volume constraints. Compliance is dependent on the structural displacements and the structural domain. The wing is deflected as the aerodynamic loads are applied to the wing. This results in the interaction between the aerodynamic and the structural models. The importance of aero-structural interaction was mentioned in Chapter 2.2.2, and will be considered during the optimisation.

$$\begin{aligned} &\text{Minimise:} \quad C(\boldsymbol{u}, \boldsymbol{\Omega}) \\ &\text{Subject to:} \quad Vol^* \leq 0.5 \times Vol \end{aligned} \tag{7.1}$$

where *C* is the compliance, *Vol** and *Vol* are the current volume and total volume of the wing box, respectively.

The compliance sensitivity in continuous form, $\frac{\partial C}{\partial \Omega}$ was derived in Chapter 4.4.2. The final compliance sensitivity on free boundary is:

$$\begin{aligned} \frac{\partial C}{\partial \Omega}(\Omega, u, w) &= \int_{\Gamma_0} V_n\big(E\varepsilon(u) \cdot \varepsilon(w) - N \cdot f_g \cdot (u + w) - A \cdot \rho g\big)\, d\Gamma_0 \\ A_c &= \frac{N}{L_\alpha} \int_{\Gamma_N} \big(f_\alpha \cdot (u + w)\big) d\Gamma_N \end{aligned} \tag{7.2}$$

The volume sensitivity of the wing box can be written in the continuous form as:

$$Vol = \int_{\Omega} H(\Omega) d\Omega \tag{7.3}$$

where $H(\Omega)$ is the Heaviside step function. Using the shape derivative defined in Eq. (4.7), the derivative of the volume of the wing box with respect to the design variable is:

$$\frac{\partial Vol}{\partial \Omega} = \int_{\Gamma} (s_{vol} \cdot V_n) d\Gamma \tag{7.4}$$

where the shape sensitivity function for s_{vol} is:

$$s_{vol} = \int_{\Omega} \frac{\partial H(\Omega)}{\partial \Omega} d\Omega = 1, \quad \text{for } \Omega \geq 0 \tag{7.5}$$

The least squares interpolation scheme is used to obtain smooth boundary sensitivities (Chapter 4.6). The SLP level set optimisation method from Chapter 6.3 is then used to compute the velocity function, V_n and update the level set function values.

7.2.2 Aircraft Wing Model

The wing used in this study is similar to the models described in Chapter 6.4. The initial structural design consists of 150 holes (3 holes along the chordwise direction and 50 holes along the spanwise direction). The doublet lattice model has 1000 elements, and the finite element model is constructed from a decomposition of 136500 elements. Both aerodynamic and structural models are coupled using the Finite Plate Spline (FPS) method as discussed in Chapter 3.4.1. During the optimisation process, the aero-structural coupling evaluations are to be converged to 10^{-4}.

The aircraft flight conditions, wing external geometry, wing box geometry and wing material properties are described from Table 7.1 to Table 7.4 below:

Flight Conditions

Cruise Mach number, M_∞	0.85
Cruise altitude (*ft*)	28000
Cruise weight (*kg*)	2.5×10^5
Air density at cruise (kg/m^3)	0.50

Table 7.1: Aircraft flight conditions.

Wing External Geometry

Aspect ratio	18
Reference wing area (m^2)	222.22
Taper ratio	0.35
Root chord (*m*)	5.21
Tip chord (*m*)	1.82
Mean aerodynamic chord (*m*)	3.79
Half wing span, (*m*)	31.62
¼-chord sweep angle	0 º
Thickness-to-chord ratio (*m*)	0.15

Table 7.2: Properties of the wing external geometry.

Wing Box Geometry

Wing box root chord (*m*)	3.12
Wing box tip chord (*m*)	1.09

Table 7.3: Properties of the wing box geometry.

Wing Material Properties	
Young's modulus (*Pa*)	70×10^9
Poisson's ratio	0.30

Table 7.4: Wing material properties.

7.2.3 Optimisation Results

The results in Table 7.5 shows that the compliance is reduced by 29% while meeting the volume (mass) constraint. Angle of attack is allowed to vary during the optimisation and the results show that it increases from 0.0076 ºto 0.373 º. An increase in the angle of attack indicates an increase in aerodynamic lift. However, the movement of the structural boundary increases the overall stiffness of the wing box. Thus, the tip deflection only increases by 6.3%. The topology of the final solution is shown Figure 7.1 which represents the top view contour plot and the section through the contour plot. The red region in the figure represents solid materials, whereas the white region represents void. It can be observed that the structural boundary moves from the tip chord toward the root chord, as well as from the trailing edge toward the leading edge. This can be explained by the way that the aerodynamic loading is applied on the structure. The loading on the root chord is the greatest, whereas the loading on the tip is the smallest. More material are expected to be preserved toward the root chord in order to support the aerodynamic loading. The internal configuration in Figure 7.1(a) suggests various thicknesses inside wing box from root to tip. It is also interesting to point out that the thicknesses for top and bottom skin are symmetrical. Finally, the compliance value of 6.00×10^5 Pa will be used for the next stage, with is the minimization of wing mass subject to compliance and continuous flutter constraints.

	Initial Topology	Final Topology
Compliance (*Pa*)	8.46×10^5	6.00×10^5
Wing mass (*kg*)	4417.11	2210
Angle of attack	0.0076 º	0.373 º
Tip deflection (*m*)	8.24	8.76

Table 7.5: Comparison between the initial and final wing topology.

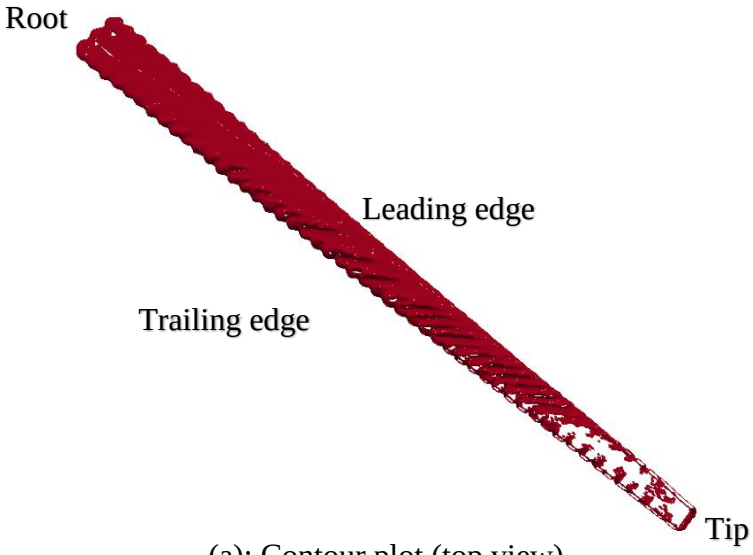

(a): Contour plot (top view)

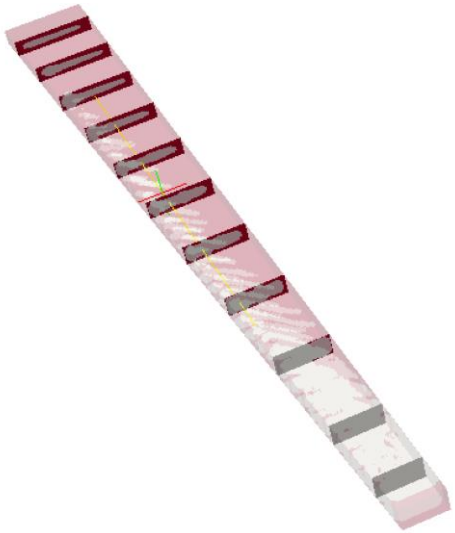

(b): Sections through the contour (do not represent ribs)

Figure 7.1: Structural topology of the final solution.

7.3 Minimisation of Wing Mass with Multiple Constraints

7.3.1 Optimisation Problem Definition

The optimisation problem that will be solved is minimisation of wing mass subject to flutter and compliance constraints as shown in Eq.

$$\begin{aligned} &\text{Minimise:} \quad M_w = \rho \cdot Vol \\ &\text{Subject to:} \quad G_f(q) < 0, \quad q_{min} < q < q_{max} \\ &\qquad\qquad C^* \leq C_{lim} \end{aligned} \tag{7.6}$$

where ρ is the material density, Vol is the volume of the wing box, M_w is the wing mass, q is the flutter point dynamic pressure, C^* is the compliance value, C_{lim} is the limit on the overall compliance. Since the flutter point is a non-linear function of the design variables, it can be discontinuous due to the switching of the critical flutter mode. The continuous flutter constraint function is represented by G_f, which is dependent on the flutter point dynamic pressure, q^*. G_f is previously defined in Eq. 4.49). q_{min} and q_{max} are minimum and maximum dynamic pressure within range of interest.

The SLP level set optimisation is extended to handle multiple constraints. The shape derivatives for all the objection and constraint functions are:

$$\begin{aligned} \Delta t \frac{\partial M_w}{\partial \Omega} &= \Delta t \int_\Gamma \left(s_f \cdot V_n\right) d\Gamma \\ \Delta t \frac{\partial G_f}{\partial \Omega} &= \Delta t \int_\Gamma \left(s_g \cdot V_n\right) d\Gamma \\ \Delta t \frac{\partial C}{\partial \Omega} &= \Delta t \int_\Gamma \left(s_c \cdot V_n\right) d\Gamma \end{aligned} \tag{7.7}$$

where Δt is the fictitious time step, V_n is a velocity function acting normal to the boundary, s_f, s_g and s_c are the shape sensitivity functions for M_w, G_f and C, respectively. In order to evaluate the integral, the boundary in Eq. (7.7) is discretised. The discretisation of the shape derivatives in Eq. (7.7) can be written as:

$$\Delta t \frac{\partial M_w}{\partial \Omega} \approx \sum_{i=1}^{n} \left(s_{f,i} \cdot z_i \cdot l_i\right)$$
$$\Delta t \frac{\partial G_f}{\partial \Omega} \approx \sum_{i=1}^{n} \left(s_{g,i} \cdot z_i \cdot l_i\right) \tag{7.8}$$
$$\Delta t \frac{\partial C}{\partial \Omega} \approx \sum_{i=1}^{n} \left(s_{c,i} \cdot z_i \cdot l_i\right)$$

where l_j is a discrete length of the surface area in the 3D wing around a discrete point i, n is the number of discrete points. To obtain a smooth boundary in the solution it is necessary to have a smooth updated velocity. With smooth boundary sensitivities, this can be achieved by setting the normal velocity to be a weighted linear sum of the boundary sensitivities:

$$V_n(w) = w_f \cdot s_f + w_g \cdot s_g + w_c \cdot s_c \tag{7.9}$$

where w_f, w_g, and w_f are the velocity weights for wing mass, continuous flutter constraint and compliance, respectively. The value of the velocity weights can be determined and optimised by formulating a linear sub-problem based on the sensitivities and solved using a SLP method. This is to find the maximum improvement in the objective function while satisfying the continuous flutter constraint. This formulation is shown in Eq. (7.10) below:

$$\begin{aligned} &\text{Minimise: } \frac{\partial M_w}{\partial \Omega} = \Delta t \left(s_f \cdot V_n(w)\right) \\ &\text{Subject to: } \frac{\partial G_f}{\partial \Omega} = \Delta t \left(s_g \cdot V_n(w)\right) \\ &\frac{\partial C}{\partial \Omega} = \Delta t\left(\mathrm{s_c} \cdot \mathrm{V_n(w)}\right) \\ &w_{min} < w < w_{max} \end{aligned} \tag{7.10}$$

Once the velocity function in Eq. (7.9) is evaluated, the updated velocity can be extended to the level set function values at the finite element nodes using the fast marching method (Sethian 1999).

7.3.2 Parametric Studies of High Aspect Ratio Wings

This study is to design high aspect ratio wings for a mission similar to a typical Boeing 777 which is to fly at Mach 0.85 at 28000ft altitude as described in Table 7.1. The wing external geometry, wing box geometry and wing material properties for three different aspect ratios are described from Table 7.6 to Table 7.8 below:

Wing External Geometry

Aspect ratio	18	20	24
Reference wing area (m^2)	222.22	246.91	296.29
Taper ratio	0.35	0.35	0.35
Root chord (m)	5.21	5.21	5.21
Tip chord (m)	1.82	1.82	1.82
Mean aerodynamic chord (m)	3.79	3.79	3.79
Half wing span, (m)	31.62	35.14	42.16
¼-chord sweep angle	0 º	0 º	0 º
Thickness-to-chord ratio (m)	0.15	0.15	0.15

Table 7.6: Properties of the wing external geometry.

Wing Box Geometry

Aspect ratio	18	20	24
Wing box tip chord (*m*)	3.12	3.12	3.12
Wing box root chord (*m*)	1.09	1.09	1.09

Table 7.7: Properties of the wing box geometry.

Wing Material Properties

Young's modulus (*Pa*)	70×10^9
Poisson's ratio	0.30

Table 7.8: Wing material properties.

For the constraints target value, the compliance for the wing is taken from the results in section 7.2.3. The critical flutter speed is set to be 20% above the design cruise speed in accordance to the Joint Aviation Requirements (JAR-25.629). Therefore, the critical flutter dynamic pressure can be obtained as:

$$q^* = 120\% \cdot \left(\frac{1}{2} \cdot \rho_\infty \cdot U_d^2\right) \tag{6.1}$$

The flutter analysis is previously described in Chapter 3.5 to calculate the critical flutter speed. Using the flight conditions in Table 7.1, the flutter dynamic pressure is deduced to be 18750Pa.

7.3.3 Optimisation Results

The initial structural design consists of 150 holes (3 holes along the chordwise direction and 50 holes along the spanwise direction) as shown in Figure 7.2. The doublet lattice model has 1000 elements, and the finite element model is constructed from a decomposition of 136500 elements. During the optimisation process, the aero-structural coupling evaluations are converged to 10^{-4}.

In order to capture the important modes in the flutter analysis, the first 15 modes are selected in this study. The effective modal mass that has been discussed in Chapter 6 is implemented to eliminate the potential local modes during the optimisation. It is expected that mode switching will occur during the optimisation, thus, continuous flutter constraint is vital in this study to be able to resolve the mode switching or hump mode issues.

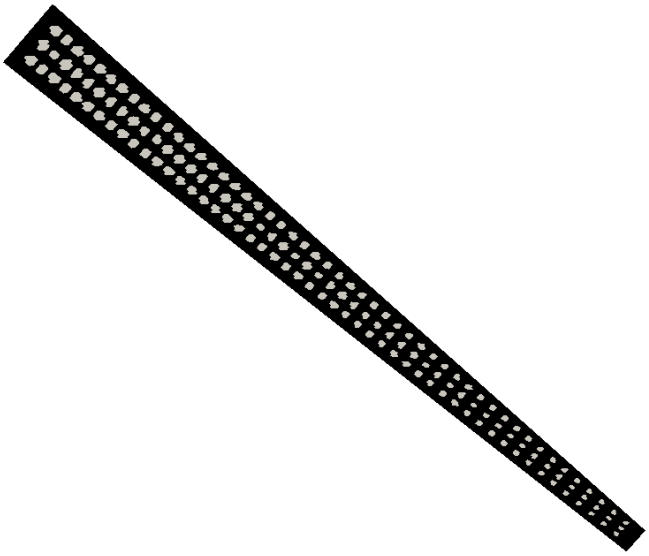

Figure 7.2: Initial structural design (top view).

Aspect Ratio	**18**		**20**		**24**	
	Initial	Final	Initial	Final	Initial	Final
Wing mass (*kg*)	4417.1	1921.3	5374.9	2666.1	6450.9	2537.6
% Mass reduction	-	56.5%	-	50.4%	-	60.7%
Compliance (*Pa*)	8.46×10^5	6.00×10^5	7.98×10^5	6.00×10^5	1.55×10^6	6.00×10^5
Flutter dynamic pressure (*Pa*)	15781	19843	14532	19844	9844	18838
Critical mode	Mode 1	Mode 2	Mode 1	Mode 1	Mode 1	Mode 1
Angle of attack	0.0076 º	0.77 º	0.91 º	0.35 º	0.76 º	0.52 º

Table 7.9: Main results showing initial and final solutions for high aspect ratio wings.

The main results of three different aspect ratio wings are tabulated in Table 7.9. For the wing with an aspect ratio of 18, the wing mass is the smallest due to the shortest span compared to other aspect ratio wings and there is a 56.5% mass reduction between the initial and final solutions. The compliance constraint is active as it is converged at 6.00×10^5 Pa, which is also the target value. The final solution is feasible as the flutter dynamic pressure is above the constraint value. There is also an increase of 25.7% for the flutter dynamic pressure between the initial and final solutions. Figure 7.3 show the convergence histories for the wing mass, compliance constraint and continuous flutter constraint. The optimisation converges reasonably smooth as the effective modal mass method manages to prevent the local modes and discontinuity in the optimisation. It is interesting to point out that the angle of attack has increased dramatically from 0.0076 ºto 0.77 º. This can be explained by the contour plots in Figure 7.4(a) as the final structural topology shows that there is not much material along the wing tip as compared to

the wing root. Therefore, the tip is deflected and induced higher angle of attack for the final topology.

The flutter dynamic pressure can be found from Figure 7.5 where it shows the damping curve for the critical modes. For simplicity, only the critical modes for the initial and final wing topologies are shown. For the initial wing, both mode 1 and 2 are critical, although mode 1 crosses the positive damping first. This mode, however, is a divergence instead of flutter. This is because the natural frequency is 0 rad/s at this mode, as shown in Figure 7.6. As the optimisation progresses, the optimiser is trying to increase the divergence for mode 1 to satisfy the prescribed constraint. On the other hand, the critical flutter dynamic pressure for mode 2 is decreasing as mode 1 and 2 have different mode shapes. For the final wing, mode 1 is not critical, whereas mode 2 is flutter at 19843Pa. The flutter frequency for the final wing is higher than the initial wing as the wing becomes stiffer.

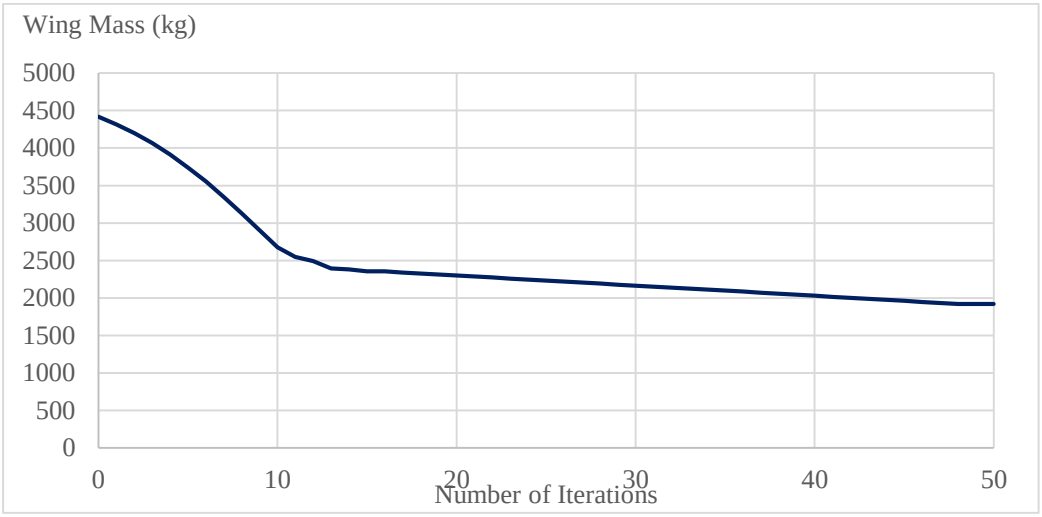

(a)

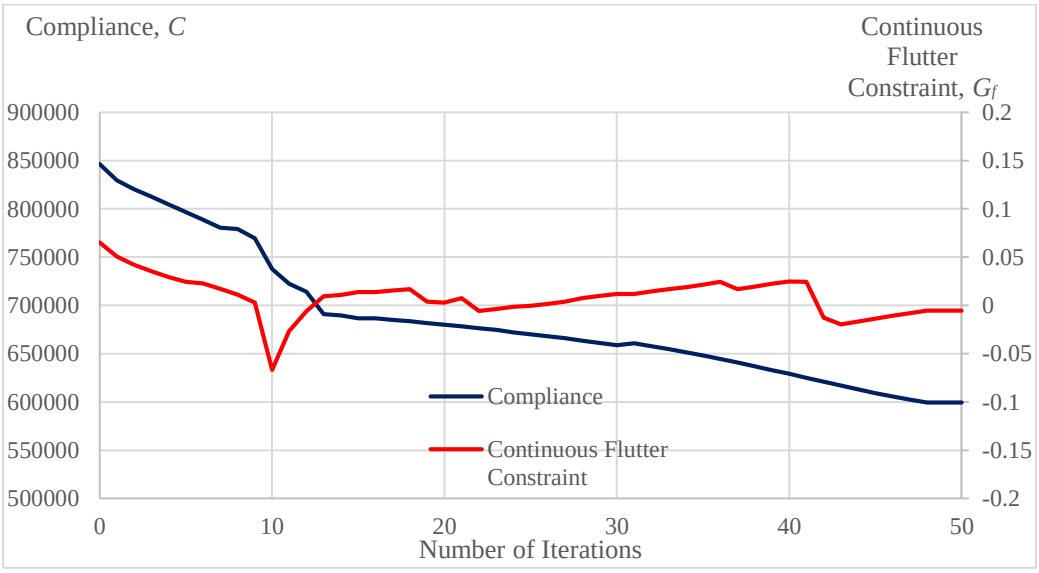

(b)

Figure 7.3: Optimisation convergence history for wing aspect ratio = 18: (a) Objective function – wing mass, (b) Constraint functions – compliance and continuous flutter constraint.

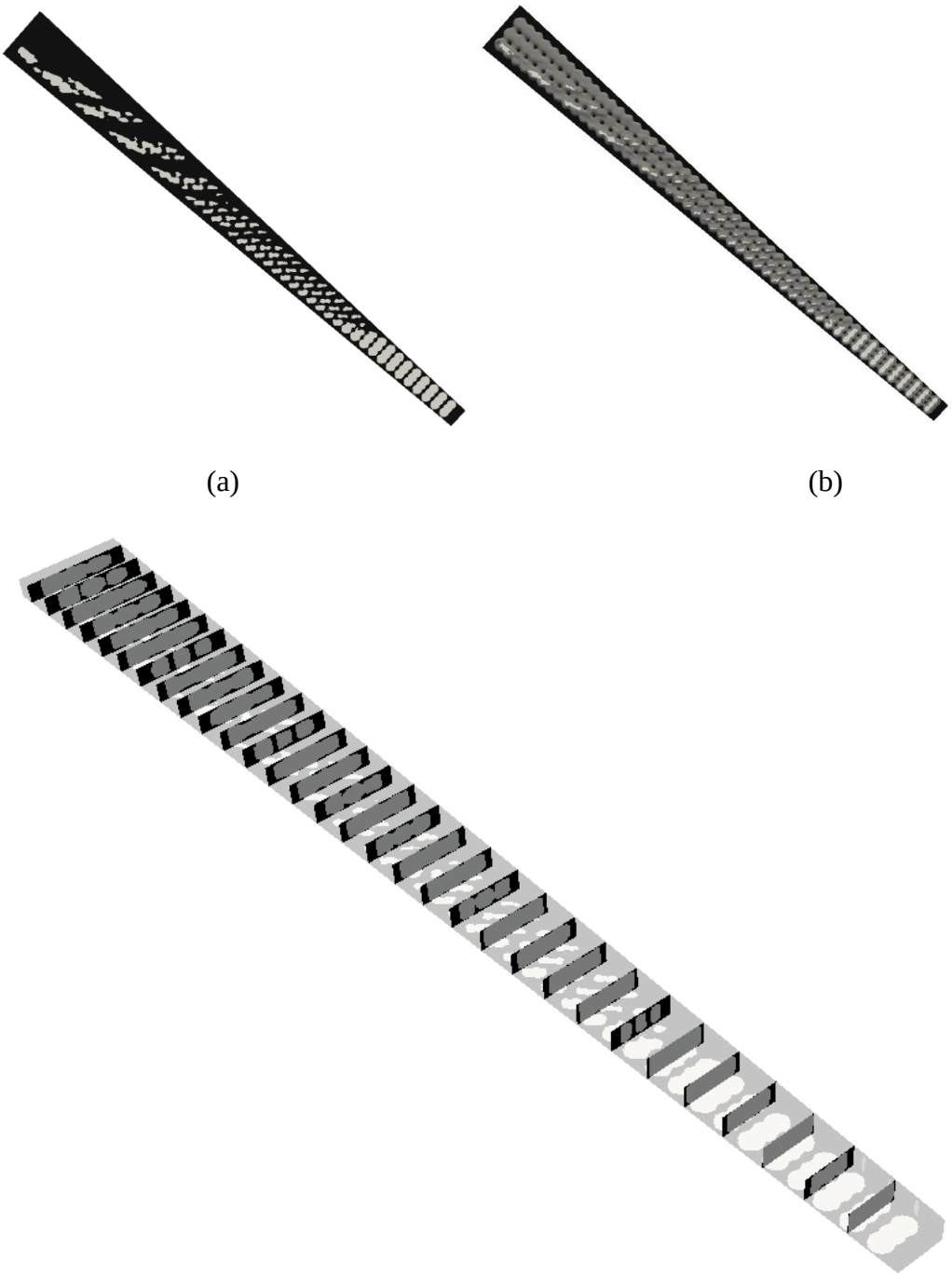

(a) (b)

(c)

Figure 7.4: Final solution for aeroelastic optimisation (AR = 18): (a) top view, (b) 3D contour of the internal structure, (c) sections through the contour (do not represent ribs)

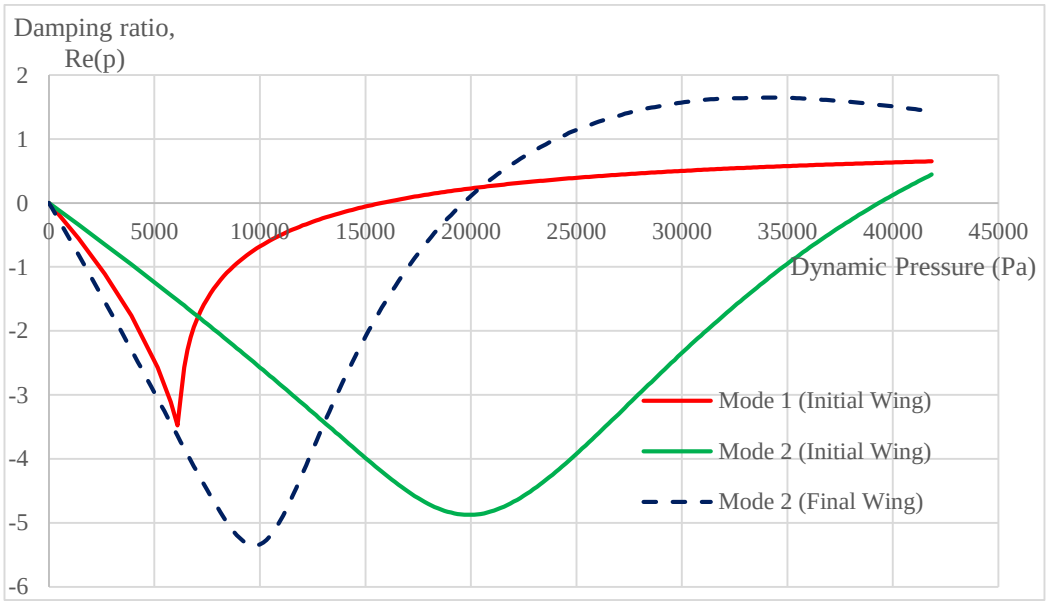

Figure 7.5: Damping ratio curve for critical flutter modes (initial and final wings: aspect ratio = 18).

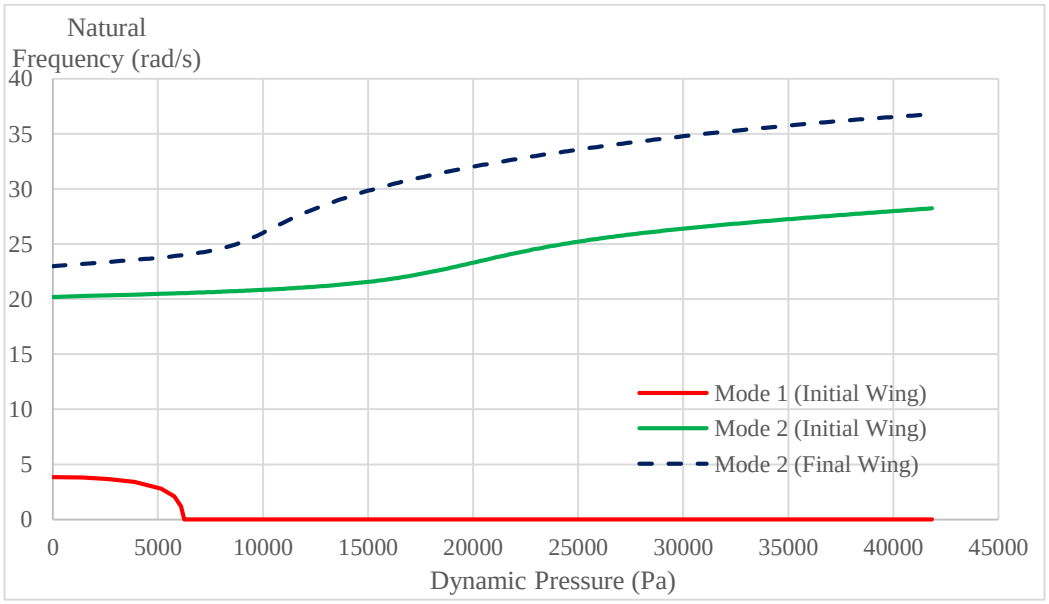

Figure 7.6: Natural frequency for critical flutter modes (initial and final wings: aspect ratio = 18).

For the wing with an aspect ratio of 20, there is a 50.4% mass reduction between the initial and final solutions. Similar to the results for wing with an aspect ratio of 18, the compliance constraint also manages to converge at 6.00×10^5Pa, which is the target value. There is an increase of 36.6% for the flutter dynamic pressure between the initial and final solutions. Figure 7.7 shows the convergence histories for the wing mass, compliance constraint and continuous flutter constraint. Between the 33rd and 34th iterations, there is a large increase in the continuous flutter constraint value. The value at the 33rd iteration is -0.00157 whereas at the 34th iteration, it is computed to be -0.25. The reason is that at 34th iteration, the flutter analysis is unable to find any critical flutter points for that particular topology. The same flutter sensitivities from 33rd iteration are used to proceed with the optimisation, and critical flutter is found at the 35th iteration. The optimisation for this aspect ratio converges at the 41st iteration.

It is noticed that the angle of attack has decreased from 0.91 º(initial topology) to 0.35 º(final topology). Figure 7.8(c) illustrates the internal configuration of the final topology. The configuration of the structure suggests material to be added at the wing tip. This results in smaller deflection at the wing tip. The flutter analysis shown in Figure 7.9 represents the critical dynamic pressures for initial and final topologies. Both topologies have the same critical mode (mode 1: first bending mode) as divergence occurs before flutter. The flutter frequency is also found to be 0 rad/s for both topologies (Figure 7.10).

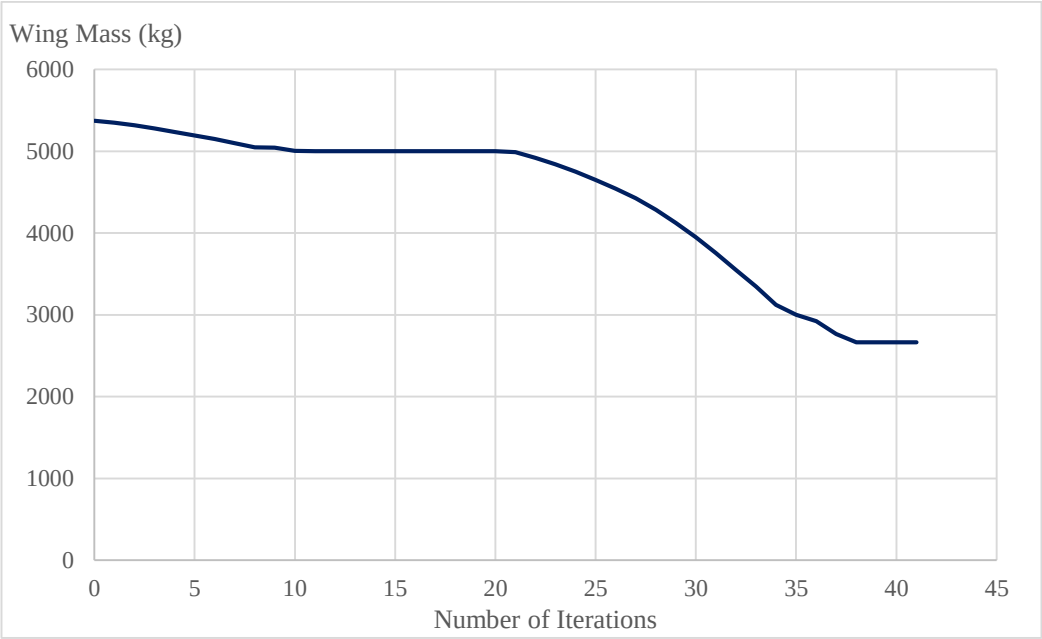

(a)

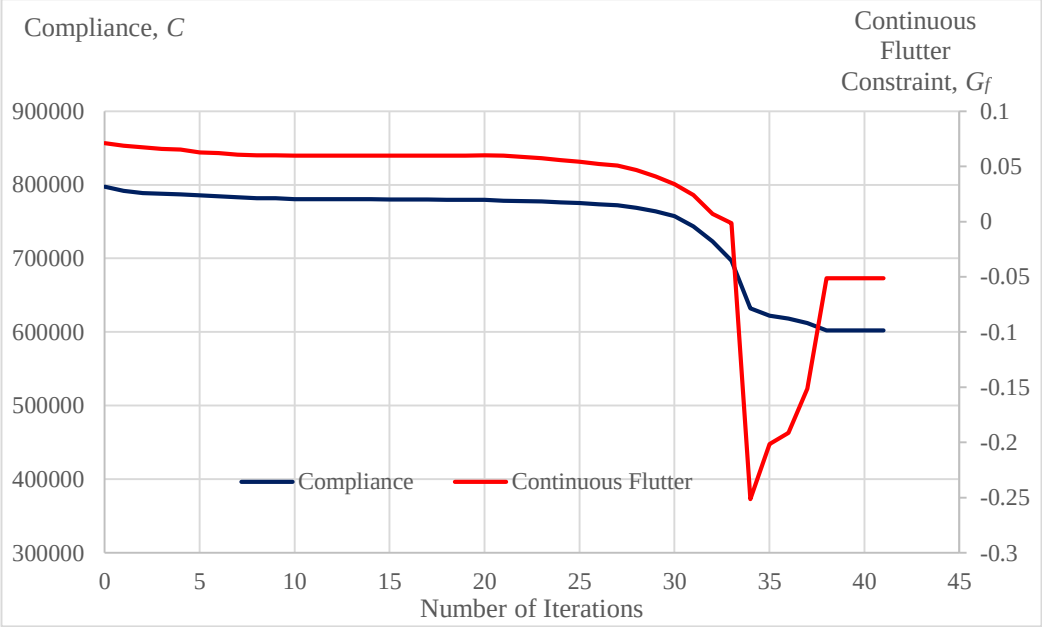

(b)

Figure 7.7: Optimisation convergence history for wing aspect ratio = 20: (a) Objective function – wing mass, (b) Constraint functions – compliance and continuous flutter constraint.

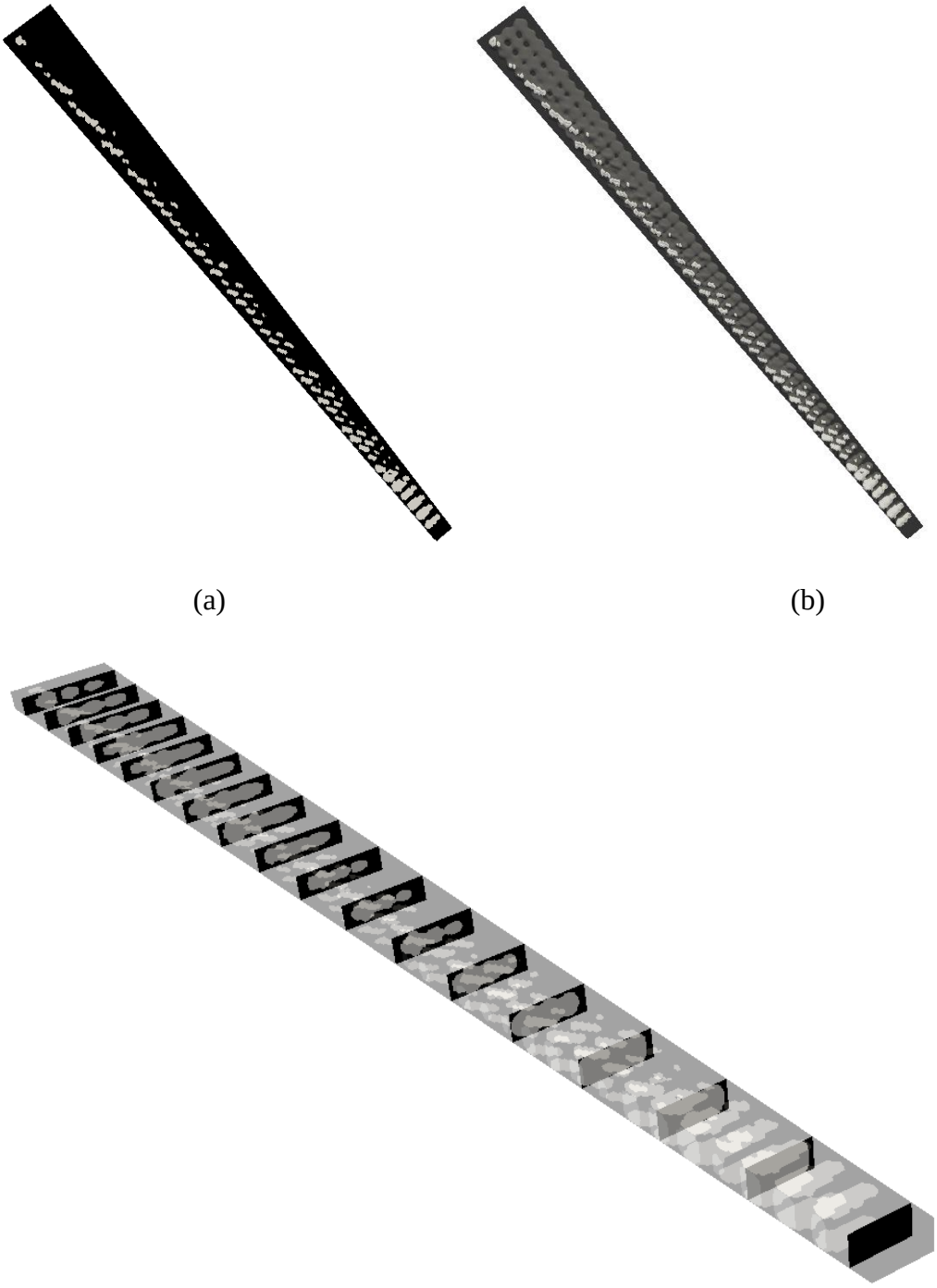

(a) (b)

(c)

Figure 7.8: Final solution for aeroelastic optimisation (AR = 20): (a) top view, (b) 3D contour of the internal structure, (c) sections through the contour (do not represent ribs)

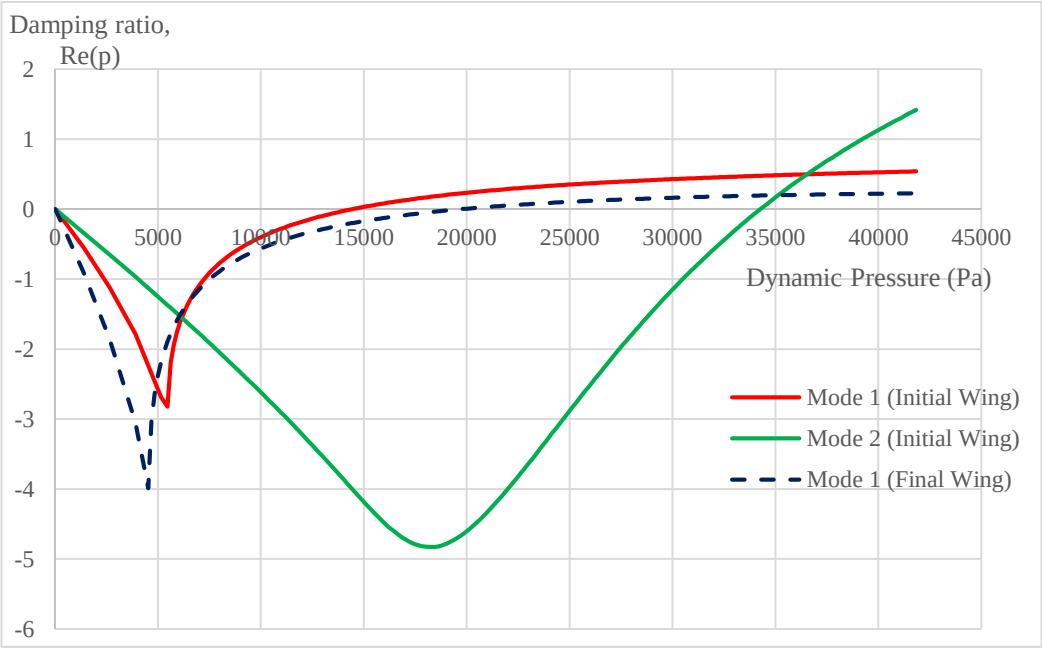

Figure 7.9: Damping ratio curve for critical flutter modes (initial and final wings: aspect ratio = 20).

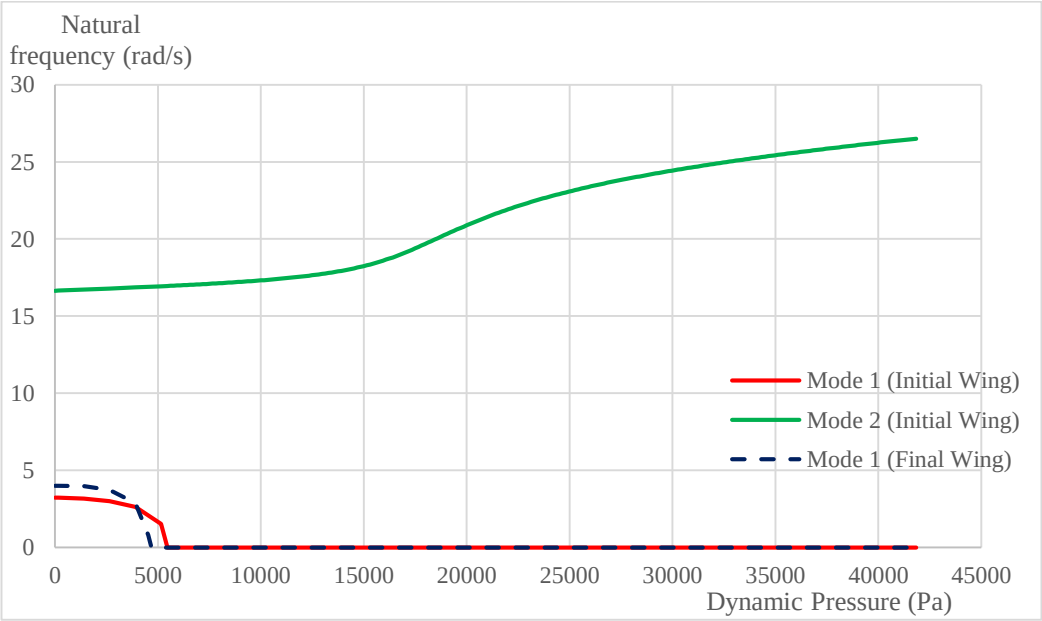

Figure 7.10: Natural frequency for critical flutter modes (initial and final wings: aspect ratio = 20).

For the wing with an aspect ratio of 24, there is a 60.7% mass reduction between the initial and final solutions. The mass reduction in this wing aspect ratio is the largest compared to the previous two wing aspect ratios. The compliance constraint is active and there is a large increase of 91.4% for the flutter dynamic pressure between the initial and final solutions. Figure 7.11 shows the convergence histories for the wing mass, compliance constraint and continuous flutter constraint. The convergence for this wing (312 iterations) is considerably slower than the previous wing aspect ratios due to the mode switching between mode 1 and mode 2. The damping curve in Figure 7.13 shows that mode 1 is a hump mode for the final topology, and the critical mode is a flutter mode at mode 2.

Similar to the wing with an aspect ratio of 20, the angle of attack has decreased from 0.76 º(initial topology) to 0.52 º(final topology). The internal configuration in Figure 7.12(c) suggests some materials should be added near the wing tip to relieve the tip loading. It can be observed that the thicknesses varied along the wing span. The final topology has thicker skin in every few other sections. Along the mid span, more material is found to be on the leading edge than the trailing edge. The flutter frequencies of the final topology for both mode 1 and mode 2 are higher than the initial topology.

The results from all three different aspect ratio wings show that even though the initial topology starts with infeasible solution, the SLP level set topology optimisation is able to find the feasible direction and converge with feasible solutions.

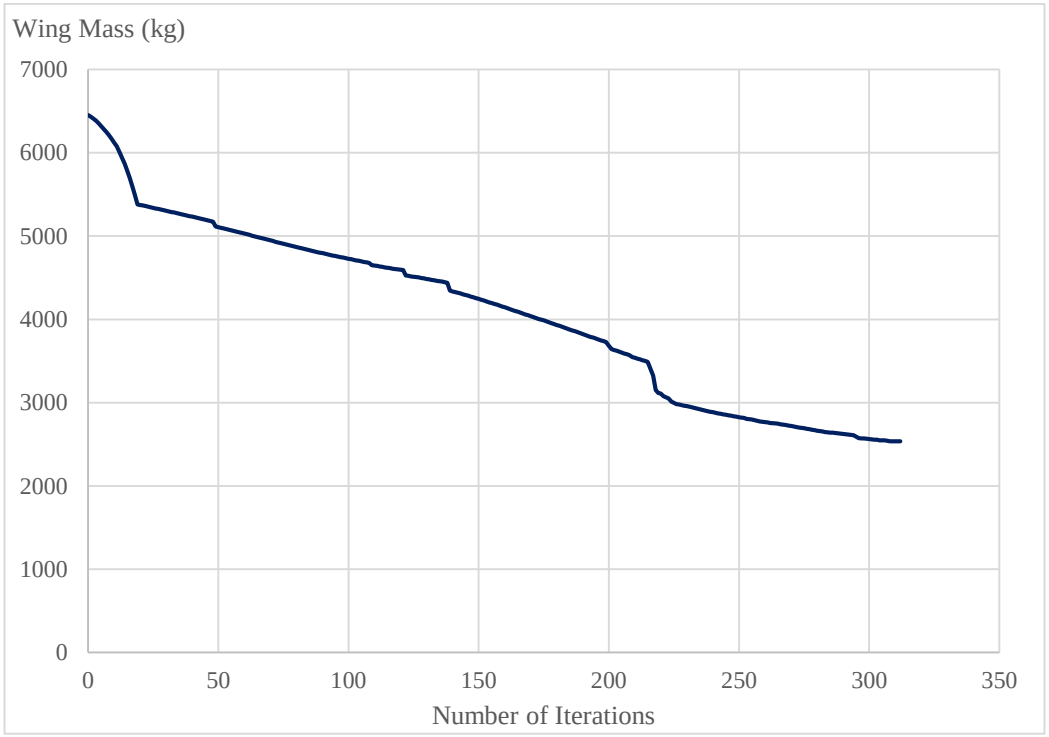

(a)

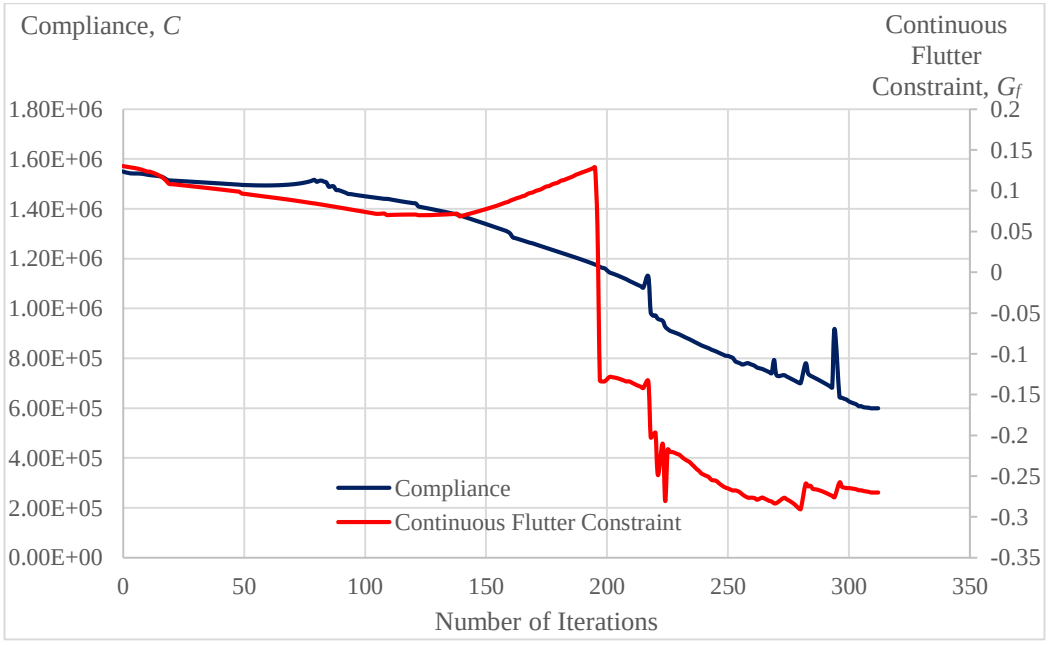

(b)

Figure 7.11: Optimisation convergence history for wing aspect ratio = 24: (a) Objective function – wing mass, (b) Constraint functions – compliance and continuous flutter constraint.

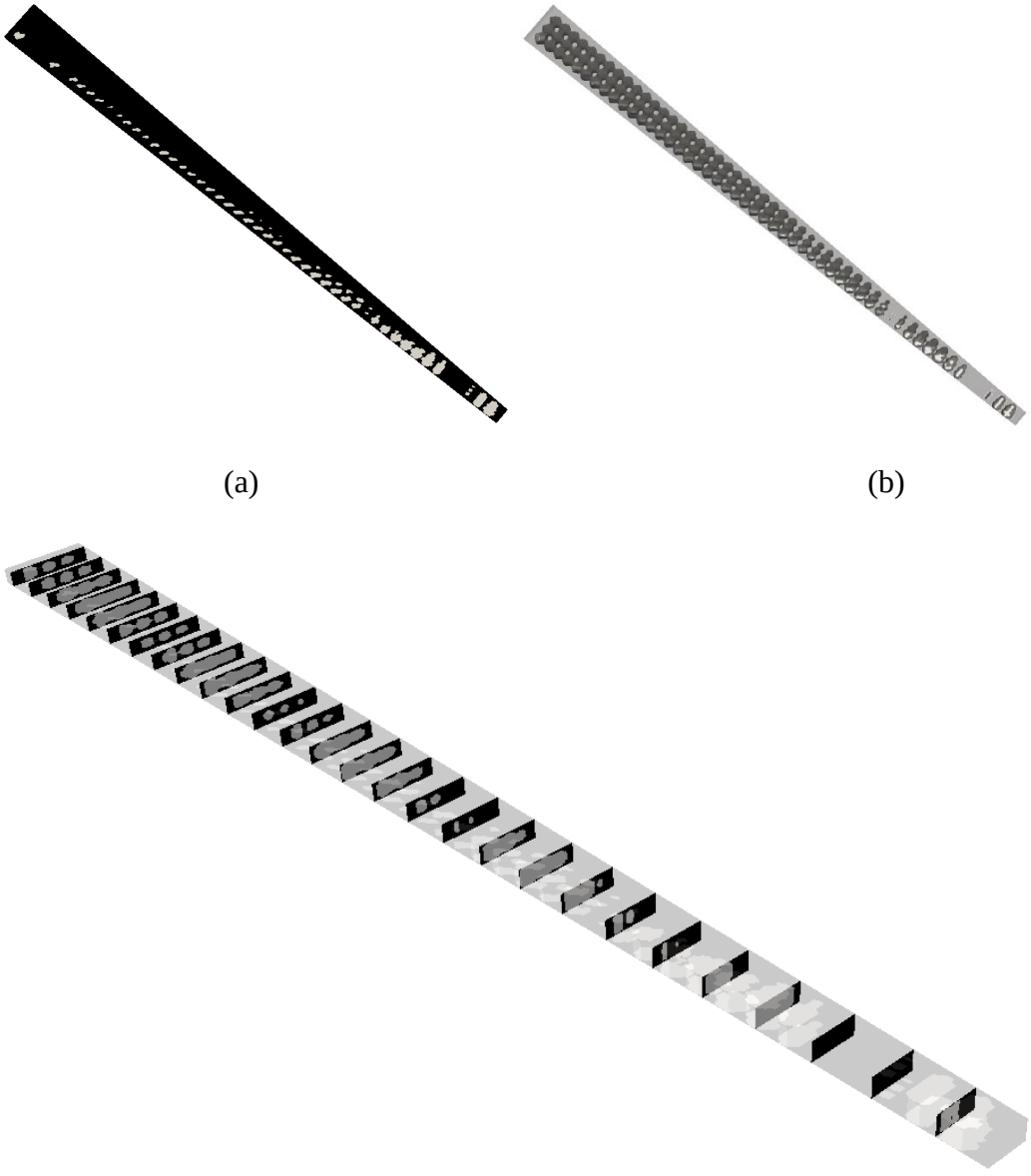

(a) (b)

(c)

Figure 7.12: Final solution for aeroelastic optimisation (AR = 24): (a) top view, (b) 3D contour of the internal structure, (c) sections through the contour (do not represent ribs)

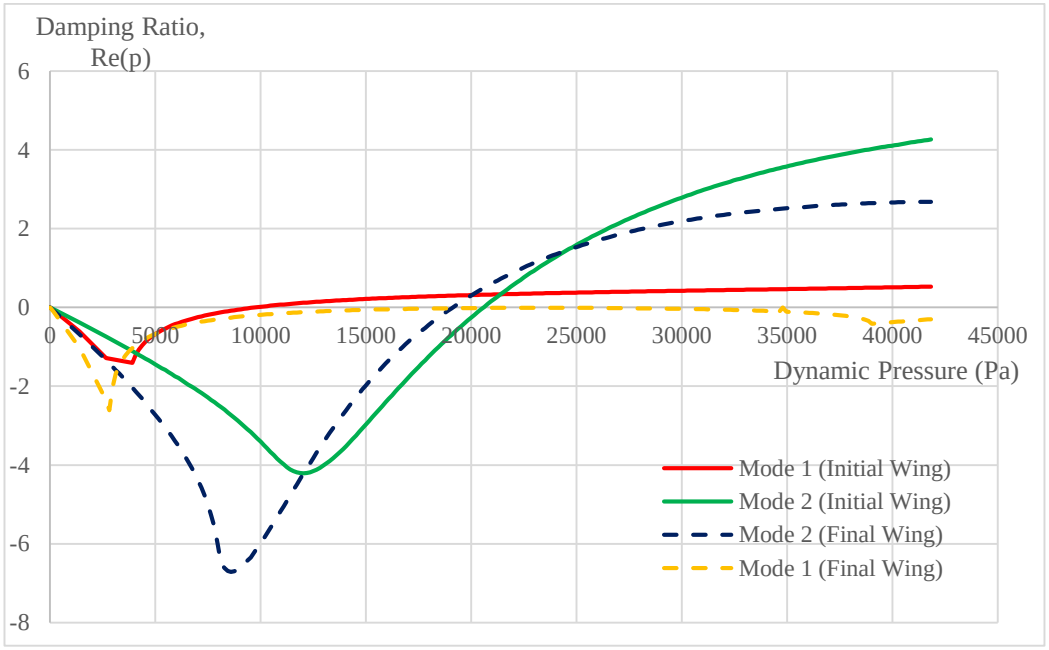

Figure 7.13: Damping ratio curve for critical flutter modes (initial and final wings: aspect ratio = 24).

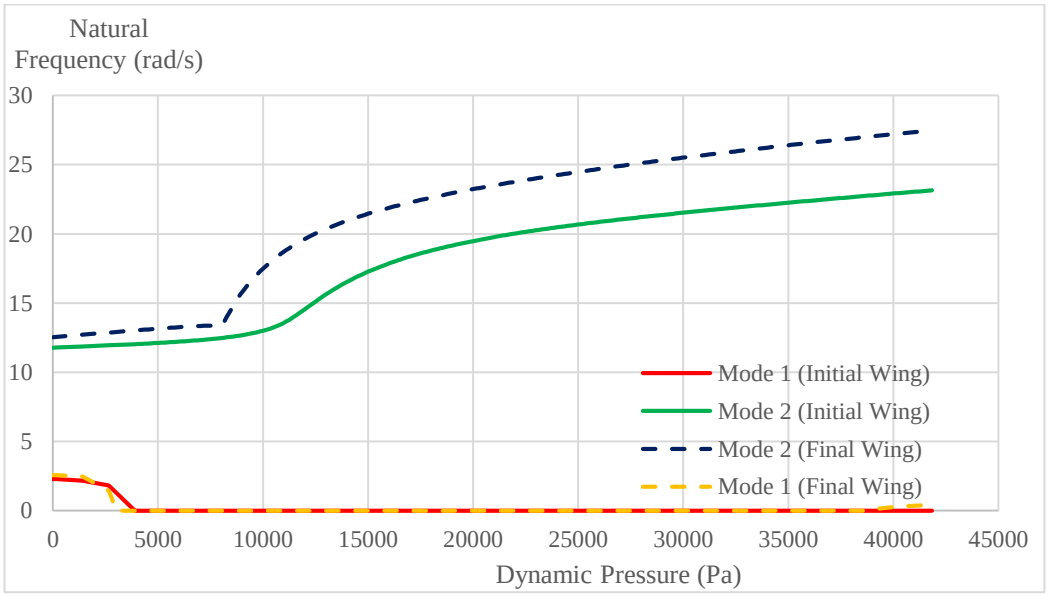

Figure 7.14: Natural frequency for critical flutter modes (initial and final wings: aspect ratio = 24).

7.4 Conclusions

A SLP level set topology optimisation is extended to handle multiple constraints optimisation problem. The derivatives of the objective function and constraint functions are first calculated at the nodal points and then interpolated to the boundary nodes using the least squares method. The velocity function is smoothed using the velocity weight technique. The SLP method is then used to optimise the velocity weights during the sub-optimisation problem.

Three different aspect ratio wings (AR = 18, 20, 24) are selected for the research studies. The aeroelastic optimisation involves minimising the wing mass, whilst satisfying the compliance and continuous flutter constraints. The target compliance value is obtained by minimising a wing with an aspect ratio of 18, subject to a 50% wing mass ratio. The continuous flutter constraint function is an inequality constraint, such that the function has to be less than zero. All three wings start with an infeasible solution, as the critical dynamic pressure (divergence) is less than the prescribed flutter constraint. However, these three wings have reached a feasible solution, where the compliance constraint is active.

The optimisation results also further prove that the effective modal mass method successfully eliminate the local modes, because the problem converges very smoothly. Even though it takes longer for wing with an aspect ratio of 24 to converge, it is caused by the natural mode switching. The continuous flutter constraint is able to suppress the hump mode, and eventually find the critical flutter mode.

Chapter 8

Conclusions and Future Remarks

This final chapter of the thesis collects the achievements and conclusions from the previous chapters and considers what the next stage of research would be for each area. The review of the literature showed that there are many varieties of methods to optimise the aircraft wing box. Aeroelastic topology optimisation has been widely used to design the internal configuration of aircraft wing box as it allows greatest freedom to find the best possible designs. The level set topology optimisation method has been used to solve a range of aeroelastic problems and objective functions because the method produces solutions with clear boundaries. However, the aeroelastic optimisation research in high aspect ratio wings are very rare in the literature. The motivation for this thesis was to find the best design for the internal configuration of aircraft high aspect ratio wings using the level set topology optimisation method.

In the aeroelastic optimisation study, three core discipline were considered: aerodynamics, structures and aeroelasticity such as divergence and flutter, leading

to the development of a framework for aeroelastic analysis. Aerodynamic and structural models were developed to perform loads and displacements calculations. It is important to couple the aerodynamic and structural meshes, known aero-structural interaction. A 3D finite element wing box model was developed to couple with an aerodynamic doublet lattice model. A more accurate aerodynamic analysis can be included in the future work. A finite plate spline method was used to accurately transfer the loads and displacement data. For the dynamic part, a free vibration analysis was conducted to capture the natural frequencies and mode shapes for the interested modes. A *p-k* method was implemented to calculate the divergence or flutter dynamic pressure.

First order derivatives of the objective function and constraints are required for the level set optimisation. The first order derivatives of the wing mass, compliance and flutter dynamic pressure were derived. Sensitivity analysis in a discrete form was first derived with respect to any structural design variables. Sensitivity analysis in a continuous form was later developed with respect to the level set boundary domain, which is applicable for the level set optimisation method. It is expected that the structural boundaries were moved during the optimisation and this results in the finite elements being cut. A least squares interpolation technique was used to calculate the boundary sensitivities.

Mode switching was a well-known problem in aeroelastic optimisation as it could cause discontinuity during the optimisation process. Existing mode tracking such as the modal assurance criterion method and eigenvector orthogonality correlation method were discussed. These methods could experience a failure to track modes. An improved eigenvector orthogonality correlation method was introduced in this work by employing the Hungarian algorithm to track the modes during divergence or flutter analysis. The level set optimisation method was used to maximise the flutter dynamic pressure of a high aspect ratio wing whilst satisfying the mass constraint. Mode switching was found during the optimisation but the improved eigenvector correlation method was able to track the modes successfully and prevented any discontinuity in the optimisation. A range of

various mass constraints were imposed to run the optimisation. The optimal structural topologies were discussed and the mass distribution of the wing played an important role in flutter maximisation studies. Further studies were needed to test the improved eigenvector correlation method with different wing aspect ratios.

A local modes phenomenon was also an existing issue in the aeroelastic topology optimisation. To demonstrate the local mode problems, wing mass minimisation subject to a continuous flutter constraint was formulated for a high aspect ratio wing. The problem was optimised using the Sequential Linear Programming (SLP) level set based method. Local modes were identified when the natural frequency method was adopted where the mode shapes were updated in every iteration. An assumed mode method was implemented by retaining the same mode shapes of the initial wing topology throughout the optimisation. This method produced a much smoother convergence. However, when the final solution was verified against the natural frequency method, a big difference in the critical dynamic pressure was found. Effective modal mass method was then developed and implemented to calculate the ratio of effective modal mass for shell and solid elements of the structural wing. The results showed the effective modal mass method produced smooth convergence, as well as predicted the accurate critical flutter dynamic pressures.

An optimisation problem with the objective function being wing mass subject to compliance and flutter constraints are implemented. The SLP level set method was extended to handle multiple constraints. An adjoint method for coupled sensitivity analysis of aero-structural interaction was presented. Three different wing aspect ratios were chosen in this optimisation studies. The dynamic characteristics, such as natural frequencies and damping were discussed in detail. Future development includes applying a hole insertion method into the 3D level set topology optimisation, so that the final solution would not depend on the initial solution. In addition, robust topology optimisation could be introduced to solve the optimisation problem with various loading conditions and flight conditions.

References

Appa, K. (1989) Finite-surface spline. *Journal of Aircraft*. 26(5). 495-496.

Albano, E. and Rodden, W. P. (1969) A doublet-lattice method for calculating lift distributions on oscillating surfaces in subsonic flows. *AIAA Journal*. 7(2). 279-285.

Allaire, G., Jouve, F., and Toader, A. (2004) Structural optimization using sensitivity analysis and a level-set method. *Journal of Computational Physics*. 194(1), 363–393.

Allemang, R. J., and Brown, D.L. (1982) A correlation coefficient for modal vector analysis. *In Proceeding of International Modal Analysis Conference*. 110-116.

Arizono, H., and Isogai, K. (2005) Application of genetic algorithm for aeroelastic tailoring of a cranked-arrow wing. *Journal of Aircraft*. 42(2). 493-499.

Balabanov, V. O., and Haftka, R. T. (1996) Topology optimization of transport wing internal structure. *Journal of Aircraft*. 33(1). 232-233.

Barboni, R., Mannini, A., and Gaudenzi, P. (1999) On the use of the P-TFE method for panel flutter optimization. *Computers and Structures*. 70(1). 109–117.

Bendsøe, M. P., and Sigmund, O. (2004) *Topology optimization: Theory, Methods and Applications*. Germany: Springer-Verlag.

Bendsøe, M., and Sigmund, O. (1999) Material interpolation schemes in topology optimization. *Archive of Applied Mechanics*. 69. 635–654

Brampton, C. J., Kim, H. A., Cunningham, J. L. (2012) Level set topology optimisation of aircraft wing considering aerostructural interaction. *In Proceedings of the 14th AIAA/ISSMO Multidisciplinary Analysis and Optimization*, Indianapolis, United States.

Brown, S. A. (1997) Displacement extrapolations for CFD+CSM aeroelastic analysis. *In Proceedings of the 38th Structures, Structural Dynamics, and Materials Conference, Structures, Structural Dynamics, and Materials and Co-located Conferences*. AIAA Paper 97-1090.

Bruggi, M., and Duysinx, P. (2012) Topology optimization for minimum weight with compliance and stress constraints. *Structural Multidisciplinary Optimization*. 46. 269-284.

Butler, R., and Banerjee, J. (1996) Optimum design of bending-torsion coupled beams with frequency or aeroelastic constraints. *Computers and Structures*. 60(5). 715–724.

Chedrik, V. V., Ishmuratov, F. Z., Kuzmina, S. I., and Zichenkov, M. C. (2010) Strength/aeroelasticity research at multidisciplinary structural design of high aspect ratio wing. *In Proceedings of the 27th Congress of International Council of the Aeronautical Sciences*, Nice, France. 19-24 September.

Clough, R. W., and Penzien, J. (1975) *Dynamics of structures*, McGraw Hill, Inc.

Desforges, M. J., Cooper, J. E., and Wright, J. R. (1996). Mode tracking during flutter testing using the modal assurance criterion. *In the Proceedings of the*

Institution of Mechanical Engineers, Part G (Journal of Aerospace Engineering). 210 (G1). 27-37.

Du, J. B., and Olhoff, N. (2007). Topological design of freely vibrating continuum structures for maximum values of simple and multiple eigenfrequencies and frequency gaps. *Structural and Multidisciplinary Optimization*, 34(2). 91-110.

Duan, K., Seow, Y. E. V., Kim, H. A., and Padget, J. (2012) A resource-oriented architecture for MDO frameworks. *In Proceedings of the 53th AIAA/ASCE/AHS/ASC Structures, Structural Dynamics, and Materials Conference*. Honolulu, Hawaii, United States. 23-26 April.

Dunning, P. D. (2011) *Introducing loading uncertainty in level set-based structural topology optimisation*. Ph.D. thesis submitted to the University of Bath.

Dunning, P. D., Brampton, C. J., and Kim, H. A. (2013) Multidisciplinary level set topology optimization of the internal structure of an aircraft wing. *In Proceedings of the 10th World Congress on Structural and Multidisciplinary Optimization*. Orlando, Florida, United States. 19-24 May.

Dunning, P. D. and Kim, H. A. (2013). A new hole insertion method for level set based structural topology optimization. *International Journal for Numerical Methods in Engineering*. 93 (1). 118-134.

Dunning, P. D., and Kim, H. A. (2015) Introducing the sequential linear programming level-set method for topology optimization. *Structural and Multidisciplinary Optimization*. 51 (3). 631-643.

Dunning, P. D., Kim, H. A., and Mullineux, G. (2011). Investigation and improvement of sensitivity computation using the area-fraction weighted fixed grid FEM and structural optimization. Finite Element Analysis and Desgin. 47(8). 933-941

Dunning, P. D., Stanford, B. K., and Kim, H. A. (2014) Aerostructural level set topology optimization for a common research model wing. *In Proceedings of*

the 10th AIAA Multidisciplinary Design Optimization Specialist Conference, Maryland, United States. 13-17 January.

Dunning, P. D., Stanford, B. K., and Kim, H. A. (2015) Level-set topology optimization with aeroelastic constraints. *In Proceedings of the 56th AIAA/ASCE/AHS/ASC Structures, Structural Dynamics, and Materials Conference*. Kissimmee, United States. 5-9 January.

Eldred, M. S., Venkayya, V. B., and Anderson, W. J. (1995) New mode tracking methods in aeroelastic analysis. *AIAA Journal*. 33(7). 1292-1299.

Eschenauer, H. A., and Olhoff, N. (2001) Topology optimization of continuum structures: A Review. *Applied Mechanics Reviews*. 54(4). 331-390.

Eves, J., Toropov, V. V., Thompson, H. M., Gaskell, P. H., Doherty, J. J., and Harris, J. C. (2009) Topology optimization of aircraft with non-conventional configurations. *In Proceedings of the 8th World Congress on Structural and Multidisciplinary Optimization*. Lisbon, Portugal.

Ewins D. J. *Modal testing: theory and practice*. Bruèel & Kjñr, 1986.

Gasbarri. P., Chiwiacowsky L. D., Velho H.F.C. (2009) A hybrid multilevel approach for aeroelastic optimization of composite wing-box. *Structural Multidiscplinary Optimization*. 39. 607-624

Gomes, A. A., and Suleman, A. (2008) Topology optimization of a reinforced wing box for enhanced roll maneuvers. *AIAA Journal*. 46(3). 548-556.

Haftka, R. T. (1975) Parametric constraints with application to optimization for flutter using a continuous flutter constraint. *AIAA Journal*. 13(4). 471-475.

Harder, R. L., and Desmarais, R. N. (1972) Interpolation using surface splines. *Journal of Aircraft*. 9(2). 189-191.

Haviland, J. K., and Yoo, Y. S. (1973) Downwash-velocity potential method for oscillating surfaces. *AIAA Journal*. 11 (5). 607-612.

Hollowell, S. J., and Dugundji, J. (1984) Aeroelastic flutter and divergence of stiffness coupled, graphite/epoxy cantilevered plates. *Journal of Aircraft*. 21(1). 69-76.

Howcroft, C., Calderon, D., Lambert, L., Castellani, M., Cooper, J. E., Lowenberg, M. H., and Neild, S. (2016) Aeroelastic modelling of highly flexible wings. *In Proceedings of the 15th Dynamics Specialists Conference, AIAA SciTech*.

James, K. A., and Martins, J. R. R. A. (2012) An isoparametric approach to level set topology optimization using a body-fitted finite element mesh. *Computers and Structures*. 90-91. 97-106.

James, K. A., Kennedy, G. J., and Martins, J. R. R. A. (2014) Concurrent aerostructural topology optimization of a wing box. *Computers and Structures*. 134(1). 1-17.

Jutte, C.V., Stanford, B. K., Wieseman, C. D., and Moore, J. B. (2014) Aeroelastic tailoring of the NASA common research model via novel material and structural configurations. *In Proceedings of the SciTech Conference*, National Harbour, MD.

Kalman, T. P., Giesing, J. P. and Rodden, W. P. (1970) Application of the doublet-lattice method to nonplanar configurations in subsonic flows. *Journal of Aircraft*. 8(6). 406-413.

Kennedy, G., Kenway, G., and Martins, J. R. R. A. (2014) Towards gradient-based design optimization of flexible transport aircraft with flutter constraints. *In Proceedings of 15th AIAA/ISSMO Multidisciplinary Analysis and Optimization Conference*, AIAA Aviation.

Kim, M. J. (2013) *Introduction to finite element methods with programing and Ansys*. Lulu.com. ISBN: 978130077151.

Kim, T. S., and Kim, Y. Y. (2000) Mac-based mode-tracking in structural topology optimization. *Computers and Structures*. 74. 375-383.

Kobayashi, M. H., Pedro, H. T. C., Kolonay, R. M., and Reich, G. W. (2010) On a cellular division model for multi-disciplinary optimization. *In Proceedings of the 51st AIAA/ASME/ASCE/AHS/ASC Structures, Structural Dynamics, and Materials Conference*, Orlando, Florida. 12-15 April.

Krog, L., Tucker, A., Kemp, M., and Boyd, R. (2004) Topology optimization of aircraft wing box ribs. *In Proceedings of the AIAA Multidisciplonary Analysis and* Optimization Conference, Albany NY, August 30 – September 1.

Kuhn, H. W. (2009) *50 years of integer programming 1958-2008. Chapter 2: The Hungarian method for the assignment problem*. Germany: Springer-Verlag

Langthjem, M., and Sugiyama, Y. (1999) Optimum shape design against flutter of a cantilevered column with an end-mass of finite size subjected to a non-conservative load. *Journal of Sound and Vibration*. 226(1). 1-23.

Li, J., Chen, S., and Huang, H. (2015) Topology optimization of continuum structure with dynamic constraints using mode identification. *Journal of Mechanical Science and Technology*. 29(4). 1407-1412.

Luo, J., Luo, Z., Chen, L., Tong, L., and Wang, M. Y. (2008) A semi-implicit level set method for structural shape and topology optimization. *Journal of Computational Physics*. 227 (11). 5561–5581

Maute, K., and Allen, M. (2004) Conceptual design of aeroelastic structures by topology optimization. *Structural and Multidisciplinary Optimization*. 27(1). 27-42.

Mei, Y., and Wang, X. (2004) A level set method for structural topology optimization and its applications. *Advanced Engineering Software*. 35(7). 415–441

Neves, M. M., Rodrigues, H., and Guedes, J. M. (1995) Generalized topology design of structures with a buckling load criterion. *Structural and Multidisciplinary Optimization*. 10. 71-78.

Odaka, Y., and Furuya, H. (2005) Robust structural optimization of plate wing corresponding to bifurcation in higher mode flutter. *Structural and Multidisciplinary Optimization*. 30(6). 437–446.

Osher, S., and Santosa, F. (2001) Level set methods for optimization problems involving geometry and constraints: I. Frequencies of a two-density inhomogeneous drum. *Journal of Computational Physics*. 171(1). 272–288

Pastilha, P. (2007) Structural optimization for flutter instability problems. *M.S. Thesis*, Technical University of Lisbon, Mechanical Engineering Department, Lisbon.

Pedersen, N. L. (2000) Maximization of eigenvalues using topology optimization. *Structural and Multidisciplinary Optimization*. 20(1). 2-11.

Pidaparti, R. M. V. (1992) Structural and aerodynamic data transformation using inverse isoparametric mapping. *Journal of Aircraft*. 29(3). 507-509.

Rendall, T. C. S., and Allen, C. B. (2007) Unified fluid-structure interpolation and mesh motion using radial basis functions. *International Journal for Numerical Methods in Engineering*. 74(10). 1519-1559.

Rodden, W. P., Giesing, J. P. and Kalman, T. P. (1972) Refinement of the nonplanar aspects of the subsonic doublet-lattice lifting surface method. *Journal of Aircraft*. 9(1). 69-73.

Rodden, W. P., and Johnson, E. H. (1994). MSC. NASTRAN aeroelastic analysis user's guide, version 68. *Machneal-Schwendler Corp.*, Los Angeles.

Roughen, K. M., Baker, M. L. and Fogarty, T. (2001) Computational fluid dynamics and doublet-lattice calculation of unsteady control surface aerodynamics. *Journal of Guidance, Control, and Dynamics*. 24(1). 160-166.

Rule, J. A., Richard, R. E. and Clark, R. L. (2001) Design of an aeroelastic delta wing model for active flutter control. *Journal of Guidance, Control, and Dynamics*. 24(5). 918-924.

Schmitt, A. F. (1956) A least squares matrix interpolation of flexibility influence coefficients. *Journal of the Aeronautical Sciences*. Vol. 23. pp. 980.

Seyranian, A. (1982) Sensitivity analysis and optimization of aeroelastic stability. *International Journal of Solids and Structures*, 18(9). 791–807.

Sethian, J. A. (1999). *Level set methods and fast marching methods 2nd edition*, New York: Cambridge University Press.

Shirk, M. H., Hertz, T. J., and Weisshaar, T. A. (1986). Aeroelastic tailoring – theory, practice, and promise. *Journal of Aircraft.* 23(1). 6-18.

Stanford, B. K., and Beran, P. (2011) Optimal structural topology of a platelike wing for subsonic aeroelastic stability. *Journal of Aircraft*. 48(4). 1193-1203.

Stanford, B. K., Beran, P., and Bhatia, M. (2014) Aeroelastic topology optimisation of blade-stiffened panels. *Journal of Aircraft*. 51(3). 938-944.

Stanford, B. K., and Dunning, P. D. (2014) Optimal topology of aircraft rib and spar structures under aeroelastic loads. *Journal of Aircraft*. 52(4). 1-14.

Stodieck, O., Cooper, J. E., Weaver, P., and Kealy, P. (2013) Improved aeroelastic tailoring using tow-steered composites. *Composite Structures*. (106). 703-715.

Stodieck, O., Cooper, J. E., Weaver, P., and Kealy, P. (2015) Optimization of tow-steered composite wing laminates for aeroelastic tailoring. *AIAA Journal*. 53(8). 2203-2215.

Stolpe, M., and Svanberg, K. (2001). An alternative interpolation scheme for minimum compliance topology optimization. *Structural and Multidisciplinary Optimization*. 22(2). 116-124.

Stroud, W., Krishnamurthy, T., Mason, B., Smith, S., Naser, A. (2002) Probabilistic design of a plate-like wing to meet flutter and strength requirements. *In Proceedings of the AIAA Structures, Structural Dynamics, and Materials Conference*, Denver, CO. AIAA Paper 2002-1464.

Tang, P.S. and Chang, K.H. (2001). Integration of topology and shape optimization for design of structural components. *Structural and Multidisciplinary Optimization*, 22(1). 65-82.

Tcherniak, D. (2002). Topology optimization of resonating structures using SIMP method. *International Journal for Numerical Methods in Engineering*, 54(11). 1605-1622.

Ting, T., Chen, T. L. C., and Twomey, W. J. (1994). Automated mode tracking strategy. *AIAA Journal*. 33(1). 183-185.

Tsai, T. D., and Cheng, C. C. (2013) Structural design for desired eigenfrequencies and mode shapes using topology optimization. *Structural and Multidisciplinary Optimization.* 47(5). 673-686.

van Dijk, N. P., Maute, K., Langelaar, M., and van Keulen, F. (2013) Level-set methods for structural topology optimization: a review. *Structural and Multidisciplinary Optimization*. 48(3). 437-472

van Zyl, L. H. (2001) Aeroelastic divergence and aerodynamic lag roots. *Journal of Aircraft*. 38 (3). 586-588.

van Zyl, L. H. (1993) Use of eigenvectors in the solution of the flutter equation. *Journal of Aircraft*. 30 (4). 553-554.

Wang, M. Y., and Wang, X. (2004) "Color" level sets: a multi-phase method for structural topology optimization with multiple materials. *Computational Methods Applied Mechanical Engineering*. 193(6–8). 469–496

Wang, M. Y., Wang, X., and Guo, D. (2003) A level set method for structural topology optimization. *Computer Methods in Applied Mechanics and Engineering*. 192(1-2). 227–246.

Weisshaar, T. A. (1987) Aeroelastic tailoring – creative use of unusual materials. In. *Proc. 28th ASME, ASCE, and AHS, Structures, Structural Dynamics and Materials Conference*, Monterey, CA. AIAA Paper 87-0976-CR. Apr. 6-8,

Weisshaar, T. A., and Ryan, R. J. (1986) Control of aeroelastic instabilities through stiffness cross-coupling. *Journal of Aircraft*. 23(2). 148-155.

Wright, J. R., and Cooper, J. E. (2007). *Introduction to Aircraft Aeroelasticity and Loads*. John Wiley & Sons Ltd, West Sussex, England.

Yuan, J. (2004). *Design and analysis of satellite structures*. (Chinese edition).

Zhu, S., Wu, Q., and Liu, C. (2010) Variational piecewise constant level set methods for shape optimization of a two-density drum. *Journal of Computational Physics*. 229 (13). 5062–5089.